UNIMORE
UNIVERSITÀ DEGLI STUDI DI
MODENA E REGGIO EMILIA

UNIVERSITÀ DEGLI STUDI
DI MODENA E REGGIO EMILIA

Dottorato di ricerca in Ingegneria industriale e del territorio

Ciclo XXXVIII

From 1D to 3D Numerical Modeling of Lithium-Ion Battery

Candidato: Elif Kaya

Relatore (Tutor): Prof. Alessandro d'Adamo

Eventuale Correlatore (Co-Tutor): Dr. Fabio Berni

Coordinatore del Corso di Dottorato: Prof. Alberto Muscio

To my dear parents, Emel and Kemal Görken...

I would like to express my deepest gratitude to my supervisor, **Prof. Alessandro d'Adamo**, who is one of the most professional and understanding individuals I have ever met. I am grateful to him for always instilling hope in me and reminding me of my true potential. His mentorship and academic approach will serve as a guiding example that I will strive to emulate throughout my entire academic career.

I am also deeply indebted to **Prof. Alberto Muscio**. His endless support, sincerity, and encouragement during my PhD application process were instrumental in starting this journey, and I am grateful for his belief in me.

I gratefully acknowledge the financial support provided by the **Republic of Türkiye Ministry of National Education** and the **YLSY scholarship program**, which made my doctoral studies possible.

A very special thanks goes to my dear aunt, **Ayla Üsküplü**. From buying me my very first reading book in my childhood to offering unhesitating support with her endless trust during my PhD, she has always been a pillar of strength for me.

To my beloved husband and dear life partner, **Ahmet Fatih Kaya**; thank you for walking this path with me and for the life we have been building together for years to make our dreams come true.

Finally, I would like to thank my entire **family**, whose love and support I have always felt by my side.

INDEX

From 1D to 3D Numerical Modeling of Lithium-Ion Battery

Abstract (English)

Advancements in powertrain technology and the expanding electrification of vehicles have made batteries one of the primary solutions to the rising need for energy storage. With the growing demand for electric batteries, the Battery Thermal Management System (BTMS), which plays a crucial role in ensuring their safety, performance, and lifespan, has gained increasing importance. In this thesis, in the first stage, C-rates of 0.1C, 0.5C, 1C, 2C, and 3C, which are applicable to automotive applications, were analyzed using a 1D Isothermal Lithium-ion Battery model developed with the Battery Design Module of COMSOL Multiphysics software. Following this study, the same model was examined under various electrolyte and electrode materials.

In the next stage, the effects of different cooling fluids and flow rates were investigated on the Thermal Modeling of a Cylindrical Lithium-ion Battery in a 3D model. These included conventional coolants (air and water) as well as nanofluid coolants using water, ethylene glycol (EG), and ethylene glycol water (EGW) as base fluids, and separately Al_2O_3 and CuO nanoparticles at different volume fractions (2%, 3%, and 5%). Furthermore, the Taguchi L9 orthogonal array methodology, combined with S/N ratio analysis and analysis of variance (ANOVA), was applied to minimize the maximum temperature (T_{max}) by optimizing control factors such as base fluid, nanoparticle fraction, battery spacing, and inlet temperature (T_{inlet}).

The initial results showed that under higher C-rate operating conditions, variations occurred in the voltage ranges of the electrolyte and electrode, in the salt concentration profiles within the electrolyte, and in the lithium concentrations of the surface and center electrode particles. Regarding the effects of electrolyte and electrode materials, batteries with polymer electrolytes exhibited a slightly higher average salt concentration compared to liquid electrolytes. The battery with a lithium iron phosphate (LFP) positive electrode experienced the largest change in lithium concentration at the surface and center, whereas the $LiNiO_2$ cathode showed the smallest variation.

When examining the cooling strategies, the most significant improvement initially occurred when switching from air to water, with nanofluids providing additional gains. Crucially, the optimization study identified the base fluid and T_{inlet} as the most dominant factors affecting performance. The optimized design (A3-B3-C3-D1), utilizing water with a 5% Al_2O_3 volume fraction, achieved a

T_{max} of 33.5°C. This represents a temperature reduction of 29.0°C compared to the experimentally validated air-cooled reference model (62.5°C). Additionally, the optimized design demonstrated superior thermal stability, exhibiting a heating rate reduction of 73% compared to the air-cooled model.

The study started with the 1D model including Lithium-Ion Battery Interface and continued with the 3D thermal model including Heat Transfer Interface. This integrated approach, validated against the literature and confirmed by the Taguchi method's ability to predict superior optimums, provides a robust tool to guide the design and optimization of future BTMS.

Modellazione Numerica da 1D a 3D di Batterie agli Ioni di Litio

Abstract (Italian)

I progressi nella tecnologia dei gruppi propulsori e la crescente elettrificazione dei veicoli hanno reso le batterie una delle soluzioni primarie alla crescente necessità di accumulo di energia. Con la crescente domanda di batterie per veicoli elettrici, il Sistema di Gestione Termica della Batteria (BTMS), che svolge un ruolo cruciale nel garantirne la sicurezza, le prestazioni e la durata, ha acquisito un'importanza sempre maggiore. In questa tesi, in una prima fase, sono stati analizzati i tassi di C (C-rates) di 0.1C, 0.5C, 1C, 2C e 3C, rappresentativi di applicazioni automobilistiche, utilizzando un modello di batteria agli ioni di litio isotermico 1D sviluppato con il modulo di battery design del software COMSOL Multiphysics. Successivamente a questo studio, lo stesso modello è stato valutato utilizzando vari materiali per elettrolita ed elettrodo.

Nella fase successiva, sono stati studiati gli effetti di diversi fluidi refrigeranti e delle loro portate sul Modello Termico di una Batteria Cilindrica agli Ioni di Litio in 3D. Questi includevano refrigeranti convenzionali (aria e acqua) e nanofluidi refrigeranti che utilizzavano acqua, glicole etilenico (EG) e acqua-glicole etilenico (EGW) come fluidi di base, e nanoparticelle di Al_2O_3 e CuO a diverse frazioni volumetriche (2%, 3% e 5%). Inoltre, è stata applicata la metodologia dell'array ortogonale Taguchi L9, combinata con l'analisi del rapporto S/N e l'ANOVA, per minimizzare la temperatura massima (T_{max}) ottimizzando fattori di controllo quali fluido di base, frazione di nanoparticelle, spaziatura della batteria e temperatura di ingresso.

I risultati iniziali hanno mostrato che, in condizioni operative ad alti tassi di C, si verificavano variazioni negli intervalli di tensione e nei profili di concentrazione salina. Riguardo ai materiali, le batterie con elettroliti polimerici hanno mostrato una concentrazione salina media leggermente superiore rispetto a quelle con elettroliti liquidi. La batteria con un elettrodo positivo LFP ha registrato la maggiore variazione di concentrazione di litio superficiale, mentre il catodo $LiNiO_2$ ha mostrato la variazione più piccola.

Esaminando le strategie di raffreddamento, il miglioramento più significativo si verifica passando dall'aria all'acqua, con ulteriori vantaggi offerti dai nanofluidi. Fondamentalmente, lo studio di ottimizzazione ha identificato il fluido di base e la temperatura di ingresso come i fattori più dominanti. Il design ottimizzato (A3-B3-C3-D1), utilizzando acqua con una frazione volumetrica

del 5% di Al_2O_3, ha raggiunto una T_{max} di 33.5°C. Ciò rappresenta una riduzione della temperatura di 29.0°C rispetto al modello di riferimento raffreddato ad aria (62,5°C) convalidato sperimentalmente. Inoltre, il design ottimizzato ha dimostrato una stabilità termica superiore, con una riduzione del tasso di riscaldamento del 73% rispetto al modello ad aria.

Lo studio ha avuto inizio con il modello 1D ed è proseguito con il modello termico 3D. Questo approccio integrato, validato rispetto alla letteratura e confermato dalla capacità del metodo Taguchi di prevedere ottimi superiori, fornisce uno strumento robusto per guidare la progettazione e l'ottimizzazione dei futuri sistemi di gestione termica delle batterie.

1. INTRODUCTION

In recent years, the ubiquity of high-performance rechargeable batteries has solidified the industry's understanding of their functional requirements. However, this intense demand for advanced, lightweight energy storage was not always prevalent. Initially modest, research in this field experienced a significant surge following Sony Corporation's commercialization of the world's first lithium-ion battery (LIB). The introduction of the LIB revolutionized portable electronics, triggering a substantial increase in academic and industrial interest. Furthermore, this momentum has been bolstered by global governmental initiatives aimed at mitigating climate change; these policies have positioned energy storage systems as pivotal components within green energy infrastructures and the expanding electric vehicle (EV) market [1].

The nomenclature 'battery' was first introduced by Benjamin Franklin in 1749 during his experimentation with interconnected Leyden jar capacitors [2]. Franklin adopted this terminology from the military designation for an array of weapons fired simultaneously. By aggregating multiple jars, he demonstrated that the capacity for charge storage could be significantly amplified, thereby yielding greater power output upon discharge. In 1800, Italian physicist Alessandro Volta constructed and characterized the first electrochemical battery, known as the voltaic pile. This apparatus consisted of alternating copper and zinc plates intercalated with brine-saturated paper discs, a configuration capable of sustaining a steady electric current for extended durations. Despite this engineering feat, Volta erroneously attributed the electromotive force to an inexhaustible energy source [3] rather than chemical processes. Consequently, he dismissed electrode corrosion as a trivial side effect, a misconception corrected in 1834 by Michael Faraday, who demonstrated that such chemical degradation is intrinsic to the battery's operation [4]. While primitive batteries possessed significant experimental value [5], their practical utility was severely constrained by voltage fluctuations and an inability to deliver sustained high currents. The landscape changed in 1836 with British chemist John Frederic Daniell's invention of the Daniell cell, recognized as the first viable source of electricity. This device rapidly became the industry standard, achieving widespread adoption as the primary power supply for electrical telegraph networks. Structurally, it featured a copper vessel containing a copper sulfate solution, within which an unglazed earthenware container holding sulfuric acid and a zinc electrode was immersed [6].

An electric battery is defined as a power source comprising one or more electrochemical cells equipped with external connections [7] to power electrical devices. During the discharge process, the terminal with positive polarity functions as the cathode, while the negative terminal acts as the anode [8].

Batteries are generally categorized into two distinct classes: primary and secondary forms.

- Primary batteries are engineered for single-use applications, intended to be discarded upon energy depletion. Due to the irreversible nature of their electrochemical reactions, they cannot be recharged; once the reactants are consumed, current generation ceases and the unit becomes non-functional.
- Secondary batteries are characterized by their rechargeability, as their chemical reactions can be reversed through the application of an external electrical current. This process regenerates the original active materials, allowing the device to undergo multiple charge-discharge cycles.

Apparatuses designed to facilitate the reuse of secondary batteries through the application of an electric current are designated as chargers. Prominent examples of secondary battery chemistries include Nickel-Cadmium (NiCd), Lead-acid, Nickel-Metal Hydride (NiMH), Nickel-Zinc (NiZn), Silver-Zinc (AgZn), and Lithium-ion (Li-ion) configurations [9]. The structural design of rechargeable batteries is typically categorized into three formats: cylindrical, prismatic, and pouch.

A conventional Li-ion cell typically incorporates a graphite-based negative electrode paired with a positive electrode composed of a metal oxide or phosphate. Ionic conductivity is facilitated by an electrolyte solution consisting of a lithium salt dissolved in an organic solvent [10]. Structurally, the negative electrode (functioning as the anode during discharge) and the positive electrode (acting as the cathode) are physically isolated by a separator [11] to preclude short circuits. Finally, the connection to the external circuit is established via metallic components known as current collectors [12]. Figure 1 illustrates the fundamental operating principles and characteristics of LIBs. The underlying mechanism is relatively straightforward: during the charging phase, lithium ions are released from the positive electrode (cathode) and migrate to the negative electrode (anode). Conversely, during the discharge process, the flow is reversed, with the negative electrode supplying lithium ions back to the positive electrode [13].

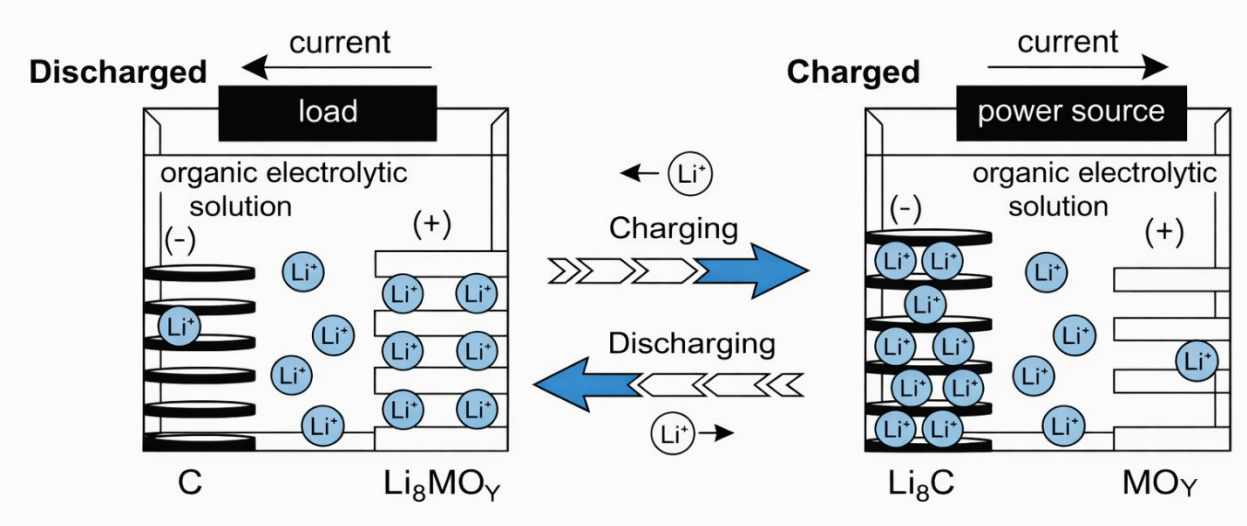

Figure 1. Working mechanism and characteristics of LIB, based on [13].

The release of stored chemical energy is facilitated by electrochemical reactions occurring at the electrode interfaces [14]. The theoretical cell voltage (ΔE) is intrinsically linked to the total Gibbs free energy change (ΔG) of these reactions, as described by the equation ($\Delta E = -\Delta G/nF$). The performance of LIBs is evaluated through critical parameters including specific energy, volumetric energy, specific capacity, abuse tolerance, and cyclability. Specific energy (Wh/kg), defined as the product of specific capacity (Ah/kg) and operating voltage (V), quantifies the energy stored per unit mass. Cyclability refers to the reversibility of the lithium-ion insertion-extraction process and is influenced by operational variables such as Depth of Discharge (DOD), State of Charge (SOC), and temperature. To maximize cycle life and mitigate risks like lithium dendrite formation which typically occurs during low-temperature charging optimal thermal and load management is essential. Furthermore, given the safety implications of multi-cell configurations, Battery Management Systems (BMS) are essential for preventing thermal runaway by detecting and isolating compromised cells [15]. Battery capacity is defined as the total quantity of electric charge a cell can deliver before its potential drops below a specific terminal voltage threshold. As an extensive property, capacity is directly proportional to the mass of active electrode material; therefore, while larger cells possess greater capacity than smaller counterparts of the same chemistry, their open-circuit voltage remains constant. This parameter is conventionally quantified in ampere-hours (Ah). Standard rated capacity is typically derived from a 20-hour discharge protocol at 20°C; for instance, a 100 Ah rating implies a sustained current of 5 A over this duration.

However, the actual fraction of extractable charge is variable, contingent upon factors such as electrochemical composition, discharge rate, ambient temperature, and storage history [16]. Charge and discharge kinetics are frequently quantified using the 'C-rate,' a metric that normalizes the electrical current relative to the battery's nominal capacity. Mathematically defined as the quotient of the applied current and the charge storage capacity, the C-rate is an invariably non-negative magnitude; thus, the direction of energy flow (charge or discharge) is inferred from the operational context [17]. To illustrate, for a battery with a 500 mAh capacity, a discharge current of 5000 mA (5 A) corresponds to a rate of 10C. Conversely, a charge current of 250 mA applied to the same unit equates to a C/2 rate, which implies a 50% increase in the SOC over a one-hour interval [18]. The C-rate, defined as the normalized charge or discharge current relative to capacity, serves as a critical determinant of battery performance and degradation kinetics. Operation at elevated C-rates accelerates electrochemical reactions, which concomitantly intensifies thermal generation and elevates internal resistance. These factors collectively contribute to accelerated aging phenomena, manifesting as irreversible capacity fading and truncated cycle life. Consequently, management and control of the C-rate is imperative to optimize operational performance while preserving the long-term health of the energy storage system [19]. The escalating demand for LIBs is driven by their widespread availability and operational reliability. Besides mitigating environmental concerns, LIBs have demonstrated significant potential across a myriad of technologies, ranging from portable consumer electronics such as mobile phones, laptops, and digital cameras to hybrid EVs. Physically characterized by high capacity, low diffusion barriers, minimal volume expansion, and high absorption energy, LIBs are distinct from alternative chemistries (e.g., Na, K, or Ca-ion) and are frequently the subject of thermal runaway modeling. Furthermore, LIBs offer superior longevity relative to conventional battery technologies, exhibiting a lifespan up to ten times longer and retaining 80% of their rated capacity after 2000 charge-discharge cycles. Notwithstanding their technological potential, LIBs are subject to significant inherent limitations. They are particularly susceptible to thermal runaway induced by high-voltage conditions, a vulnerability highlighted by high-profile safety incidents such as the grounding of the Boeing 787 fleet due to onboard battery fires. Consequently, the safety risks associated with bulk air transport have led several logistics providers to impose strict shipping embargoes. To mitigate risks like excessive voltage and internal stress, complex protective circuitry is required; however, these measures often result in increased weight and compromised

performance. Furthermore, LIBs exhibit progressive capacity fading and reliability issues due to aging. Economic factors also impede widespread adoption, as production costs remain approximately 40% higher than those of NiCd alternatives [20].

LIBs are classified into various subclasses based on the chemical structure of the cathode material employed; these materials directly determine key performance parameters such as energy density, thermal stability, cost, and cycle life. The primary cathode chemistries widely used in the industry are detailed below (Table 1) [21-25]:

Table 1. Comparison some of LIB chemistries, based on [26].

Chemistry Type	Properties
Lithium Cobalt Oxide (LCO)	LCO ($LiCoO_2$) batteries provide high specific energy, ranging from 175 to 240 Wh/kg, making them a prevalent choice for portable devices with low discharge rates, such as mobile phones and laptops. While these cells are characterized by high electrical efficiency and reasonable cost, they exhibit very low thermal stability.
Lithium Manganese Oxide (LMO)	LMO ($LiMn_2O_4$) batteries typically exhibit specific energies ranging from 100 to 150 Wh/kg. LMO batteries represent a middle ground with moderate specific energy and safety. Despite limitations such as lower efficiency and a shorter lifespan, their cost-effectiveness makes them widely applicable in power tools and medical equipment.
Lithium Iron Phosphate (LFP)	LFP ($LiFePO_4$) chemistry is distinguished by significant advantages, including extended cycle life, high current capability, and exceptional thermal stability. However, compared to other Li-ion variants, their primary limitation is lower cell voltage and specific energy. Despite this drawback, LFP batteries score highly in safety, cost-effectiveness, and lifespan.
Lithium Nickel Manganese Cobalt Oxide (NMC)	NMC batteries specific energy ranges from 100 to 150 Wh/kg, while thermal performance is enhanced. Due to their high specific energy and cost-effectiveness, NMC batteries are extensively adopted in the automotive sector (including EVs and electric powertrains) as well as in portable electronics. Overall, NMC chemistry offers a versatile solution with moderate specific power, safety, and lifespan compared to other Li-ion variants.

Lithium Nickel Cobalt Aluminum Oxide (NCA)	NCA ($Li(Ni, Co, Al)O_2$) batteries are distinguished by their superior specific capacity. NCA batteries provide high specific energy and an extended service life. However, their application is constrained by significant drawbacks, specifically high manufacturing costs and a lower safety profile.

The electrolyte solution typically constitutes a lithium salt dissolved within an organic solvent matrix [10, 11]. Fundamental to the battery's operation, this medium is primarily composed of lithium salts, solvents, and additives, the specific concentrations and types of which are critical determinants of electrochemical performance. In standard practice, a 'mixed solvent system' is employed, predominantly (95%) consisting of carbonate-based solvents. These are categorized into cyclic and linear carbonates, encompassing dimethyl carbonate (DMC), diethyl carbonate (DEC), ethyl methyl carbonate (EMC), ethylene carbonate (EC), and propylene carbonate (PC). The primary function of the solvent is to facilitate the solvation of lithium salts, such as lithium hexafluorophosphate ($LiPF_6$), and to establish conductive pathways for ionic transport. The physicochemical properties of the electrolyte, particularly viscosity and wettability, are governed by the interaction between the salt and the solvent. Generally, organic solvents exhibiting high dielectric constants and low viscosity are preferred; the former facilitates salt dissociation, while the latter enhances ionic mobility. However, owing to the inherent inverse correlation between dielectric constant and viscosity in single solvents, binary or ternary solvent mixtures are utilized to optimize the system. Consequently, the analysis of single-solvent systems serves as a prerequisite for the formulation of advanced mixed-solvent electrolytes [27].

A preeminent constraint inherent to LIB technology is its acute thermal susceptibility. Efficient operation is strictly confined to a narrow thermal window of 15–35 °C [28]; excursions beyond this operational envelope precipitate rapid electrochemical degradation and significantly heighten the probability of catastrophic failures, including combustion and explosion. Consequently, the analysis of thermal impacts is conventionally bifurcated into two distinct regimes: low-temperature and high-temperature phenomena [29-32]. Sub-zero ambient conditions (< 0 °C) exert a profound deleterious impact on the operational efficacy and cycle life of LIBs, a challenge particularly acute within the domain of electric mobility (EVs, Hybrid EVs (HEVs), and Plug-in HEVs (PHEVs)) [33, 34]. In such hypothermal environments, the electrochemical system suffers from retarded

reaction kinetics and impeded charge-transfer mechanisms [28]. This kinetic sluggishness precipitates a marked attenuation in ionic conductivity within the electrolyte [35] and inhibits Li-ion diffusivity throughout the electrode matrix [36]. Consequently, these physicochemical limitations culminate in a substantial degradation of power density and energy efficiency. Internal thermal accumulation is predominantly caused by Joule heating during aggressive operational regimes, such as high-rate charging and discharging [37, 38]. This thermal excursion causes severe performance attenuation, characterized by significant deficits in capacity and energy efficiency [39-42]. Mechanistically, capacity fading is attributed to the depletion of lithium inventory and the degradation of active materials, whereas power reduction correlates with the escalation of internal impedance [43]. To preclude the onset of thermal runaway, battery architectures must incorporate robust heat dissipation capabilities that maintain temperatures below critical safety thresholds. Breaching this thermal limit instigates irreversible structural disintegration of the electrode-electrolyte interface. Given that decomposition reactions are inherently exothermic, reaching the runaway threshold triggers a self-propagating, autocatalytic heating cycle, inevitably culminating in catastrophic cell destruction [44] and potential detonation [45, 46]. Currently, BTMS for EVs are classified into three primary categories: passive, active, and hybrid BTMS. Passive BTMS regulate battery temperature via natural physical processes, including convection and the use of phase change materials (PCMs). While these systems offer benefits such as simplicity, cost-effectiveness, and minimal energy consumption, they often lack sufficient cooling capacity for high energy density applications. In contrast, active BTMS employs external power sources such as fans and pumps to manage thermal loads. Although more complex, active systems provide superior cooling capabilities, rendering them particularly well-suited for high power battery packs and fast charging environments. Commonly employed active BTMS technologies include forced air cooling, liquid cooling, and heat pipe systems. Forced air cooling remains prevalent in low-power applications due to its structural simplicity and cost-efficiency. Conversely, liquid cooling has emerged as the mainstream solution for high-power battery packs. This technology is classified into indirect and direct (immersion) methods; however, due to safety and reliability considerations, indirect cooling is currently the dominant approach in EVs, whereas direct cooling lacks widespread adoption. A clear trend exists within liquid cooling design: complex channel geometries offer superior thermal dissipation but incur higher pressure drops and increased pumping power requirements, while simpler designs, though easier to manage, often fail to meet

the demands of fast charging. Finally, while heat pipes enhance temperature uniformity and reduce weight, their scalability is limited, and their complex integration into full battery packs remains a significant barrier to commercial automotive adoption. Hybrid BTMS, which integrate two or more distinct cooling methodologies, are designed to enhance both thermal reduction and temperature uniformity. Among the various hybrid configurations, those founded on liquid cooling are particularly prominent due to the superior heat dissipation properties of fluid media. Key iterations include combinations such as liquid-air, liquid-PCM, and liquid-heat pipe systems. While these hybrid architectures demonstrate superior thermal performance, they concurrently introduce penalties regarding system weight, manufacturing cost, and design complexity. Consequently, hybrid BTMS remains predominantly within the field of theoretical research and has yet to achieve widespread implementation in mass produced EVs [47].

The heat transfer capabilities of conventional air and water cooling systems are constrained by the inherent thermophysical properties of these fluids. To transcend these traditional limitations and enhance cooling performance, nanofluid technology has been utilized. By combining the high thermal conductivity of solid particles with the liquid flow, nanofluids play a pivotal role in the mechanism of heat removal from battery surfaces. Nanofluids are defined as engineered colloidal suspensions comprising nanometer-scale particles dispersed within a base fluid [48]. The particulate phase typically consists of metals, oxides, carbides, or carbon nanotubes, whereas the base medium is commonly selected from fluids such as water, EG [49], or oil. The commonly used base fluids and nanoparticles in nanofluid preparation are illustrated in Figure 2.

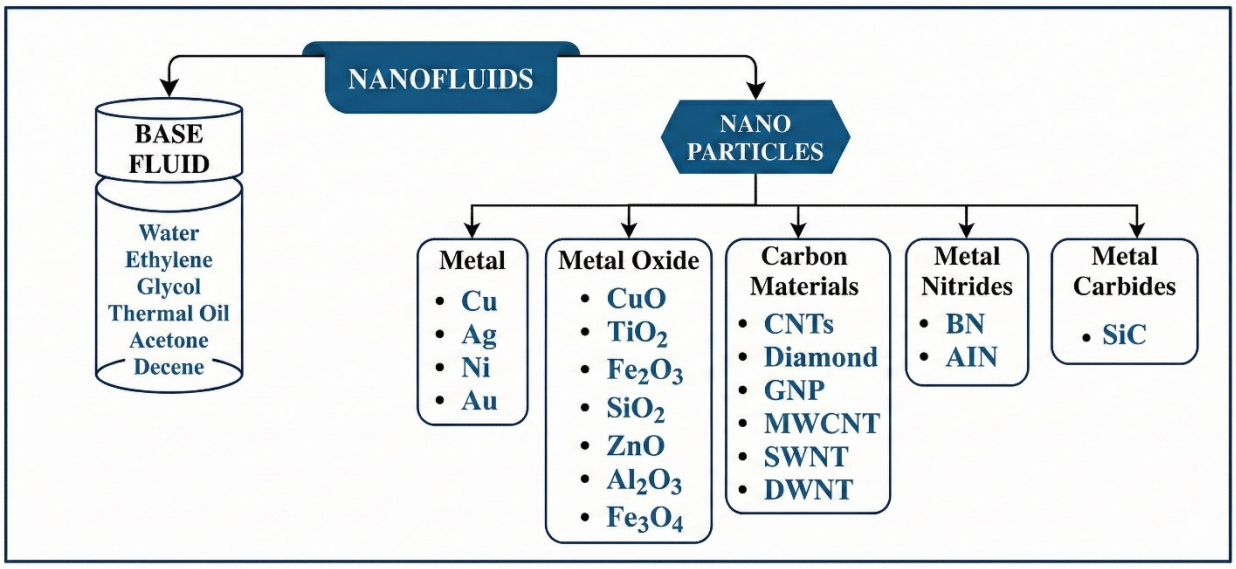

Figure 2. Schematic representation of various base fluids and nanoparticles, based on [50].

Key thermophysical attributes of nanofluids include thermal conductivity, viscosity, density, specific heat, and surface tension. The magnitude of these properties is contingent upon multiple independent variables, notably nanoparticle morphology (type, size, shape), volumetric concentration, fluid temperature, and the specific synthesis technique employed [51]. The nanoparticle volume fraction, representing the concentration of solid particles within the base fluid, is the fundamental parameter governing the thermophysical properties of nanofluids. Increasing the volume fraction significantly enhances the effective thermal conductivity of the fluid, thereby boosting heat transfer capacity and positively contributing to battery cooling performance. However, this elevation in particle concentration inevitably leads to an increase in both the viscosity and density of the fluid. Consequently, the volume fraction serves as a critical variable that dictates the trade-off between the thermal gains in heat transfer and the pressure drop (pumping power) resulting from increased viscosity. Beyond the thermophysical properties of the working fluid, the cooling performance of BTMS is directly correlated with the system's hydrodynamic and geometric parameters. In particular, the coolant inlet velocity stands out as one of the most critical dynamics, determining the convective heat transfer coefficient and, consequently, the rate of heat transfer. Similarly, the fluid inlet temperature dictates the temperature gradient between the battery and the coolant, thereby shaping the overall cooling potential. From a geometric perspective, the spacing between batteries emerges as a fundamental design variable;

it influences the flow regime and pressure drop, ultimately determining both the system's compactness and temperature uniformity.

This thesis presents a comprehensive investigation into the performance and optimization of LIBs, spanning from electrochemical modeling to thermal management strategies. First, the study examines the impact of varying C-rates on a 1D isothermal model, demonstrating how high-rate operations exacerbate internal heterogeneity, voltage spreads, and diffusion lags. Subsequently, the research evaluates the critical role of material selection, quantifying the distinct concentration gradients in polymer versus liquid electrolytes and analyzing the trade-offs between high-energy cathodes like $LiNiO_2$ and stable alternatives like LFP. Extending the analysis to thermal behavior, a 3D cylindrical model is utilized to compare cooling strategies, establishing the superior performance of liquid cooling particularly when enhanced with water-based Al_2O_3 and water-based CuO nanofluids over traditional air cooling methods. Finally, the study applies the Taguchi L9 orthogonal array methodology to optimize the BTMS. By identifying the optimal combination of coolant type, nanofluid concentration, and flow parameters, this optimization significantly minimizes the battery T_{max}, offering a robust framework for designing safer and more efficient energy storage systems.

2. LITERATURE REVIEW

2.1 Literature Review on C-rate Effect

Yüksek and Alkaya [19] investigate the critical impact of DOD and C-Rate on the long-term robustness of energy storage systems. Their simulation-based analysis reveals that while increasing these parameters accelerates battery degradation, it also opens pathways for designing customized applications by strategically balancing energy requirements with lifespan expectations. Hasan et al. [52] examine the constraints of conventional charging protocols, particularly at high C-rates such as 3C. Their findings indicate that the primary bottleneck for rapid charging performance at moderate to high operating temperatures is the transport of Li-ion within the electrolyte, manifesting as electrolyte resistance. Research into battery performance under varying rates reveals diverse degradation mechanisms. Leißing et al. [53] observed that the correlation between gassing and C-rate is largely determined by the specific type of graphite material employed. Furthermore, Snyder [54] notes that while degradation at high C-rates involves both chemical and mechanical factors, mechanical deterioration becomes increasingly dominant as the rate rises. This

is corroborated by Somerville et al. [55], whose findings indicate that charging rates exceeding 4C significantly compromise battery lifespan by altering chemical compositions. Conversely, Wang et al. [56] argue that capacity loss is primarily driven by temperature and time, with charging rates playing a negligible role in their experiments. Regarding electrode physical properties, Tran et al. [57] investigated graphite electrodes with particle sizes ranging from 6 to 44 μm. They concluded that capacity is jointly defined by the C-rate and the physical-chemical attributes linked to particle size. Similarly, Zheng et al. [58] identified a power-law relationship between electrode loading and maximum C-rate. They suggest that the rate-limiting step is not the resistance increase in thicker electrodes, but rather the diffusion of Li-ions, indicating a diffusion-dependent system. Finally, in terms of voltage stability, Li et al. [59] demonstrated that terminal voltage discrepancies remain minimal even at high rates; LCO batteries showed deviations below 50 mV at 4C, while LFP batteries maintained deviations under 50 mV even at 5C.

2.2 Literature Review on Electrode and Electrolyte Material Effect

Peng and Jiang [60] conducted a comparative simulation of five distinct LIB chemistries to evaluate their thermal properties. Their results highlight that while the LMO cell exhibits superior thermal stability, the LFP cell demonstrates the highest level of thermal safety among the variants tested. Choi et al. [61] conducted a comparative analysis of discharge characteristics, revealing that elevated discharge rates directly correlate with increased capacity loss and rising temperatures. Their findings indicate that NCM batteries are more sensitive to these rate fluctuations than LFP and LMO chemistries. However, despite this sensitivity, they conclude that NCM remains the more suitable option for EV applications due to its superior high energy density and lighter weight, whereas LFP is recommended when prioritizing thermal safety over capacity. Zheng et al. [62] provide a comparative analysis of LFP and NCA chemistries, establishing that both possess robust thermal stability. However, a divergence in performance is noted based on current density: while NCA outperforms LFP under low charge/discharge rate conditions, LFP demonstrates superior efficiency at higher rates. Consequently, the authors conclude that both materials remain viable candidates for cathode applications, depending on the specific operational requirements. The impact of electrode density on battery performance is a multifaceted subject. Shim and Striebel [63] identified a non-linear relationship, observing that capacity retention at elevated rates peaks at a density of 0.9 g/cm³ before subsequently declining. Expanding on this, Choi et al. [64] report

that while higher density improves electrical conductivity, increasing cathode density (e.g., from 1.5 to 3.5 g/cm³) significantly degrades rate capability and cyclability. This deterioration is attributed to a substantial reduction in porosity and active surface area, as confirmed by scanning electron microscope (SEM) imaging. Further nuances regarding density were highlighted by Smekens et al. [65], who found that high-density positive electrodes benefit from a 4–5% reduction in DC resistance (DCR) and offer marginally better discharge capacities at low current rates. However, for high-current applications, cells with lower electrode density demonstrate superior performance. Beyond density, diffusion kinetics and particle dynamics are critical. Chabot et al. [66] established a performance threshold, noting a marked decline in efficiency when the lithium diffusion coefficient falls below 3.9×10^{-14} m²/s. Similarly, Ye et al. [67] and Zheng et al. [58] focus on concentration gradients; they demonstrate that significant Li-ion concentration disparities within active material particles lead to a rapid drop in electrode potential, thereby prematurely limiting the cell's discharge capacity.

2.3 Literature Review on BTMS

Wiriyasart et al. [68] investigate the impact of nanofluids on thermal management, emphasizing that the movement of nanoparticles suspended in the base fluid significantly enhances cooling capacity. Their results demonstrate an inverse relationship between concentration and temperature; specifically, higher nanofluid concentrations lead to lower maximum battery temperatures. Soleymani et al. [69] revealed that the integration of nanofluids enhances heat transfer capabilities by promoting vortex development within the fluid. Through a comparative analysis, they established that Al_2O_3 nanofluids demonstrate superior thermal performance over CuO, outperforming the latter by an average of 4.37%. In terms of optimization, the study identified a 5% volume fraction as the ideal concentration for Al_2O_3 to maximize efficiency while mitigating the risk of nanoparticle clustering. Furthermore, transient analysis showed significant temperature reductions compared to the base fluid: 7.89% for Al_2O_3 and 4.73% for CuO. Although increasing fluid velocity was found to improve heat transfer via enhanced turbulence, the authors noted this comes at the cost of a higher pressure drop. Koorata and Chandrasekaran [70] investigated the thermal dynamics of battery packs under varying environmental conditions. Their analysis reveals that reducing the ambient temperature not only lowers the maximum cell temperature but also facilitates a more uniform thermal distribution across the pack. Even under aggressive operating

conditions, such as a 4C discharge rate at an ambient temperature of 38°C, the system successfully maintains the maximum temperature within the optimal range for LIBs. However, the authors note a critical trade-off regarding airflow; increasing the inlet velocity from 0.1 to 0.5 m/s reduces the peak temperature by 1°C but comes at the cost of increased power consumption (0.23 W) and a widened temperature differential of 2.3°C. Suryavanshi and Ghanegaonkar [71] investigated the geometric optimization of battery packs, identifying that a cell spacing of 2 mm yields the best cooling performance by minimizing the ventilation path and enhancing efficiency. They noted that contrary to expectation, larger spacings reduce cooling effectiveness despite providing more airflow channels. Furthermore, while they confirmed that higher discharge rates (C-rates) increase both maximum temperatures and thermal gradients, they argue that reducing the C-rate is not a practical solution due to the dynamic power demands of EVs. Yetik et al. [72] employed an L16 orthogonal array to evaluate the combined effects of inlet velocity, nanoparticle mixture ratio, C-rate, and ambient temperature on thermal performance. Their statistical analysis identifies the C-rate as the primary determinant affecting both maximum battery temperature and temperature uniformity. Conversely, while increasing the nanoparticle mixture ratio was observed to decrease the model's temperature, it was found to have the least significant impact on thermal outcomes among all the factors tested. Thorat et al. [73] emphasize the critical role of the thermophysical properties of nanofluids in maintaining battery temperatures within safe operating limits. Their study suggests that the choice of a specific nanofluid for a BTMS is not arbitrary but depends heavily on the battery pack arrangement and cell geometry. Furthermore, they report that employing nanofluids enhances cooling efficiency significantly, outperforming conventionally used fluids by 10% to 15%. Banerjee and Nidhul [74] demonstrate that the use of nanofluids leads to a significant improvement in thermal management, achieving a maximum temperature reduction of 7 K. They attribute this performance to the enhanced thermal conductivity of the fluid and the formation of a thinner thermal boundary layer, which collectively ensure a uniform temperature distribution across both high and low discharge rates. Interestingly, the study reveals a saturation point; increasing the nanofluid volume fraction from 0.1% to 0.4% does not yield a substantial further reduction in temperature. Panchal [75] investigates the geometric configuration of battery packs, concluding that a cell spacing of 2 mm provides the optimal cooling performance by minimizing the ventilation path. The study highlights a counter-intuitive finding: increasing the spacing beyond this point reduces efficiency, despite creating more airflow channels. Furthermore,

while increasing the inlet air velocity is effective in mitigating the high temperatures and thermal gradients caused by elevated discharge rates, Panchal warns of a diminishing return. Beyond a certain threshold, higher air velocities lead to increased power consumption and a decline in heat dissipation efficiency. Yetik and Karakoc [76] emphasize that the importance of nanofluid volume fraction and inlet velocity is amplified under high discharge rate conditions, primarily due to the larger temperature differentials observed in the battery model. Their individual cell analysis revealed a distinct thermal profile: temperatures are lowest near the cooling inlet, peak towards the center of the module, and decrease again at the end where the absence of adjacent cells facilitates heat loss. Furthermore, they observed that low coolant velocities exacerbate thermal non-uniformity, resulting in significant temperature disparities between individual cells. Ali et al. [77] conducted an experimental investigation simulating the cooling system (radiator) of a Toyota Yaris 2007 to evaluate the efficacy of nanofluids under various loads and concentrations. Their study concludes that to maximize heat transfer enhancement within the radiator system, the optimum nanofluid concentration is 0.01. Ozbektas et al. [78] presented a comprehensive experimental and numerical analysis of temperature estimation in Li-ion cells, utilizing Taguchi-based model parameterization. By examining key variables such as pulse time gap, discharge duration, and rest periods, they highlighted the influence of these parameters on Equivalent Circuit Model (ECM) accuracy across various thermal conditions. Their primary conclusion identifies the discharge pulse C-rate as the most critical determinant of temperature accuracy, particularly under high discharge rate conditions. Sharma et al. [79] successfully investigated the performance of a novel hybrid automotive cooling system utilizing the Peltier effect. Their study distinguishes the specific impact of operational variables on different thermal metrics. They identified flow rate as the dominant factor for maximizing thermal energy, whereas the coolant ratio was found to have the strongest influence on maximizing the Reynolds number. Regarding the convective heat transfer coefficient, the results indicate that both flow rate and coolant ratio contribute almost equally and significantly, while fan speed consistently showed a negligible effect across these performance indicators. Internal material composition and cell geometry are fundamental factors that determine the internal resistance and the resulting heat generation rate of a battery during operation, which directly dictates the required cooling capacity of a BTMS. In this context, Alrashdan [80] investigated seven control factors influencing the average electric power during the charging of LIBs, ranging from electrode thicknesses to material compositions. Through Signal-to-Noise (S/N)

ratio analysis, the study identified that the positive electrode material is the most critical determinant, exhibiting the highest delta function. The research established a clear hierarchy of influence: the positive electrode material has the greatest impact, followed in decreasing order by separator thickness, negative electrode active material volume fraction, and positive electrode thickness, with the positive electrode active material volume fraction showing the least significance. Morali et al. [81] employed thermal simulation coupled with S/N ratio analysis to quantify the relative magnitude of various discharge factors. Their statistical evaluation identifies ambient temperature (delta = 0.5593) as the primary determinant for the maximum battery temperature. In contrast, for temperature uniformity, the C-rate emerges as the most influential parameter, evidenced by a significantly higher delta value of 24.1513. Kirad and Chaudhari [82] differentiate the impacts of geometric parameters on thermal performance. They identify that the module cooling efficiency factor is primarily contingent on transverse spacing, as this dimension governs flow characteristics, convective heat transfer coefficients, and the pressure drop associated with energy consumption. Conversely, longitudinal spacing is found to be the dominant factor influencing maximum temperature and thermal variation; specifically, increasing the longitudinal gap reduces peak temperatures and promotes a more uniform thermal distribution. Shaik et al. [83] investigated the interdependent effects of cell spacing and flow characteristics on thermal performance. They observed that increasing the gap between cells from 1 mm to 4 mm, which inherently led to a rise in the Reynolds number, resulted in a significant enhancement in the average Nusselt number by 39% and 51%, respectively. This improvement is attributed to the larger temperature gradient established between the battery cells, which accelerates the overall heat transfer rate. Furthermore, the 4 mm spacing was found to alleviate flow resistance compared to the restricted 1 mm gap, thereby contributing to more efficient cooling.

3. MATERIALS AND METHODS

3.1 Physical and Chemical Properties of the 1D LIB Model

Figure 3 [84] illustrates the architecture of a standard LIB. This configuration typically utilizes a graphite intercalation compound (LiC_6) for the negative electrode and LMO for the positive electrode, though specific materials may vary. Functionally, the discharge phase involves the transport of lithium ions from the anode to the cathode via the electrolyte. Conversely, the charging phase utilizes an external power source to drive electron flow from the cathode back to the anode.

The specific chemical reactions occurring at the negative electrode are detailed in the following equations [85], where the variable 'x' represents the stoichiometry of lithium ions (Li^+) and electrons (e^-) relative to each graphite (C_6) unit.

$$Li_xC_6 \rightarrow 6C + xLi^+ + xe^- \quad (1)$$

$$6C + xLi^+ + xe^- \rightarrow Li_xC_6 \quad (2)$$

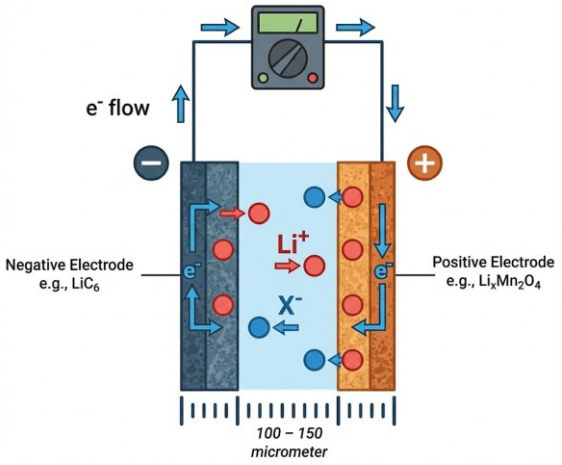

Figure 3. Schematic representation of the internal structure of a LIB, based on [84].

The specific reactions taking place at the positive electrode throughout the charging and discharging phases are described in [85]:

$$Li_{1-x}Mn_2O_4 + xLi^+ + xe^- \rightarrow LiMn_2O_4 \quad (3)$$

$$LiMn_2O_4 \rightarrow Li_{1-x}Mn_2O_4 + xLi^+ + xe^- \quad (4)$$

The simulation employs a one-dimensional (1D), isothermal model at an operating temperature of 298K, disregarding edge effects along the height and length. As shown in Figure 4, the system geometry is divided into three distinct sub-domains: a graphite negative electrode, an electrolyte, and a LMO-based positive electrode [84]. The specific dimensions for these components are 10^{-4} m for the negative electrode, 0.52×10^{-4} m for the electrolyte, and 1.74×10^{-4} m for the positive electrode. The electrolyte composition is defined as a solution of 2M $LiPF_6$ salt within a 1:2 volume ratio of EC:DMC solvent and Poly (vinylidene fluoride-hexafluoropropylene) (PVDF-HFP), utilizing standard material properties for LIBs [84].

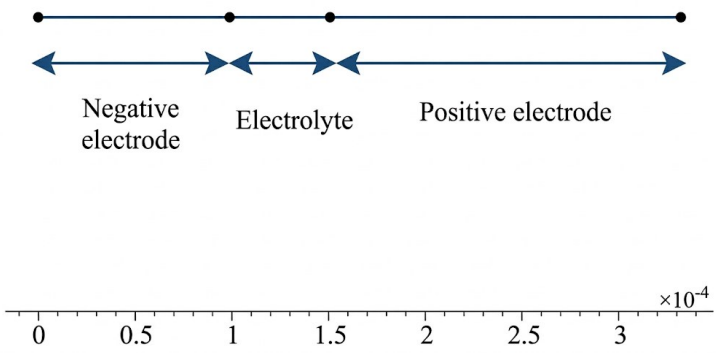

Figure 4. Schematic representation of the 1D LIB model, based on [86].

The 1D geometry of the isothermal LIB model was discretized using the mesh builder within COMSOL Multiphysics. The computational domain, with a total length of 3.26×10^{-4} m, consists of 46 edge elements and 47 mesh vertices. The mesh includes 4 vertex elements defining the boundaries of the internal domains. The element length ratio of the generated mesh is 0.2741 (defined as the ratio of the minimum element length to the maximum element length), ensuring appropriate spatial resolution for the numerical solution [84].

As depicted in Figure 5, the simulation follows a specific load profile based on Ref. [87]. The protocol commences with a discharge phase of 17.5 A/m² for a duration of 2000 s, succeeded by a 300 s relaxation (open circuit) period. Subsequently, a charging phase is applied for 2000 s at an equivalent current density, before the cycle terminates with a final rest period extending to 8000 s.

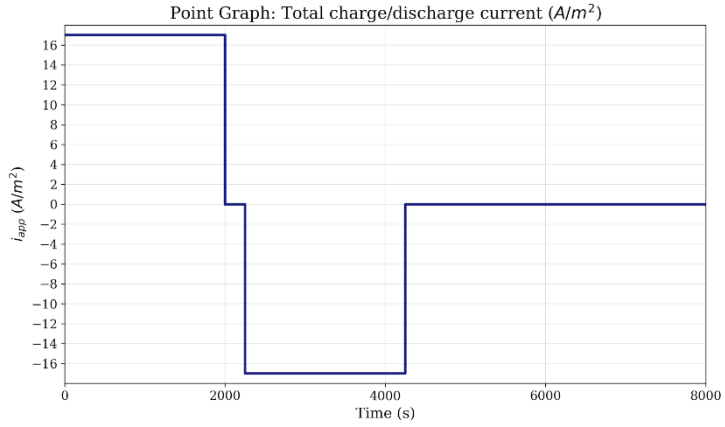

Figure 5. The simulated current load profile applied to the battery model, based on [86].

3.2 Numerical Method of the 1D LIB Model

The mathematical framework detailed in Section 3.2 adopts the 1D isothermal Li-ion battery model [84] available in COMSOL Multiphysics. These governing equations characterize the transport of charge and current distribution across both the electrode and electrolyte domains, based fundamentally on the conservation of mass and charge.

$$\nabla \cdot J_l = R_l \tag{5}$$

$$\nabla \cdot i_l = Q_l \tag{6}$$

$$\nabla \cdot i_s = Q_s \tag{7}$$

In these expressions, J_l represents the Li-ion flux within the electrolyte phase. The current densities are denoted by i_l for the ionic current in the electrolyte and i_s for the electronic current within the solid electrode. Finally, R_l, Q_l, and Q_s serve as the source terms associated with the electrochemical reactions.

$$J_l = -D_l \nabla c_l + \frac{i_l t_+}{F} \tag{8}$$

Equation 8 characterizes the total flux of Li-ions within the electrolyte phase. This expression combines two transport mechanisms: a diffusion term ($-D_l \nabla c_l$), which addresses ion movement driven by concentration gradients, and a migration term ($\frac{i_l t_+}{F}$), which describes movement induced by the electric field. In this equation, D_l represents the diffusion coefficient, c_l is the Li-ion concentration, t_+ denotes the transference number, and F is Faraday's constant.

The subsequent equation defines the ionic current within the electrolyte,

$$i_l = -\sigma_l \nabla \phi_l + \frac{2\sigma_l RT}{F}\left(1 + \frac{\partial ln f}{\partial ln c_l}\right)(1 - t_+)\nabla ln c_l \tag{9}$$

The equation includes two primary components:

- Conductive term: Expressed as $-\sigma_l \nabla \phi_l$, this term represents the migration of charged species driven by the electric potential gradient.

- Concentration gradient term: Expressed as $\frac{2\sigma_l RT}{F}\left(1+\frac{\partial lnf}{\partial lnc_l}\right)(1-t_+)\nabla lnc_l$, this term accounts for the dependency of ionic conductivity on concentration variances.

In this context, σ_l denotes the ionic conductivity, ϕ_l is the electrolyte potential, R represents the universal gas constant, T is the temperature, and f is the activity coefficient. Additionally, $c_{s,init}$ is defined as the initial concentration of the species at the start of the simulation.

$$\mathbf{i}_s = -\sigma_s \nabla \phi_s \tag{10}$$

This expression is governed by Ohm's law and characterizes the electronic current within the solid electrode phase. Here, σ_s represents the electrical conductivity of the solid material, while ϕ_s denotes the electrode potential.

$$-n \cdot J_l = 0 \tag{11}$$

This expression defines a no-flux boundary condition for the Li-ion flux (J_l) at the specified surface. The variable n denotes the unit normal vector, which is directed outward from the computational domain.

$$-n \cdot i_l = 0 \tag{12}$$

$$-n \cdot i_s = 0 \tag{13}$$

This system of equations constitutes a mathematical framework characterizing the current distribution and transport phenomena within a porous electrode, an approach widely adopted in the modeling of batteries and electrochemical systems.

The conservation of charge within both the electrolyte and solid phases is governed by the following expressions:

$$\nabla \cdot J_l = R_l, \qquad R_l = -\sum_m \frac{\nu_{Li+,m} i_{v,m}}{F} + R_{l,src} \tag{14}$$

The following equations quantify the consumption or production of Li-ions resulting from electrochemical reactions. In this context, $i_{v,\,\text{total}}$ denotes the total volumetric current density, which is directly proportional to the reaction rates.

$$\nabla \cdot i_l = i_{v,\,total} + Q_l \tag{15}$$

$$\nabla \cdot i_s = -i_{v,\,total} + Q_s \tag{16}$$

The effective transport properties are defined by the subsequent equations, where f_l represents the volume fraction of the electrolyte phase.

$$D_{l,eff} = f_l D_l, \qquad \sigma_{l,\,eff} = f_l \sigma_l, \qquad \sigma_{s,\,eff} = \sigma_s \tag{17}$$

Equation 18 defines the total volumetric current density. In this expression, $i_{v,m}$ represents the contributions from reaction current density, while $i_{v,dl}$ denotes the double-layer current, which accounts for capacitive effects at the interfaces.

$$i_{v,\,total} = \sum_m i_{v,m} + i_{v,dl} \tag{18}$$

In the context of potential losses, the overpotential (η) acts as the thermodynamic driving force for electrochemical reactions, allowing them to proceed by surpassing equilibrium conditions. The equilibrium potential (E_{eq}) represents the material-dependent voltage in a no-current state, whereas the charge transfer potential (E_{ct}) denotes the actual potential difference observed during operation. The definition of E_{ct} is provided in Eq. 20:

$$\eta = E_{ct} - E_{eq} \tag{19}$$

$$E_{ct} = \phi_s - \phi_l \tag{20}$$

Charge transfer at the electrode-electrolyte interface is governed by the electric potential difference between the solid phase and the liquid electrolyte. Consequently, the volumetric current density (i_v) is defined as:

$$i_v = a_v i_{loc} \tag{21}$$

This relationship bridges the gap between microscopic reaction rates and macroscopic performance in porous structures by utilizing the following parameters:

- i_v (volumetric current density): Measured in A/m³, this represents the current per unit volume, a crucial metric for high-surface-area porous electrodes.
- a_v (specific surface area): Measured in m²/m³, this quantifies the available reactive surface area within a given volume.
- i_{loc} (local current density): Measured in A/m², this denotes the current generated per unit surface area at specific reaction sites.

Equation 22 establishes a boundary condition within the framework of electrochemical system modeling.

$$\phi_s = 0 \tag{22}$$

Equation 23 serves as the boundary condition that enforces current continuity at the interface of the porous electrode.

$$-n \cdot i_s = i_{n,\,s} \tag{23}$$

i_n (normal current density): A scalar value quantifying the current flowing per unit area perpendicular to the surface boundary.

Subscript s: Denotes properties associated with the surface boundary.

3.3 1D LIB Model Validation with the Experimental Results

Based on the foundational work of Doyle et al. [88], the model utilizes a nominal discharge current density of 17.5 A/m^2 at 1C (representing a theoretical one-hour full discharge). By definition, a 17.5 Ah cell is theoretically capable of providing 17.5 A for one hour, 1.75 A (C/10) for ten hours, or achieving complete discharge in approximately six minutes at a 10 C-rate, though actual

discharge relationships are non-linear. The numerical model [89] was developed using the COMSOL Multiphysics Battery Design Module and validated against experimental data [88] across three distinct C-rates. As demonstrated in Figure 6, there is a strong correlation, with numerical and experimental results overlapping.

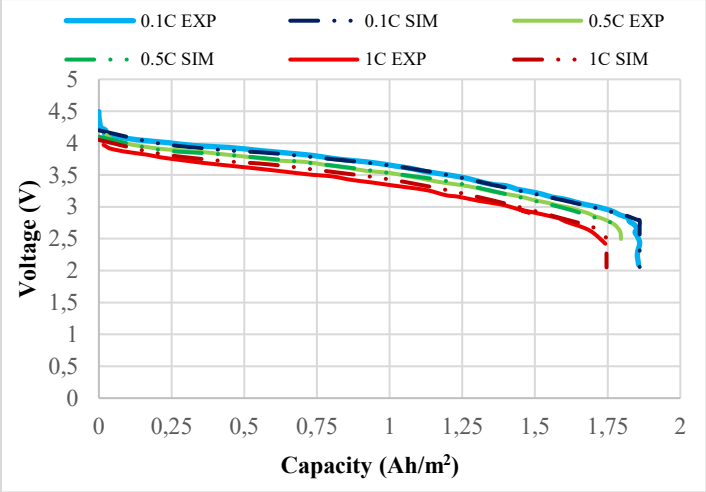

Figure 6. Cell potential (V) shown as a function of capacity (Ah/m^2) under various discharge rates.

3.4 Physical and Chemical Properties of the 3D LIB Model

The simulation centers on an air-cooled, cylindrical 18650 battery (18 mm diameter, 65 mm height). To optimize computational efficiency, a 1D model handles the internal electrochemical processes of the active cell, while a 3D model resolves the thermal behavior and cooling fluid flow. To accurately replicate pack-level thermal interactions, the computational domain includes the primary active cell surrounded by partial sections of neighboring cells (e.g., the ¼ section shown in Figure 7). 3 × r_batt (9 mm) is maintained between the main cell and its neighbors. Crucially, the 1D electrochemical model is exclusive to the main cell; neighboring sections function solely as passive thermal masses to establish realistic boundary conditions. Heat transfer and fluid motion are linked via the Nonisothermal Flow Multiphysics interface. However, because fluid properties are treated as temperature-independent, the model utilizes a one-way coupling approach. The simulation employs the LIB interface to define the cell's electrochemical properties, comprising a negative porous electrode (Li_xC_6 MCMB, 55 µm), a separator (30 µm), and a positive porous electrode ($LiFePO_4$, 55 µm). To link the physics, the model calculates the average temperature of

the active battery material using a nonlocal integration coupling. Simultaneously, the Heat Transfer in Solids and Fluids interface governs the 3D thermal behavior. As depicted in Figure 7, the thermal geometry includes four distinct domains: the active battery material (wound sheets, r=9 mm, h=65 mm), a central nylon mandrel (r=2 mm), a top-mounted aluminum connector (3 mm thick), and the surrounding flow compartment (air or liquid).

Limitations of the Study;

While the developed 3D thermal model provides significant insights into the battery's thermal behavior, the following limitations associated with the computational method and assumptions must be considered:

1. Unidirectional Flow-Thermal Coupling: The simulation employs a one-way coupling strategy where the fluid flow is solved first as a stationary step, and the resulting velocity field is used for the time-dependent thermal analysis. This approach assumes that the cooling air properties (density and viscosity) do not change significantly with temperature. Consequently, the effect of buoyancy-driven natural convection or the alteration of flow patterns due to heat rejection from the battery surface is neglected.

2. Geometric Simplification of the Canister: To reduce computational cost, the outer steel canister of the battery was not modeled as a separate physical domain. Instead, its thermal influence was approximated by scaling the volumetric heat source within the active material. This simplification ignores the specific thermal contact resistance between the jelly-roll and the canister case.

3. Averaged Electrochemical Coupling: The coupling between the 1D electrochemical model and the 3D thermal model relies on the volume-averaged temperature of the active material. The electrochemical reaction rates in the 1D model are therefore uniform, neglecting local variations in reaction kinetics that might occur due to radial thermal gradients (e.g., the core being hotter than the surface).

4. Homogenized Active Material: The spiral wound structure (jelly-roll) consists of discrete layers of anode, cathode, and separator, but was modeled as a homogenized cylinder with anisotropic thermal conductivity. This approach accurately predicts macro-scale thermal gradients but cannot capture micro-scale hotspots resulting from potential localized defects or winding irregularities.

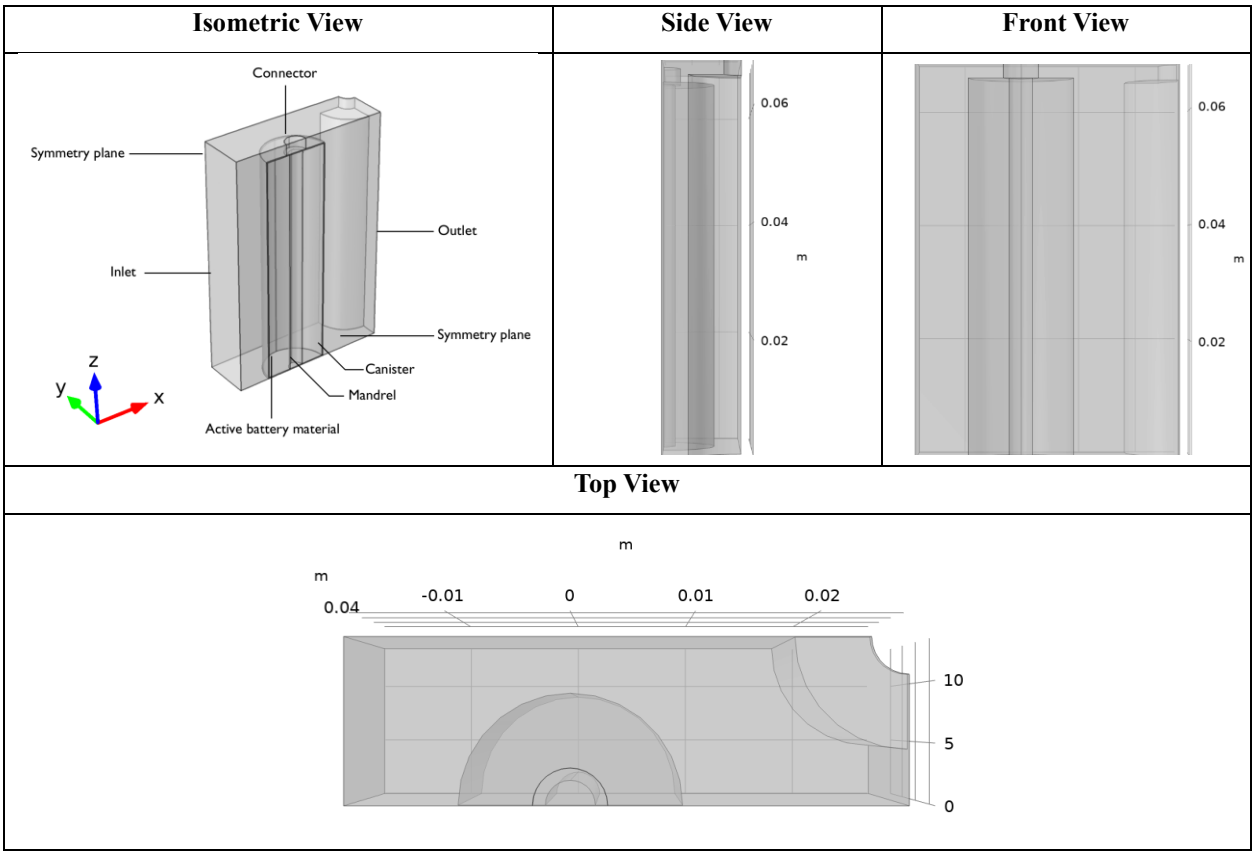

Figure 7. Geometry of the thermal model, based on [90].

As shown in Figure 8, a boundary layer mesh consisting of two layers (2×10^{-4} m thickness, 1.2 stretching factor) was applied to the channel walls to resolve gradients at the fluid-solid boundaries. The mandrel and active battery material were discretized using a swept technique with triangular face meshing, which generated prismatic elements, while the z-direction was assigned a fixed distribution of 10 elements for consistency. In total, the mesh contains 43,405 domain elements (predominantly tetrahedra and prisms), 5,429 boundary elements, and 481 edge elements. The discretization quality was verified via the skewness metric, resulting in an average score of 0.7044, which confirms a high-quality grid capable of mitigating numerical diffusion.

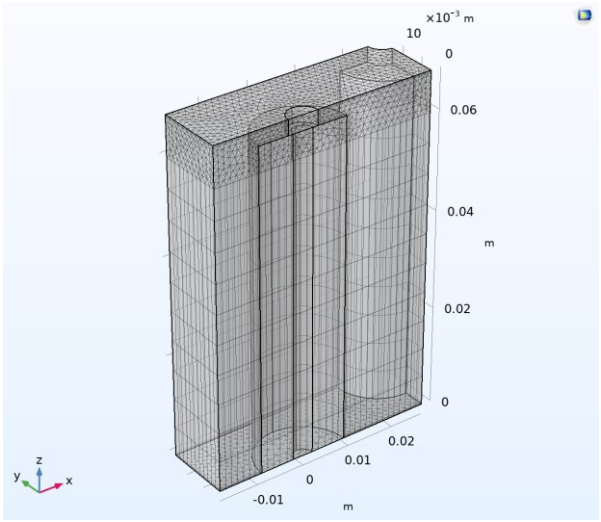

Figure 8. 3D hybrid mesh structure of the LIB cell in COMSOL Multiphysics, based on [90].

The simulation is initialized with a uniform temperature of 298.15 K. Boundary conditions include an inlet velocity of 0.1 m/s (for air cooling), a fixed outlet pressure of 1 atm, symmetry conditions on the respective planes, and no-slip conditions on the battery walls. The solution methodology follows a three-step sequence: first, computing the steady-state laminar flow at 298.15 K; second, evaluating the initial electrochemical potentials at $t=0$; and third, conducting a time-dependent analysis of the fully coupled system [90].

In the COMSOL Multiphysics analyses, the selection of the flow model was based on the calculated Reynolds numbers. The Reynolds numbers were determined to be approximately 133 for air (at 0.1 m/s) and 1541 for water-based fluids (at 0.05 m/s). Although the water-based fluid flow remains below the traditional critical threshold for turbulence, the Turbulent Flow (k-ε) interface was specifically utilized for these cases. This selection was made to conservatively account for potential local flow instabilities, enhanced mixing effects, and the significantly higher momentum associated with the liquid coolant compared to air. Comparative tests confirmed that employing turbulence modeling for the liquid coolant yielded results consistent with the laminar assumption, further validating the reliability of the modeling approach.

3.5 Numerical Method of the 3D LIB Model

The 3D thermal analysis of the cylindrical LIB integrates two distinct modeling components. The electrochemical behavior is simulated using a 1D Cell Model via the LIB interface [84], a method

further referenced in [89] and [91]. Simultaneously, the thermal dynamics are resolved using a 3D Thermal Model within the Heat Transfer in Solids and Fluids interface. The mathematical framework for this COMSOL Multiphysics implementation follows the equations [90] outlined in Section 3.5.

Eq. 24, 25 and 26 govern the fluid dynamics of the coolant employed for the battery's thermal management, under the assumptions of steady-state and incompressible flow.

$$\rho(\mathrm{u} \cdot \nabla)\mathrm{u} = \nabla \cdot [-p\mathrm{I} + \mathrm{K}] + \mathrm{F} \tag{24}$$

$$\rho \nabla \cdot \mathrm{u} = 0 \tag{25}$$

- ρ: Fluid density (coolant).
- u: Fluid velocity vector.
- ∇: The Nabla operator, representing spatial derivatives (gradient, divergence).
- p: Fluid pressure.
- I: The identity tensor.
- K: The viscous stress tensor, defined below.
- F: Volume force vector (e.g., gravity).

$$\mathrm{K} = \mu(\nabla \mathrm{u} + (\nabla \mathrm{u})^{\mathrm{T}}) \tag{26}$$

- μ: Fluid dynamic viscosity (e.g., Pa·s). It is a measure of the fluid's resistance to flow.
- ∇u: The velocity gradient tensor.
- $(\nabla \mathrm{u})^{\mathrm{T}}$: The transpose of the velocity gradient tensor.

Eq. 27 is essential for defining the boundary behavior in fluid dynamic systems.

$$\mathrm{u} = 0 \tag{27}$$

This defines the no-slip boundary condition, which is applied to the battery walls.

Eq. 28 and 29 define the pressure-outlet boundary condition within the COMSOL Laminar Flow interface, applied at the outlet of the flow compartment to maintain a constant pressure of 1 atm.

$$\mathrm{n}^{\mathrm{T}}[-p\mathrm{I}+\mathrm{K}]\mathrm{n}=-\hat{p_0} \tag{28}$$

$$\hat{p_0} \leq p_0, \mathrm{u}\cdot\mathrm{t}=0 \tag{29}$$

- n: The unit vector normal (perpendicular) to the boundary, pointing outward from the fluid domain.
- $-p\mathrm{I}+\mathrm{K}$: Total stress tensor acting on the fluid. It combines the pressure stress ($-p\mathrm{I}$) and the viscous stress (K).
- $-p_0$: This is a prescribed external pressure acting on the boundary from the outside.

Eq. 30 defines the velocity-inlet boundary condition, applied at the inlet of the flow compartment.

$$\mathrm{u}=-U_0\mathrm{n} \tag{30}$$

- u: The fluid velocity vector at the boundary.
- U_0: A constant value representing the speed or velocity magnitude.

Eq. 31 and 32 define the symmetry boundary condition applied to the symmetry planes of the domain to reflect the battery matrix arrangement.

$$\mathrm{u}\cdot\mathrm{n}=0 \tag{31}$$

$$\mathrm{K_n}-(\mathrm{K_n}\cdot\mathrm{n})\mathrm{n}=0, \mathrm{K_n}=\mathrm{Kn} \tag{32}$$

- K: The viscous stress tensor ($\mathrm{K}=\mu(\nabla\mathrm{u}+(\nabla\mathrm{u})^{\mathrm{T}})$).
- Kn: The total viscous stress vector acting on the boundary.
- $(\mathrm{Kn}\cdot\mathrm{n})\mathrm{n}$: The component of that stress that is normal to the boundary.

The following expressions represent the governing equations for the Heat Transfer physics. In this model, a one-way coupling approach is utilized where the Laminar Flow is initially solved in a

steady-state step to define the velocity field. Subsequently, this field is coupled with the time-dependent energy equation to compute the battery's thermal response.

$$\rho C_p \mathrm{u} \cdot \nabla T + \nabla \cdot \mathrm{q} = Q + Q_{\mathrm{ted}} \quad (33)$$

$$\mathrm{q} = -k \cdot \nabla T. \quad (34)$$

- $\rho C_p \mathrm{u} \cdot \nabla T$: Convective Heat Transfer.
    - ρ: Material density.
    - C_p: Specific heat capacity.
    - u: Velocity vector field (from the Laminar Flow solution).
    - ∇T: Temperature gradient.
- $\nabla \cdot \mathrm{q}$: Conductive Heat Transfer (the divergence of the heat flux).
    - This term represents how heat diffuses through the materials due to temperature differences.
- $Q + Q_{ted}$: Heat Sources.
    - Q: The main heat source from the battery electrochemistry (Joule heating, reaction heat).
    - Q_{ted}: Thermo-electric dissipation (Joule heating from electric currents, often negligible in battery models compared to the electrochemical heating).
- q: Heat flux vector (direction and magnitude of heat flow).
- k: Material thermal conductivity.
- ∇T: Temperature gradient.
- $-$ **sign**: Indicates that heat flows from high temperature to low temperature.

Eq. 33 and 34 serve as the governing heat transfer equations for the solid domains (active battery material, mandrel, and connector). In contrast, Eq. 35 and 36 represent the energy balance for the fluid domain (cooling air), where Eq. 36 explicitly accounts for the fluid density variation using the ideal gas law.

$$\rho C_p \mathrm{u} \cdot \nabla T + \nabla \cdot \mathrm{q} = Q + Q_p + Q_{\mathrm{vd}} \tag{35}$$

$$\rho = \frac{p_{\mathrm{A}}}{R_{\mathrm{s}} T} \text{ in ideal gas domains} \tag{36}$$

- Left Side - Heat Transport:
  - $\rho C_p \mathrm{u} \cdot \nabla T$: Convective heat transfer - heat carried by fluid flow.
  - $\nabla \cdot \mathrm{q}$: Conductive heat transfer - heat diffusion through materials.
- Right Side - Heat Sources:
  - Q: General heat source (from battery electrochemistry).
  - Q_p: Pressure work - heating from fluid compression/expansion.
  - Q_{vd}: Viscous dissipation - heating from fluid friction.
- ρ: Gas density.
- ρ_A: Reference density at a reference state.
- R_s: Specific gas constant.
- T: Absolute temperature.

Eq. 37 defines the adiabatic (zero heat flux) boundary condition, which is applied to all external boundaries of the flow compartment excluding the inlet and outlet as well as the symmetry planes, to represent thermal insulation from the ambient environment.

$$-\mathrm{n} \cdot \mathrm{q} = 0 \tag{37}$$

Eq. 38 defines the volumetric heat source applied to the active battery material domain. This term incorporates the heat generated during electrochemical cycles, scaled from the 1D cell model, to drive the transient temperature distribution in the 3D thermal model.

$$Q = Q_0 \tag{38}$$

- Q: The heat flux (heat flow per unit area) at the boundary.
- Q_0: A constant value specifying the magnitude of the heat flux.

Eq. 39 defines the fixed temperature boundary condition, which is applied to the inlet of the flow compartment. It maintains the incoming cooling air at a constant prescribed temperature of 298.15 K throughout the simulation.

$$T = T_0 \tag{39}$$

- T: The temperature at the boundary.
- T_0: A constant value specifying the prescribed temperature.

Eq. 40 shows a specific heat source term in the fluid flow model.

$$Q_{\mathrm{vd}} = \tau : \nabla \mathrm{u} \tag{40}$$

- Q_{vd}: The heat generated per unit volume due to viscous dissipation.
- τ: The viscous stress tensor.
- ∇u: The velocity gradient tensor.

3.6 Nanofluid Properties Calculation

Table 2 displays the thermophysical properties of the nanofluids, which were determined using equations derived from the base fluids (water and a 30:70 mixture of EG and water (EGW) [92]) and specific nanoparticles (Al_2O_3 and CuO [93–95]). The same calculation methodology was applied to determine the properties for the 2% and 3% Al_2O_3–W volume fractions.

The density of the nanofluid is determined using the Pak and Cho mixture theory model [96]. This model calculates (Eq. 41) density as a weighted average of the base fluid and nanoparticle densities, proportional to their respective volume fractions.

$$\rho_{nf} = (1 - \phi)\rho_{bf} + \phi\rho_p \tag{41}$$

- ρ_{nf} : Nanofluid density.
- ρ_{bf} : Base fluid density.
- ρ_p : Nanoparticles density.
- ϕ : Nanoparticles volume fraction.

The thermal equilibrium model [97] assumes that the nanoparticles and the base fluid share the same temperature. Consequently, this equation calculates the resulting property as a mass-weighted average of the two components.

$$c_{p,nf} = \frac{(1-\phi)\rho_{bf}c_{p,bf} + \phi\rho_p c_{p,p}}{\rho_{nf}} \tag{42}$$

- $c_{p,nf}$: Nanofluid specific heat capacity.
- $c_{p,bf}$: Base fluid specific heat capacity.
- $c_{p,p}$: Nanoparticles specific heat capacity.

The Maxwell model [98] (Eq. 43) is utilized to estimate the effective thermal conductivity of dilute suspensions containing spherical solid particles.

$$k_{nf} = k_{bf}\left[\frac{k_p + 2k_{bf} - 2\phi\left(k_{bf} - k_p\right)}{k_p + 2k_{bf} + \phi\left(k_{bf} - k_p\right)}\right] \tag{43}$$

- k_{nf} : Nanofluid thermal conductivity.
- k_{bf} : Base fluid thermal conductivity.
- k_p : Nanoparticles thermal conductivity.

The Brinkman model [99] (Eq. 44) is employed to quantify the increase in effective viscosity resulting from the suspension of spherical solid particles in a dilute mixture.

$$\mu_{nf} = \frac{\mu_{bf}}{(1-\phi)^{2.5}} \tag{44}$$

- μ_{nf} : Nanofluid dynamic viscosity.
- μ_{bf} : Base fluid dynamic viscosity.

Table 2. Properties of the Coolants.

	Nanofluids			
Properties	5% Al_2O_3 - W	5% CuO - W	5% Al_2O_3 - EGW	5% CuO - EGW
Density [kg/m^3]	1146.2	1272.68	1169.4	1295.9
Specific Heat [J/(kg.K)]	3574.8	3254.56	3253	2883.33
Thermal Conductivity [W/(m.K)]	0.707	0.7126	0.547	0.5512
Dynamic Viscosity [Pa.s]	0.0010095	0.00101	0.00079	0.00079

3.7 3D LIB Model Validation with the Experimental Results

To validate the numerical COMSOL model developed for the air-cooled cylindrical battery, the results were compared against the experimental data [100] provided by Panchal et al. Experimental data from a commercial 18,650 cylindrical Li-ion cell ($LiFePO_4$/Graphite) was utilized as the reference. The validation experiments were conducted under a controlled ambient temperature of 298 K with air cooling. The experimental setup consisted of a high-precision battery testing system and a thermal data acquisition unit. The cell was cycled using an A & D Bitrode cell cycler (providing charge/discharge control) within a voltage window of 2.0 V to 3.6 V. To ensure reliable electrical contact and minimize resistance, aluminum connectors were employed at the terminals. Thermal characterization was performed using T-type thermocouples (30 gauge, special limits of error) with a measurement uncertainty of approximately ±1°C. These sensors were strategically placed on the cell surface (anode, cathode, and mid-surface) and connected to a national instruments field point (NI-FP-TC-120) data acquisition system to record transient temperature

profiles [100]. As shown in Figure 9, the battery temperature change (ΔT) over time demonstrates a strong agreement between the simulation and the experimental measurements [100].

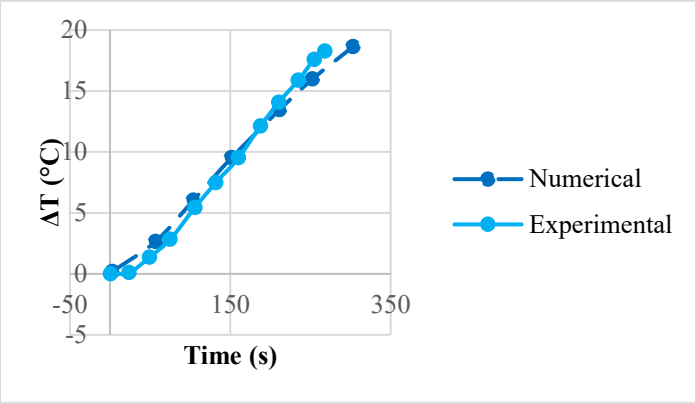

Figure 9. Validation of numerical ΔT (°C) curves against experimental data from [100].

3.8 Application of the Taguchi Method for Parameter Selection

Losses due to functional variation are defined as the losses incurred when a product's performance deviates from its intended target value. This deviation is driven by uncontrollable elements known as noise factors, which are categorized into external influences (such as ambient temperature or human error), manufacturing discrepancies (such as unit-to-unit variance), and product degradation over time. The primary objective of quality engineering is to develop products that remain robust despite these noise factors. Consequently, the selection of control factors represents the most critical phase in experimental design. It is advisable to incorporate as many factors as possible to facilitate the early identification of insignificant variables. To meet this requirement, the Taguchi method employs standard orthogonal arrays [101].

The Taguchi method is a robust optimization technique widely utilized in both industrial and scientific sectors to achieve optimal results efficiently by minimizing the number of required experiments. In the context of this study, the method was applied to accelerate the optimization process by reducing the number of numerical analyses. The approach relies on an orthogonal array design to systematically evaluate specific parameter combinations and their respective levels [102]. Central to this method is the S/N ratio calculated as the ratio of the mean (signal) to the standard deviation (noise) which serves as a quantitative indicator of process quality [103].

The S/N ratio is expressed using three different equations [101]. These are:

Smaller is better;

$$S/N = -10\log \frac{1}{n}\left(\sum y^2\right) \tag{45}$$

Larger is better;

$$S/N = -10\log \frac{1}{n}\left(\sum \frac{1}{y^2}\right) \tag{46}$$

Nominal is best;

$$S/N = 10\log \frac{\vec{y}}{S_y^2} \tag{47}$$

Where y represents the observed data, $\vec{y}$ denotes the mean value of y, S_y^2 indicates the variance of y, and n is the total number of observations.

Given that the primary objective of this study is to minimize the T_{max} of the battery, the "smaller-is-better" criterion was selected for the Taguchi optimization.

A conventional full factorial design involving four control factors at three levels would require 3^4=81 distinct numerical analyses to determine their impact on the battery's T_{max}. However, by employing the Taguchi optimization method, the requisite number of experiments was significantly reduced, allowing the optimal design to be identified more efficiently. The specific parameters and their corresponding levels are outlined in Table 3.

Table 3. Optimization parameters and their corresponding levels.

Parameters	Level 1	Level 2	Level 3
Base Fluid (A)	EG	EGW [92]	W
Φ-Al_2O_3 [93-95] (B)	2%	3%	5%
Battery-Battery Distance (C)	2.5 × r_batt (9 mm)	3 × r_batt	3.5 × r_batt
T_{inlet} (D)	293.15 K	298.15 K	303.15 K

The L9 orthogonal array (generated by Minitab software) shown in Table 4 provides a systematic way to test four factors (A, B, C, and D) using only nine experimental runs instead of the 81 required for a full factorial design. In this table, the numerical values 1, 2, and 3 represent the specific levels defined in Table 3. For instance, in experimental run L1, all factors are set to their first level (Base Fluid: EG, Concentration: 2%, Distance: 2.5 × r_batt, and T_{inlet}: 293.15 K). This balanced arrangement ensures that each level of every factor is tested equally against the levels of other factors, allowing for an independent evaluation of each parameter's main effect on the battery's maximum temperature.

Table 4. Structure of the L9 orthogonal array with four control factors and three levels.

Orthogonal Design	A	B	C	D
L1	1	1	1	1
L2	1	2	2	2
L3	1	3	3	3
L4	2	1	2	3
L5	2	2	3	1
L6	2	3	1	2
L7	3	1	3	2
L8	3	2	1	3
L9	3	3	2	1

4. RESULTS

4.1 C-Rate Effect on 1D LIB

A 1D isothermal LIB was modeled using COMSOL Multiphysics to investigate performance under various C-rates [89]. As shown in Figure 10, the initial voltage is closely aligned at approximately 4 V across all cases, though a slight decrease is observed as the C-rate increases. These voltage profiles correspond with the 0.1C, 0.5C, and 1C data presented in Figure 6. The results demonstrate that increasing the C-rate proportionally raises the cell current density, thereby reducing discharge and charge durations.

The temporal scaling of the discharge, open circuit voltage (OCV), and charge phases is evident in Figure 10. Using the 1C rate as a baseline where phases occur at 0–2000 s, 2000–2300 s, and 2300–4300 s, respectively the timing scales inversely with the C-rate. For example, at 0.1C, the duration increases tenfold (discharge ending at 20000 s). Conversely, at higher rates, the process accelerates: the 2C rate concludes the discharge phase at 1000 s, while the 3C rate reduces the discharge, OCV, and charge periods to 0–666.66 s, 666.66–766.66 s, and 766.66–1433.33 s, respectively.

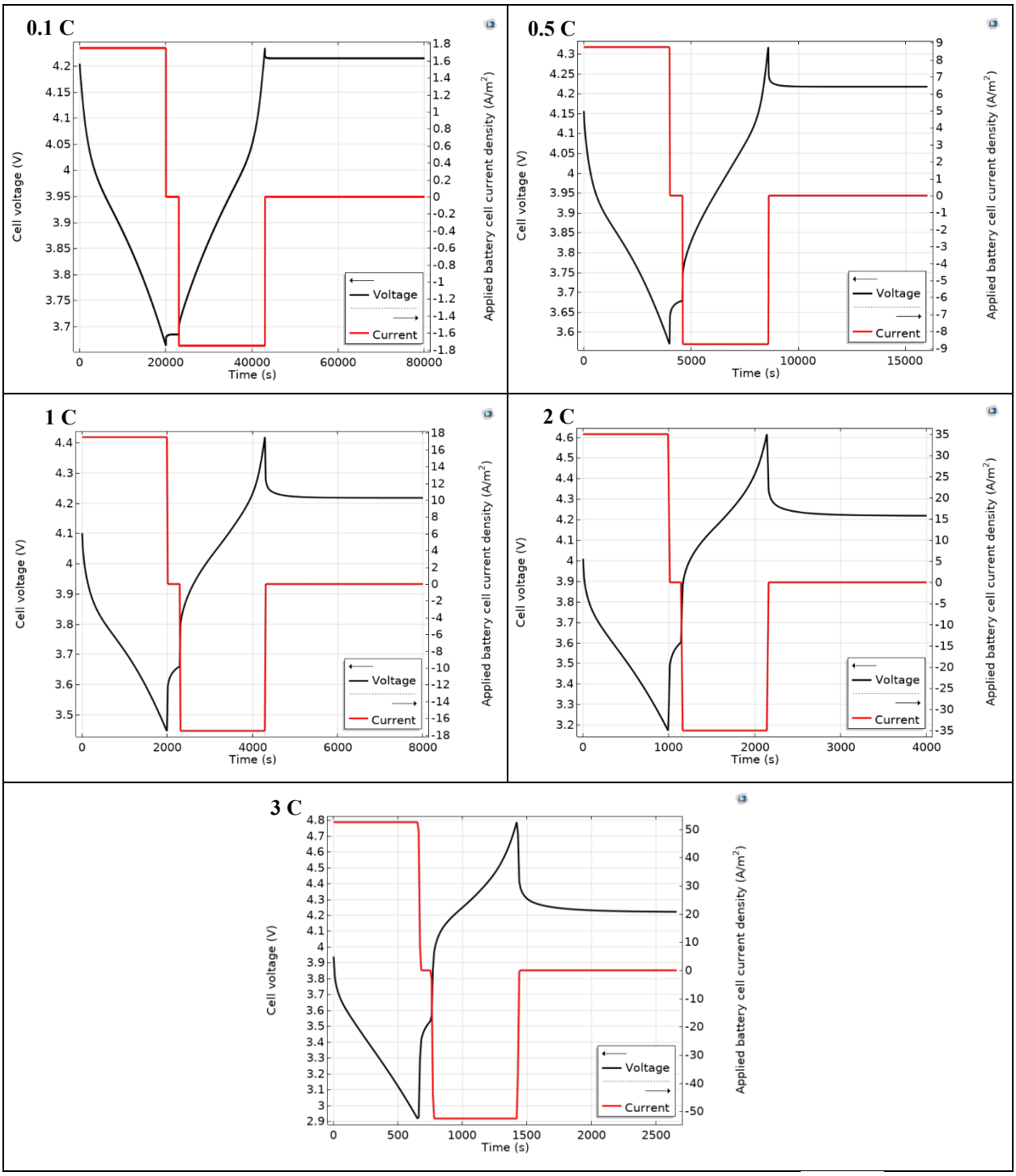

Figure 10. Voltage and current profiles during load cycles applied at five distinct C-rates.

To ensure an accurate comparison of the data presented in Figures 11, 12, and 14, time points of 10 s, 100 s, and 300 s were selected, as these fall within the discharge phase for all C-rates (refer to Figure 10). An analysis of Figure 11 and Table 5 indicates that the electrolyte voltage declines across all battery domains the negative electrode, electrolyte, and positive electrode during the first

300 seconds of discharge. Furthermore, the data demonstrates that as the C-rate increases, the rate of voltage drop accelerates across all three components.

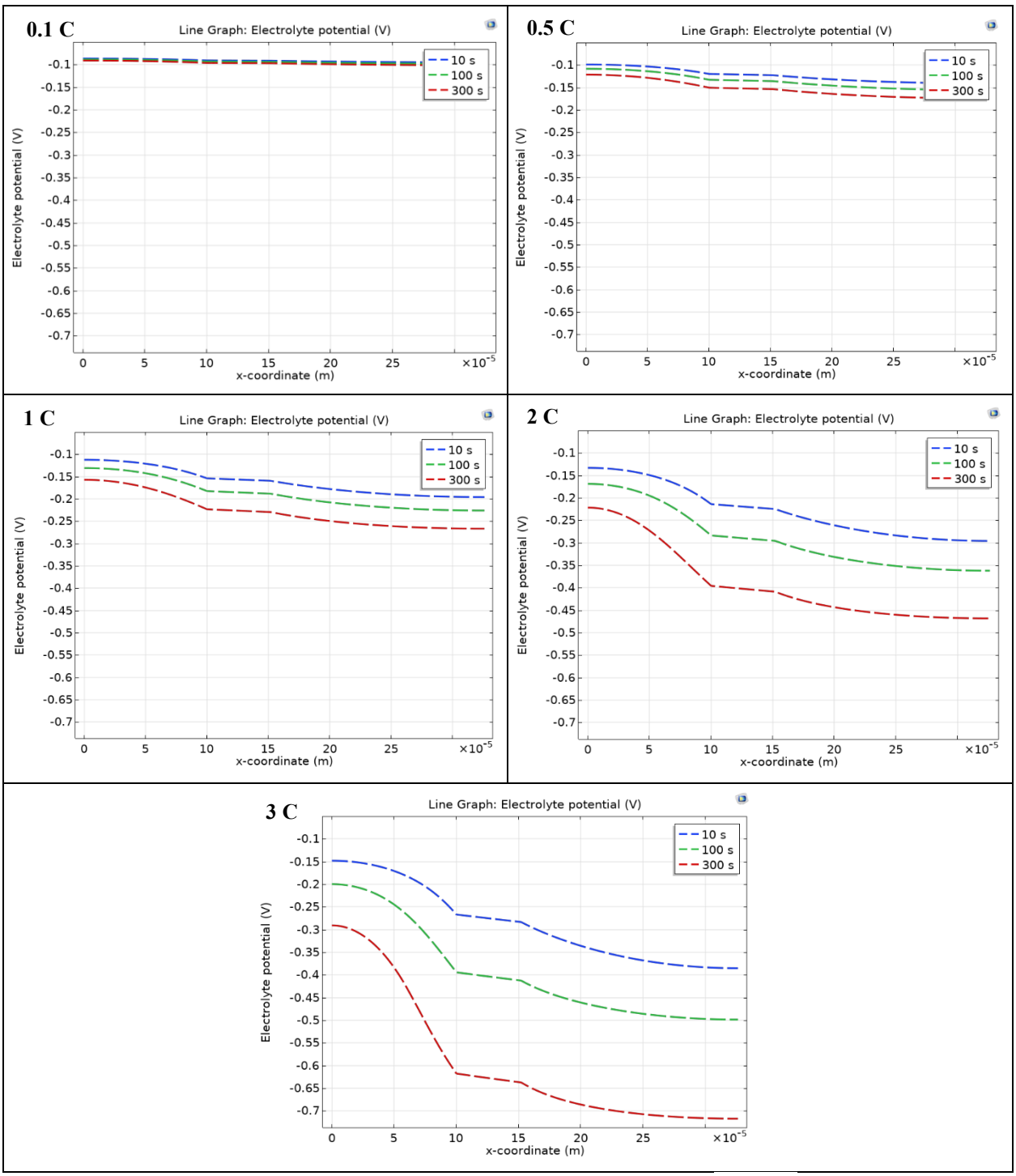

Figure 11. Electrolyte potential distribution across five distinct C-rates.

Table 5. Average electrolyte potential difference of battery components across five distinct C-rates (10–300 s).

C-Rate	Between 10s and 300s, Approximate Average Electrolyte Potential Difference of Negative Electrode [0-10]x10^{-5} m	Between 10s and 300s, Approximate Average Electrolyte Potential Difference of Electrolyte [10-15,2]x10^{-5} m	Between 10s and 300s, Approximate Average Electrolyte Potential Difference of Positive Electrode [15,2-32,6]x10^{-5} m
0.1	-0.087 V _ -0.092 V Difference = 0.005 V	-0.091 V _ -0.096 V Difference = 0.005 V	-0.094 V _ -0.1 V Difference = 0.006 V
0.5	-0.103 V _ -0.128 V Difference = 0.025 V	-0.121 V _ -0.152 V Difference = 0.031 V	-0.136 V _ -0.168 V Difference = 0.032 V
1	-0.12 V _ -0.175 V Difference = 0.055 V	-0.157 V _ -0.227 V Difference = 0.07 V	-0.186 V _ -0.257 V Difference = 0.071 V
2	-0.15 V _ -0.273 V Difference = 0.123 V	-0.22 V _ -0.404 V Difference = 0.184 V	-0.276 V _ -0.455 V Difference = 0.179 V
3	-0.17 V _ -0.385 V Difference = 0.215 V	-0.277 V _ -0.63 V Difference = 0.353 V	-0.358 V _ -0.7 V Difference = 0.342 V

As illustrated in Figure 12 and Table 6, the electric potential of the positive electrode decreases during the initial 300 seconds of the discharge phase across all C-rates. The data further indicates that this rate of decline accelerates as the C-rate increases, resulting in a steeper potential drop.

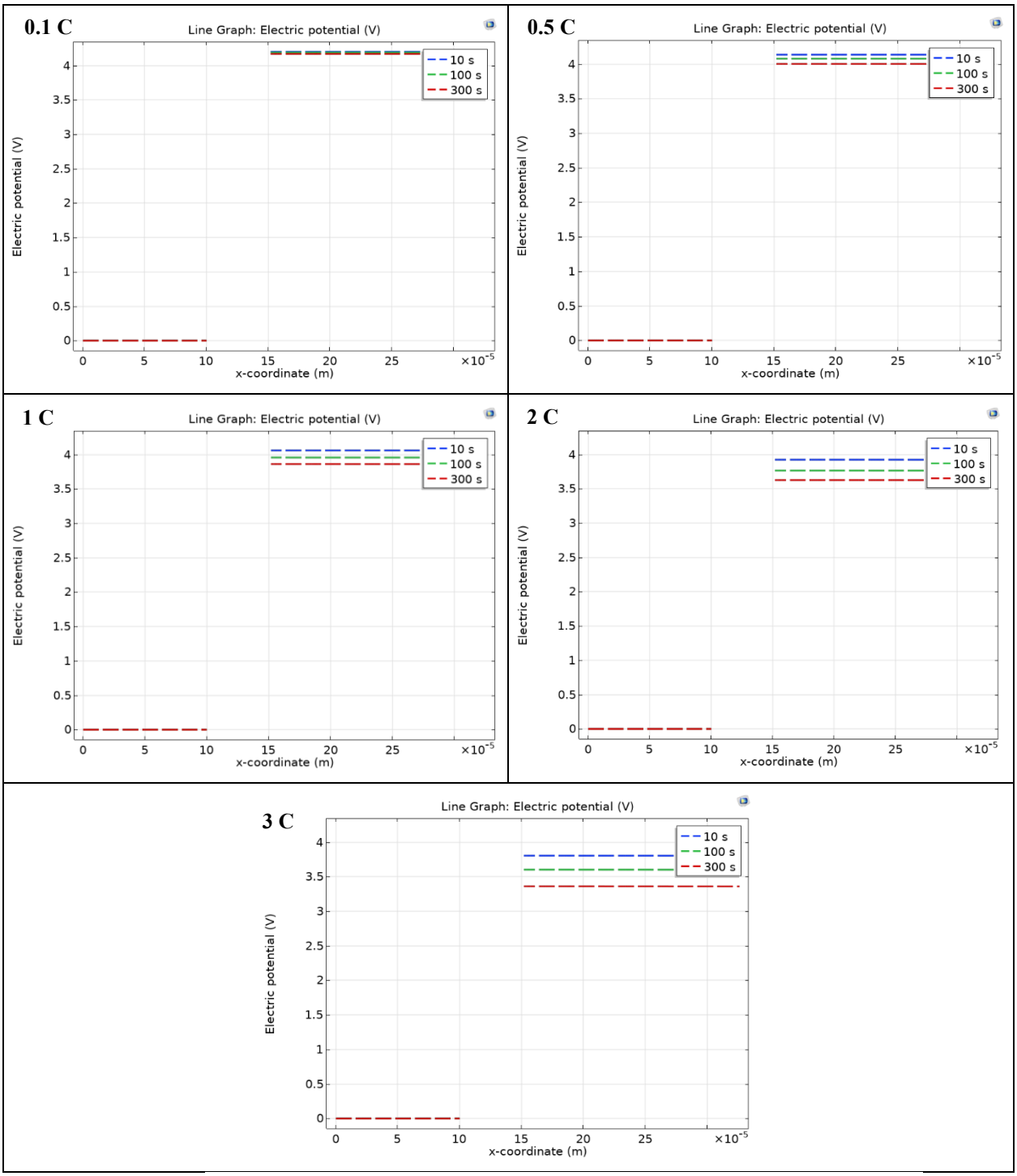

Figure 12. Electrode potential with respect to ground across five distinct C-rates.

Table 6. Positive electrode electric potential difference across five distinct C-rates (10–300 s).

C-Rate	Between 10s and 300s, Approximate Electric Potential Difference of Positive Electrode [15,2-32,6]x10^{-5} m
0.1	4.2 V – 4.17 V Difference = 0.03 V
0.5	4.13 V – 4.0 V Difference = 0.13 V
1	4.05 V – 3.85 V Difference = 0.2 V
2	3.92 V – 3.63 V Difference = 0.29 V
3	3.8 V – 3.36 V Difference = 0.44 V

To analyze the evolution of electrolyte salt concentration, time snapshots of 1200, 1800, 2200, 2400, and 3000 seconds were chosen. For the 1C rate, these times effectively map the full cycle: mid-to-late discharge, the relaxation phase, and the subsequent charging process. However, due to time scaling, these points represent the discharge phase for 0.1C and 0.5C rates, whereas for the 2C rate, the period from 1800 s onward falls within the charge phase. The average salt concentration values were derived from the vertical axis at approximate average horizontal coordinates. Figure 13 and Table 7 indicate that the variation in salt concentration widens as the C-rate rises.

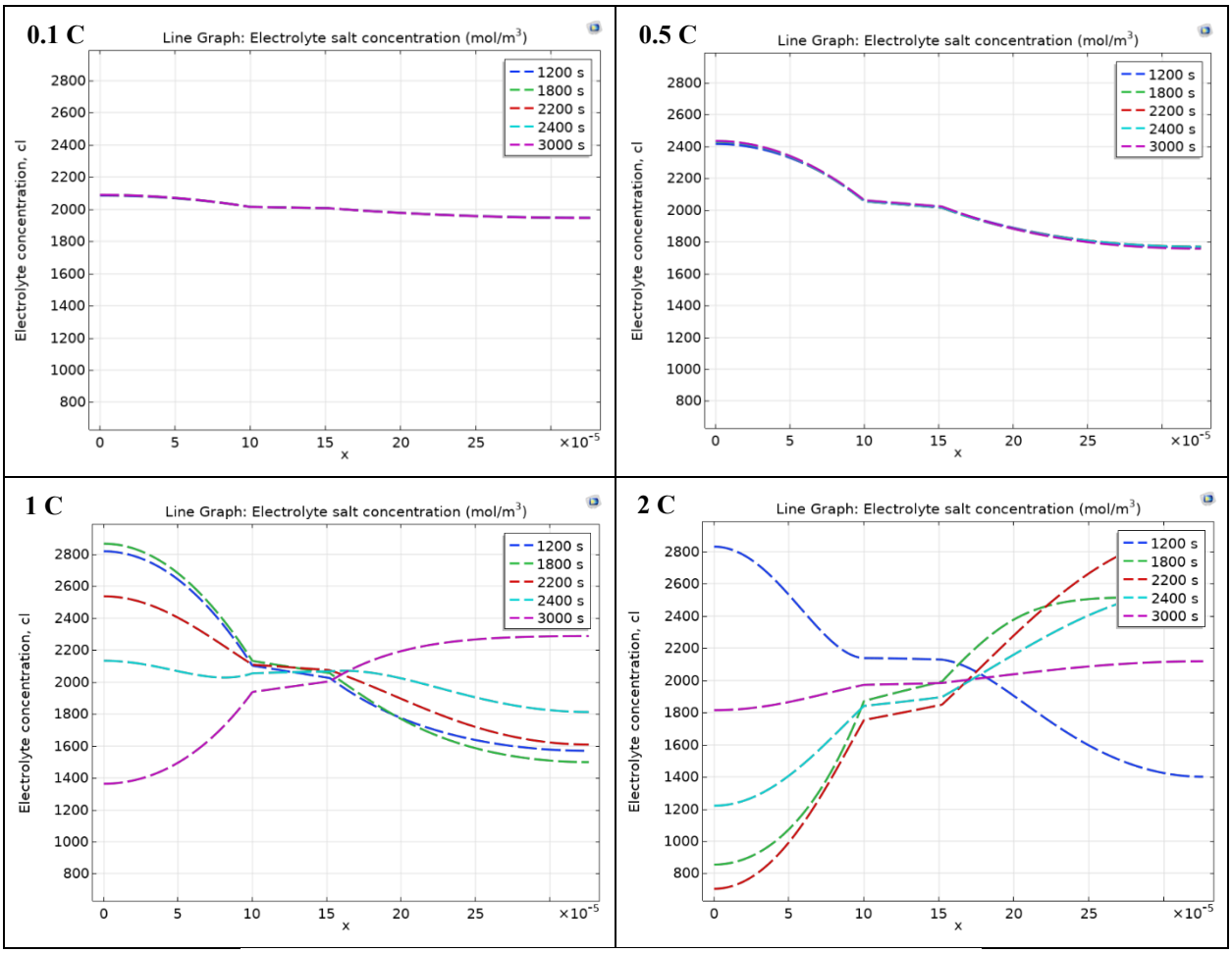

Figure 13. Electrolyte salt concentration at various C-rates.

Table 7. Average electrolyte salt concentration ranges within battery components at various C-rates.

C-Rate	Average Electrolyte Salt Concentration Range of Negative Electrode [0-10]x10^{-5} m	Average Electrolyte Salt Concentration Range of Electrolyte [10-15,2]x10^{-5} m	Average Electrolyte Salt Concentration Range of Positive Electrode [15,2-32,6]x10^{-5} m
0.1	2070 mol/m^3 - 2067 mol/m^3 Difference = 3 mol/m^3	2010 mol/m^3 - 2010 mol/m^3 Difference = 0 mol/m^3	1962 mol/m^3 - 1960 mol/m^3 Difference = 2 mol/m^3
0.5	2340 mol/m^3 - 2330 mol/m^3 Difference = 10 mol/m^3	2040 mol/m^3 - 2035 mol/m^3 Difference = 5 mol/m^3	1820 mol/m^3 – 1810 mol/m^3 Difference = 10 mol/m^3
1	2700 mol/m^3 - 1500 mol/m^3 Difference = 1200 mol/m^3	2080 mol/m^3 - 1970 mol/m^3 Difference = 110 mol/m^3	2250 mol/m^3 - 1600 mol/m^3 Difference = 650 mol/m^3
2	2530 mol/m^3 - 1000 mol/m^3 Difference = 1530 mol/m^3	2130 mol/m^3 - 1800 mol/m^3 Difference = 330 mol/m^3	2650 mol/m^3 - 1650 mol/m^3 Difference = 1000 mol/m^3

Figure 14 illustrates that the gradient in solid lithium concentration between the particle surface and center intensifies as the C-rate increases. Temporally, the negative electrode exhibits a consistent depletion of solid lithium at both the surface and center, whereas the positive electrode shows a corresponding accumulation. As supported by Figure 14 and Table 8, the disparity in average lithium concentration between the center and surface of the electrode particles widens progressively over time and scales proportionally with the C-rate.

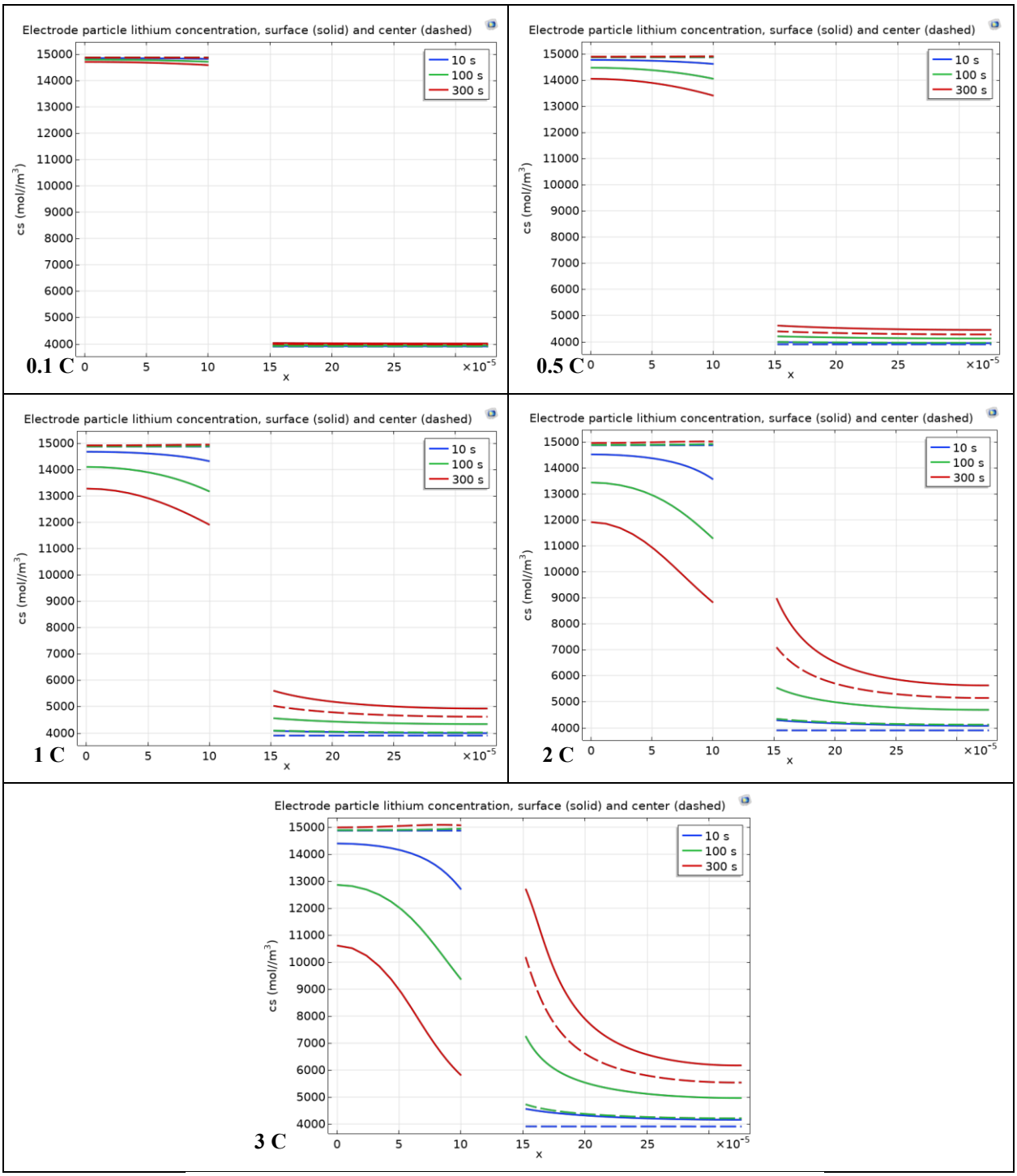

Figure 14. Solid lithium concentration at five distinct C-rates.

Table 8. Center-to-surface lithium concentration differences in negative and positive electrode particles across five distinct C-rates.

C-Rate	Time	Between Center and Surface, Approximate Average Electrode Particle Lithium Concentration Difference of Negative Electrode [0-10]x10^{-5} m	Between Surface and Center Approximate Average Electrode Particle Lithium Concentration Difference of Positive Electrode [15,2-32,6]x10^{-5} m
0.1	10 s.	14870 mol/m^3 - 14840 mol/m^3 Difference = 30 mol/m^3	3910 mol/m^3 - 3900 mol/m^3 Difference = 10 mol/m^3
	100 s.	14870 mol/m^3 - 14775 mol/m^3 Difference = 95 mol/m^3	3950 mol/m^3 - 3910 mol/m^3 Difference = 40 mol/m^3
	300 s.	14870 mol/m^3 - 14680 mol/m^3 Difference = 190 mol/m^3	4020 mol/m^3 - 3980 mol/m^3 Difference = 40 mol/m^3
0.5	10 s.	14870 mol/m^3 - 14740 mol/m^3 Difference = 130 mol/m^3	3950 mol/m^3 - 3900 mol/m^3 Difference = 50 mol/m^3
	100 s.	14870 mol/m^3 - 14380 mol/m^3 Difference = 490 mol/m^3	4150 mol/m^3 - 3950 mol/m^3 Difference = 200 mol/m^3
	300 s.	14900 mol/m^3 - 13900 mol/m^3 Difference = 1000 mol/m^3	4500 mol/m^3 - 4300 mol/m^3 Difference = 200 mol/m^3
1	10 s.	14870 mol/m^3 - 14600 mol/m^3 Difference = 270 mol/m^3	4000 mol/m^3 - 3900 mol/m^3 Difference = 10 mol/m^3
	100 s.	14880 mol/m^3 - 13900 mol/m^3 Difference = 980 mol/m^3	4365 mol/m^3 - 4030 mol/m^3 Difference = 335 mol/m^3
	300 s.	14920 mol/m^3 - 12900 mol/m^3 Difference = 2020 mol/m^3	5000 mol/m^3 - 4670 mol/m^3 Difference = 330 mol/m^3
2	10 s.	14870 mol/m^3 - 14370 mol/m^3 Difference = 500 mol/m^3	4105 mol/m^3 - 3900 mol/m^3 Difference = 205 mol/m^3
	100 s.	14890 mol/m^3 - 12950 mol/m^3 Difference = 1940 mol/m^3	4778 mol/m^3 - 4150 mol/m^3 Difference = 628 mol/m^3

	300 s.	14980 mol/m^3 - 10930 mol/m^3 Difference = 4050 mol/m^3	5860 mol/m^3 - 5300 mol/m^3 Difference = 560 mol/m^3
3	10 s.	14870 mol/m^3 - 14155 mol/m^3 Difference = 715 mol/m^3	4200 mol/m^3 - 3900 mol/m^3 Difference = 300 mol/m^3
	100 s.	14897 mol/m^3 – 12016 mol/m^3 Difference = 2881 mol/m^3	5110 mol/m^3 - 4250 mol/m^3 Difference = 860 mol/m^3
	300 s.	15040 mol/m^3 - 8967 mol/m^3 Difference = 6073 mol/m^3	6560 mol/m^3 - 5790 mol/m^3 Difference = 770 mol/m^3

Figure 15 compares the discharge curves across five distinct C-rates (0.1C, 0.5C, 1C, 2C, and 3C).

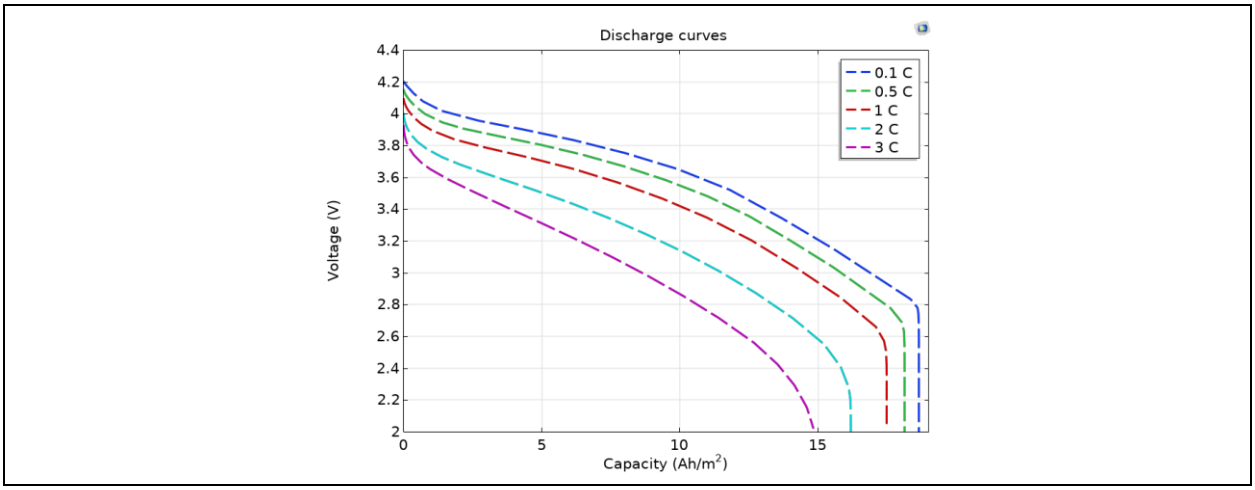

Figure 15. Comparison of discharge profiles across five distinct C-rates.

4.2 Electrolyte, Electrode Material Effect on 1D LIB

Batteries are fundamentally composed of electrodes and electrolytes. Given that battery operation relies on electrochemical processes, the intrinsic properties and chemical behavior of these materials are fundamental.

This research [91] investigates the impact of six distinct electrolyte materials using a 1D isothermal LIB model within COMSOL Multiphysics. The electrolytes were categorized into two cohorts:

- Group 1: Two batteries utilizing polymer electrolytes with varying solvents.
- Group 2: Four batteries employing liquid electrolytes with differing solvents.

The specific materials and their properties, sourced from the COMSOL Multiphysics Battery Design Module material library, are outlined below:

1. Polymeric Electrolyte (1:2 EC:DMC): Composed of $LiPF_6$ salt dissolved in a 1:2 volume ratio of EC:DMC solvent within a PVDF-HFP polymer matrix. Key properties include a diffusion coefficient of 7.5×10^{-11} m^2/s, a transport number of 0.363, and a salt concentration of 1000 mol/m^3.

2. Polymeric Electrolyte (2:1 EC:DMC): Utilizes $LiPF_6$ salt in a 2:1 EC:DMC solvent mixture. It retains the same PVDF-HFP polymer structure and identical material properties as the first electrolyte.

3. Liquid Electrolyte (1:1 EC:DEC): A solution based on $LiPF_6$ dissolved in a 1:1 EC:DEC solvent system, with a salt concentration of 1000 mol/m^3.

4. Liquid Electrolyte (1:1 EC:DMC): Consists of $LiPF_6$ dissolved in a 1:1 EC:DMC mixture.

5. Liquid Electrolyte (3:7 EC:EMC): Features $LiPF_6$ in a 3:7 EC:EMC solvent system with a salt concentration of 1200 mol/m^3.

6. Liquid Electrolyte (PC:EC:EMC): Composed of $LiPF_6$ in a solvent mixture of 0.1 PC : 0.27 EC : 0.63 EMC, also maintaining a salt concentration of 1200 mol/m^3.

Utilizing these distinct electrolyte formulations allows for a comparative analysis of ion transport and electrochemical performance within the LIB simulations. Specific time snapshots 1200, 1800, 2200, 2400, and 3000 s were selected for the electrolyte salt concentration graph to represent critical phases of a 1C charge-discharge cycle:

- 1200 s (Mid-Discharge): Captures the concentration profile during the active discharge phase, providing data before the cycle nears completion.
- 1800 s (Late Discharge): Represents the final stages of discharge, highlighting concentration gradients as the battery approaches full depletion.
- 2200 s (Rest Period): occurs during the 300-second pause following discharge, allowing for the observation of post-discharge electrolyte relaxation.
- 2400 s (Onset of Charge): Marks the beginning of the charging phase, establishing a baseline for concentration shifts as energy input begins.

- 3000 s (Late Charge): Reflects the profile near the end of the charging process, demonstrating how lithium ions redistribute as the battery nears capacity.

Figure 16 illustrates the spatial distribution of electrolyte salt concentration across the battery cross section for six different electrolytes at a 1 C-rate, captured at five distinct time intervals. The horizontal axis represents the battery dimension (m), while the vertical axis displays the salt concentration (mol/m^3).

An analysis of Figure 16 and Table 9 reveals distinct trends among the groups:

- Cases A and B: The polymer electrolytes exhibit nearly identical concentration profiles across all battery domains (negative electrode, electrolyte, and positive electrode).
- Cases D, E, and F: The liquid electrolytes demonstrate similar concentration magnitudes.

Furthermore, the polymer electrolytes (Cases A and B) and Case C ($LiPF_6$ in 1:1 EC:DEC) maintain a higher average salt concentration compared to the other formulations. To quantify the concentration gradients, the difference between the maximum and minimum concentrations at the midpoint of the battery components was calculated and defined as the average electrolyte salt concentration range.

A) $LiPF_6$ salt in 1:2 EC:DMC (by volume) solvent and PVDF-HFP (Polymer, LIB)	B) $LiPF_6$ salt in 2:1 EC:DMC (by volume) solvent and PVDF-HFP (Polymer, LIB)
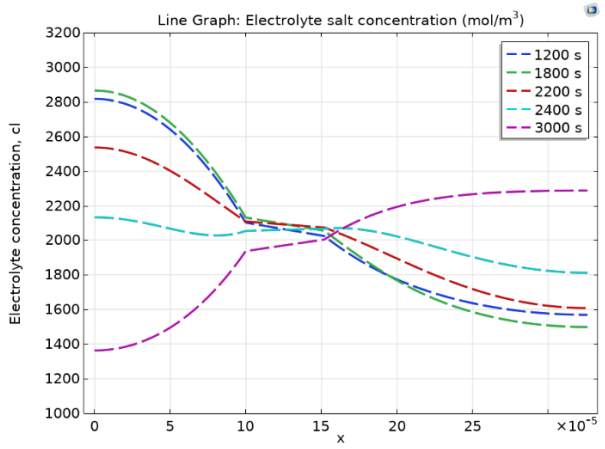	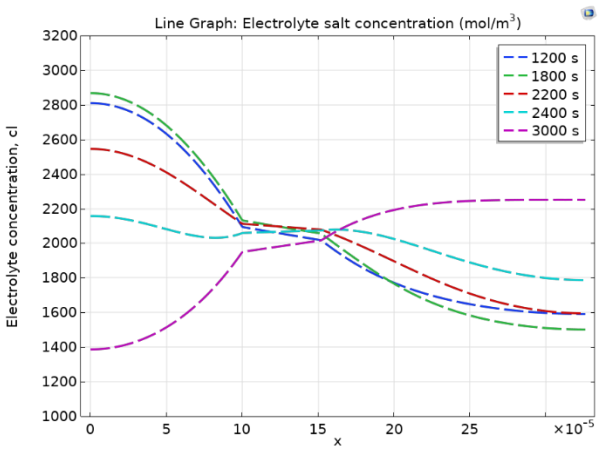
C) $LiPF_6$ in 1:1 EC:DEC (Liquid, LIB)	**D) $LiPF_6$ in 1:1 EC:DMC (Liquid, LIB)**
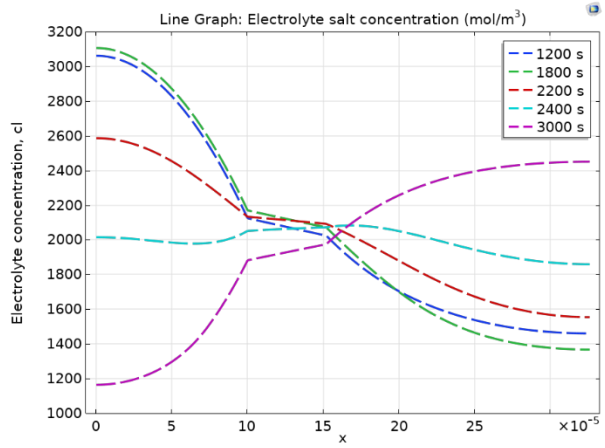	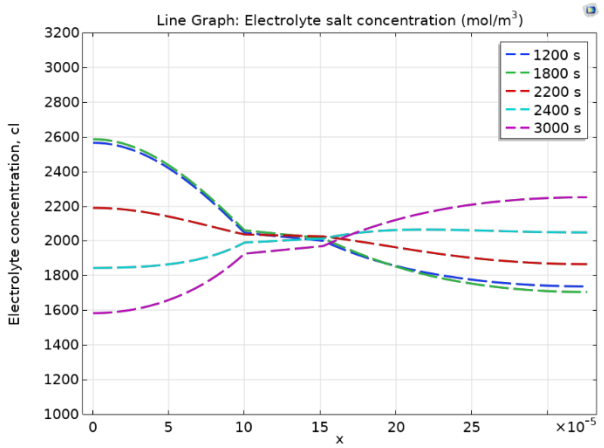
E) $LiPF_6$ in 3:7 EC:EMC (Liquid, LIB)	**F) $LiPF_6$ in 0.1PC:0.27EC:0.63EMC (Liquid, LIB)**
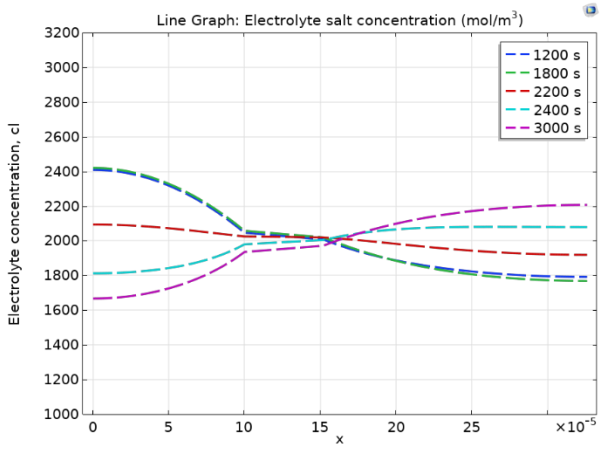	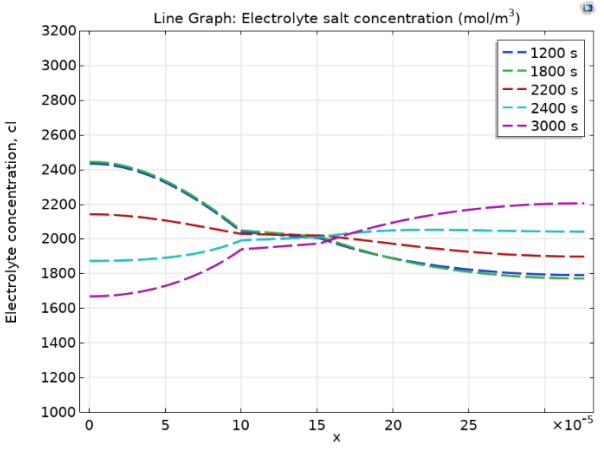

Figure 16. Comparative analysis of salt concentration across different LIBs electrolytes at selected time steps.

Table 9. Ranges of average electrolyte salt concentrations across battery components for LIBs utilizing various electrolyte materials.

Electrolyte Material Types	**Average Electrolyte Salt Concentration Range of Negative Electrode [0-10]x10^{-5} m**	**Average Electrolyte Salt Concentration Range of Electrolyte [10-15,2]x10^{-5} m**	**Average Electrolyte Salt Concentration Range of Positive Electrode [15,2-32,6]x10^{-5} m**
$LiPF_6$ salt in 1:2 EC:DMC (by volume) solvent and PVDF-HFP (Polymer, LIB)	2680 mol/m^3 – 1495 mol/m^3 Difference = 1185 mol/m^3	2095 mol/m^3 - 1970 mol/m^3 Difference = 125 mol/m^3	2265 mol/m^3 - 1586 mol/m^3 Difference = 679 mol/m^3
$LiPF_6$ salt in 2:1 EC:DMC (by volume) solvent and PVDF-HFP (Polymer, LIB)	2680 mol/m^3 - 1515 mol/m^3 Difference = 1165 mol/m^3	2095 mol/m^3 - 1980 mol/m^3 Difference = 115 mol/m^3	2245 mol/m^3 – 1583 mol/m^3 Difference = 662 mol/m^3
$LiPF_6$ in 1:1 EC:DEC (Liquid, LIB)	2870 mol/m^3 - 1297 mol/m^3 Difference = 1573 mol/m^3	2122 mol/m^3 - 1927 mol/m^3 Difference = 195 mol/m^3	2395 mol/m^3 - 1465 mol/m^3 Difference = 930 mol/m^3
$LiPF_6$ in 1:1 EC:DMC (Liquid, LIB)	2436 mol/m^3 - 1659 mol/m^3 Difference = 777 mol/m^3	2037 mol/m^3 - 1947 mol/m^3 Difference = 90 mol/m^3	2208 mol/m^3 - 1754 mol/m^3 Difference = 454 mol/m^3
$LiPF_6$ in 3:7 EC:EMC (Liquid, LIB)	2330 mol/m^3 - 1725 mol/m^3 Difference = 605 mol/m^3	2040 mol/m^3 - 1953 mol/m^3 Difference = 87 mol/m^3	2171 mol/m^3 - 1807 mol/m^3 Difference = 364 mol/m^3
$LiPF_6$ in 0.1PC:0.27EC:0.63EMC (Liquid, LIB)	2333 mol/m^3 - 1729 mol/m^3 Difference = 604 mol/m^3	2031 mol/m^3 - 1955 mol/m^3 Difference = 76 mol/m^3	2167 mol/m^3 - 1810 mol/m^3 Difference = 357 mol/m^3

Figure 17 illustrates the discharge profiles of LIBs utilizing varying electrolytes across different C-rates. In these graphs, voltage (V) is plotted against capacity (Ah/m^2). The left panel depicts the performance of two batteries with polymer electrolytes, while the right panel displays four batteries utilizing liquid electrolytes. A comparison of the discharge curves reveals that the liquid electrolyte batteries exhibit higher voltage levels, particularly at elevated C-rates. For a detailed quantitative analysis, this data is summarized in Table 10.

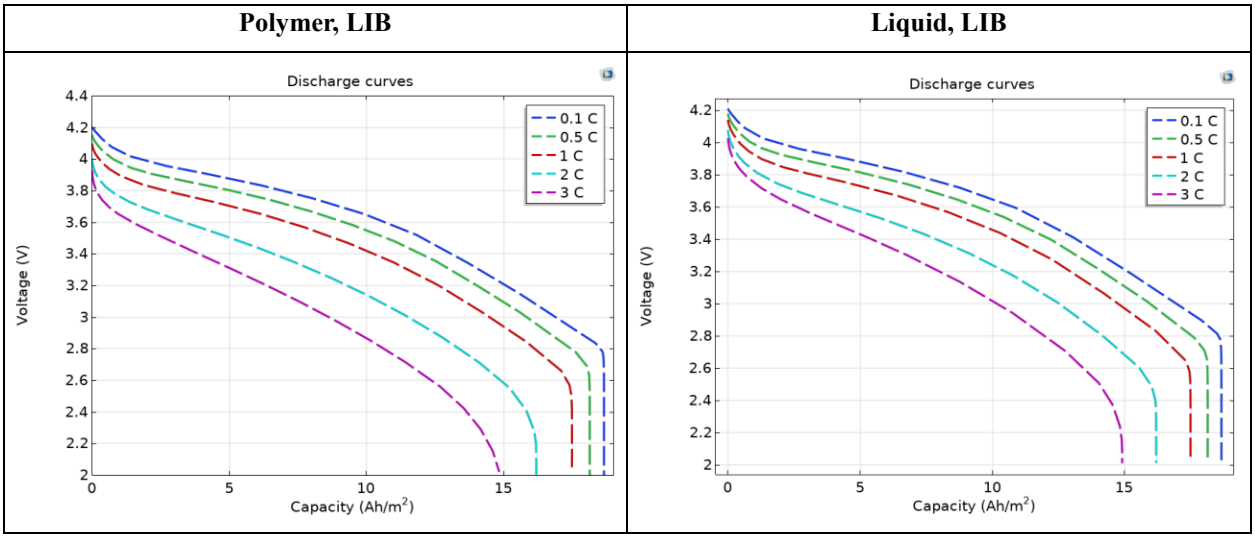

Figure 17. Comparative analysis of discharge curves for LIBs utilizing various electrolyte materials across five C-rates.

Table 10. Voltage-capacity profiles of LIBs utilizing different electrolyte materials evaluated at five distinct C-rates.

Electrolyte Material Type	C-rate	Capacity (Ah/m^2) 0	5	10	15
Polymer, LIB	**0.1**	4.2 V	3.875 V	3.65 V	3.2 V
	0.5	4.155 V	3.8 V	3.55 V	3.09 V
	1	4.099 V	3.7 V	3.419 V	2.93 V
	2	4 V	3.5 V	3.14 V	2.58 V
	3	3.93 V	3.31 V	2.86 V	-
Liquid, LIB	**0.1**	4.21 V	3.87 V	3.65 V	3.2 V
	0.5	4.17 V	3.82 V	3.57 V	3.1 V
	1	4.14 V	3.74 V	3.47 V	2.98 V
	2	4.08 V	3.6 V	3.28 V	2.7 V
	3	4.02 V	3.47 V	3.08 V	-

Among common cathode materials, LCO is distinguished by its superior specific energy density. Electrochemical behaviors differ significantly across materials; for instance, LMO batteries function within a range of 3.0–4.2 V (3.7 V nominal), whereas LFP cells operate between 2.5–3.65 V with a nominal voltage of 3.2 V. Although LFP exhibits lower specific capacity and operating voltage, it is considered one of the most dependable technologies due to its exceptional voltage plateau stability, high-current performance, and slow reaction rate with the electrolyte. In contrast, NCA is characterized by high specific capacity and elevated operating voltage [104], offering three main benefits: high energy density, outstanding power density, and superior cycle durability. Properties for these five positive electrode materials, sourced from the COMSOL Multiphysics Battery Design Module material library, are detailed in the Appendix.

Figure 18 and Table 11 illustrate the average electrode state of charge (AESOC) for five LIBs with distinct positive electrode materials, subjected to identical load cycling at a 1C rate. The negative electrodes (porous electrode 1) exhibited consistent AESOC values across all battery types examined. However, the positive electrodes (porous electrode 2) demonstrated significant

variation during the discharge period. LFP showed the largest AESOC increase at 0.33, followed by $LiNiO_2$ at 0.31, LMO at 0.30, NCA at 0.14, and LCO with the smallest rise at 0.121. When the cathode materials are ranked by increasing reference concentration and density LFP, LMO, $LiNiO_2$, NCA, and LCO the order closely aligns with the observed trend in AESOC elevation (from highest to lowest). These results confirm the outstanding performance of LFP under high-rate conditions, as previously noted in [104].

Variations in the AESOC offer critical insights into the electrochemical balance, operational efficiency, and durability of LIBs throughout charge-discharge cycles. AESOC behavior is heavily influenced by the reference concentration and density of the cathode materials, which dictate both Li-ion storage capacity and mass transport dynamics. Materials with lower reference concentrations and densities, such as LFP and LMO, experience more pronounced AESOC shifts during discharge. This occurs because their lower initial volumetric or gravimetric lithium content results in a larger fractional depletion of SOC under load. Conversely, high density materials like LCO and NCA possess larger total lithium reserves, resulting in more moderate relative SOC changes under identical conditions. These trends highlight a fundamental trade-off in battery design: materials exhibiting high AESOC fluctuations (e.g., LFP) generally offer superior safety, structural stability, and cycle life, albeit at the expense of energy density. In contrast, materials with stable AESOC profiles (e.g., LCO, NCA) maximize energy output but are more susceptible to structural stress and degradation, potentially shortening the battery's lifespan.

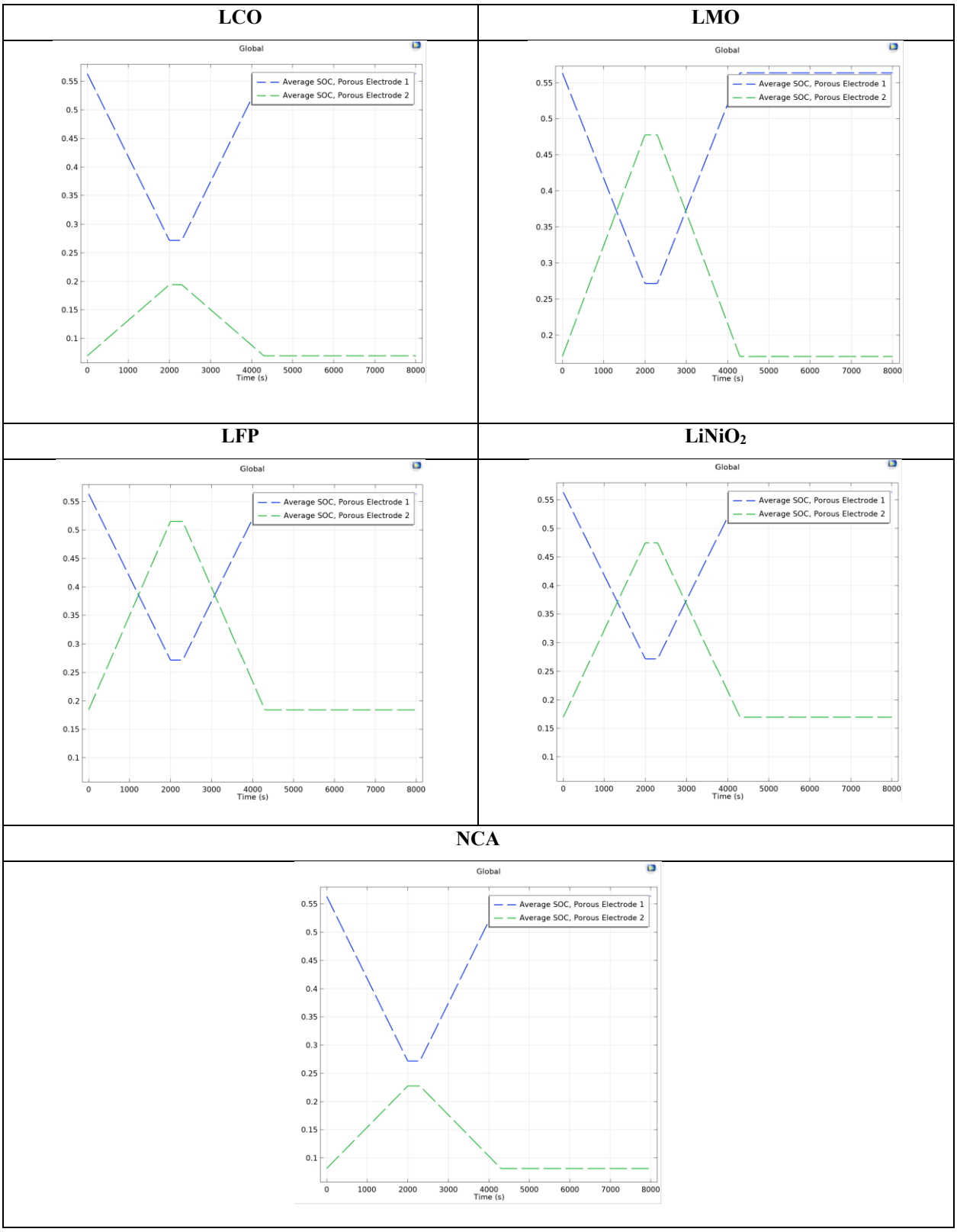

Figure 18. Average SOC profiles of porous electrodes in LIBs with different cathode compositions during charging and discharging at 1 C-rate.

Table 11. Average SOC values of porous electrodes for LIBs having various cathode materials at chosen times of 1 C-rate.

Positive Electrode Material Type		Time (s)		
		0	2000	4000
LCO, $LiCoO_2$	Negative Electrode	0.56	0.27	0.519
	Positive Electrode	0.069	0.19	0.087
LMO, $LiMn_2O_4$	Negative Electrode	0.56	0.27	0.519
	Positive Electrode	0.17	0.47	0.21
LFP, $LiFePO_4$	Negative Electrode	0.56	0.27	0.519
	Positive Electrode	0.18	0.51	0.23
$LiNiO_2$	Negative Electrode	0.56	0.27	0.519
	Positive Electrode	0.16	0.47	0.21
NCA, $LiNi_{0.8}Co_{0.15}Al_{0.05}O_2$	Negative Electrode	0.56	0.27	0.519
	Positive Electrode	0.08	0.22	0.1

Figure 19 illustrates the lithium concentration values at the surface and center of positive and negative electrode particles for five different LIBs at a 1 C-rate. Complementary numerical data is provided in Table 12. An analysis of the positive electrode surface data reveals that LFP exhibits the most significant variation in particle lithium concentration between the 1200 and 1800-second time points. Conversely, $LiNiO_2$ demonstrates the smallest concentration difference over this same interval. This trend LFP showing the highest variation and $LiNiO_2$ the lowest is consistent for the lithium concentrations observed at the particle center as well. These concentration gradients serve as a critical indicator of solid-phase diffusion kinetics and interfacial mechanical stress, highlighting the materials' rate capability and long-term structural stability.

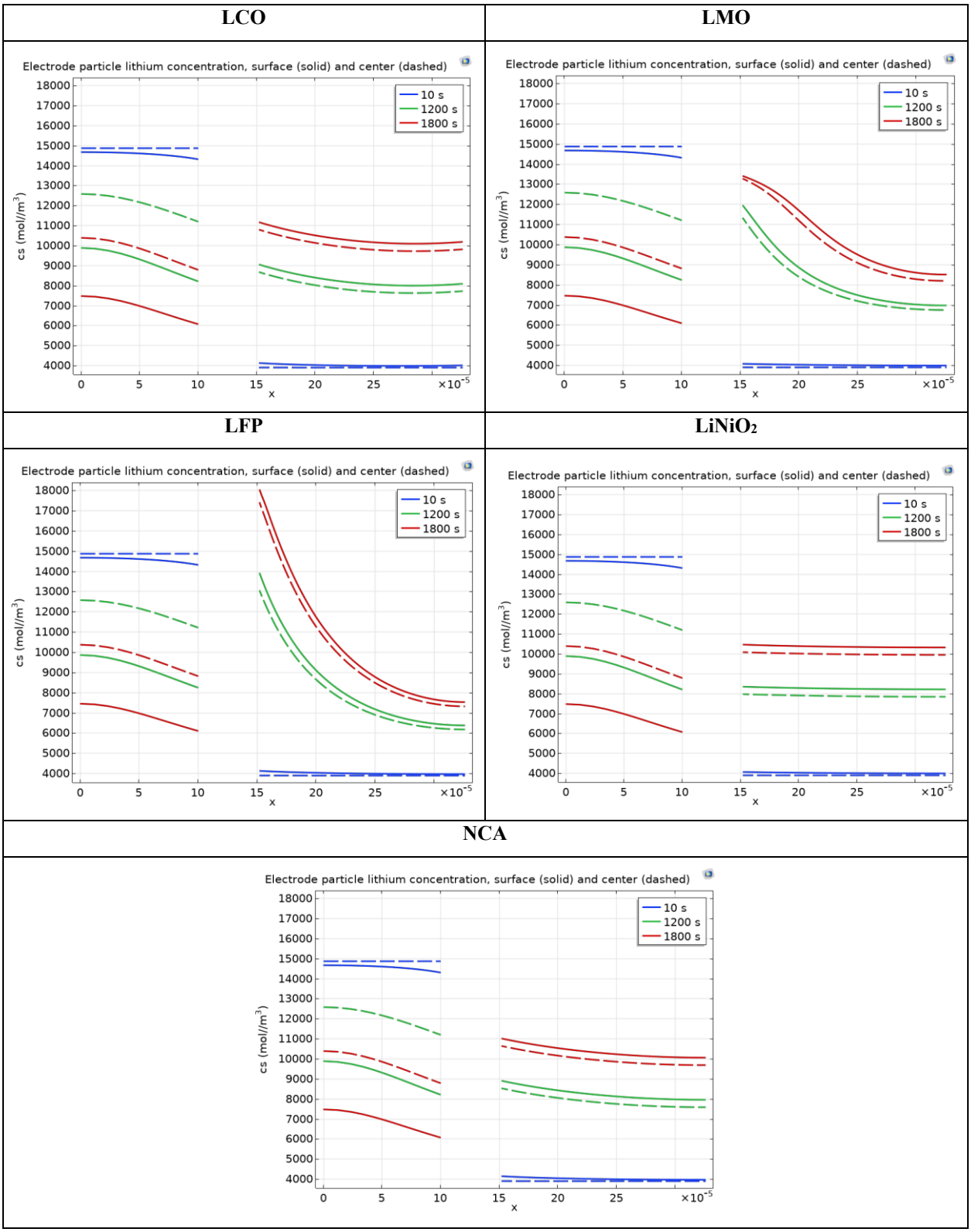

Figure 19. Profiles of solid-phase lithium concentration at the electrode surface and center for different cathode materials during a 1 C-rate discharge.

Table 12. Comparison of lithium concentration differences between two surface points of the positive electrode for distinct cathode materials during the discharge phase.

Positive Electrode Material Type	**Difference of Electrode Particle Lithium Concentration of the Positive Electrode Surface Two Chosen Point [(16-30)x10^{-5} m] According to Time (s)**		
	10	**1200**	**1800**
LCO, $LiCoO_2$	4105 mol/m^3-3991 mol/m^3 = 114 mol/m^3	8918 mol/m^3-8011 mol/m^3 = 907 mol/m^3	11034 mol/m^3 -10108 mol/m^3 = 926 mol/m^3
LMO, $LiMn_2O_4$	4069 mol/m^3-3992 mol/m^3 = 77 mol/m^3	11341 mol/m^3-7023 mol/m^3 = 4318 mol/m^3	13227 mol/m^3 -8604 mol/m^3 = 4623 mol/m^3
LFP, $LiFePO_4$	4110 mol/m^3-3975 mol/m^3 = 135 mol/m^3	12742 mol/m^3 -6465 mol/m^3 = 6277 mol/m^3	16787 mol/m^3 -7665 mol/m^3 = 9122 mol/m^3
$LiNiO_2$	4059 mol/m^3-3997 mol/m^3 = 62 mol/m^3	8337 mol/m^3 -8222 mol/m^3 = 115 mol/m^3	10449 mol/m^3 -10326 mol/m^3 = 123 mol/m^3
NCA, $LiNi_{0.8}Co_{0.15}Al_{0.05}O_2$	4122 mol/m^3-3971 mol/m^3 = 151 mol/m^3	8810 mol/m^3 -7979 mol/m^3 = 831 mol/m^3	10920 mol/m^3 -10081 mol/m^3 = 839 mol/m^3

Figure 20 and Table 13 illustrate the discharge characteristics of the varying cathode materials. At the onset of the discharge period, $LiNiO_2$ exhibits the highest initial potential, followed by LCO, NCA, and LMO, with LFP showing the lowest potential. However, this hierarchy shifts significantly toward the end of the discharge cycle. In the final stages, LCO retains the maximum potential, followed by NCA and LMO. Notably, $LiNiO_2$ drops to the second-lowest position, while LFP remains at the minimum voltage value.

Quantitative analysis reveals that $LiNiO_2$ experiences the largest voltage decay, with a difference of 3.58 V between 0 and 15 Ah/m^2. While this steep drop suggests high energy availability, it implies reduced voltage stability, making it suitable for energy-intensive applications where stability is secondary. In contrast, LFP demonstrates the most stable profile, with a minimal potential difference of just 0.9 V over the same range. Although this smaller voltage window indicates lower energy density, the superior stability of LFP supports applications requiring safety

and extended cycle life. As noted in [104], LFP is defined by its lower voltage and slow electrolyte reactivity, whereas NCA is distinguished by high specific capacity and elevated operating voltage.

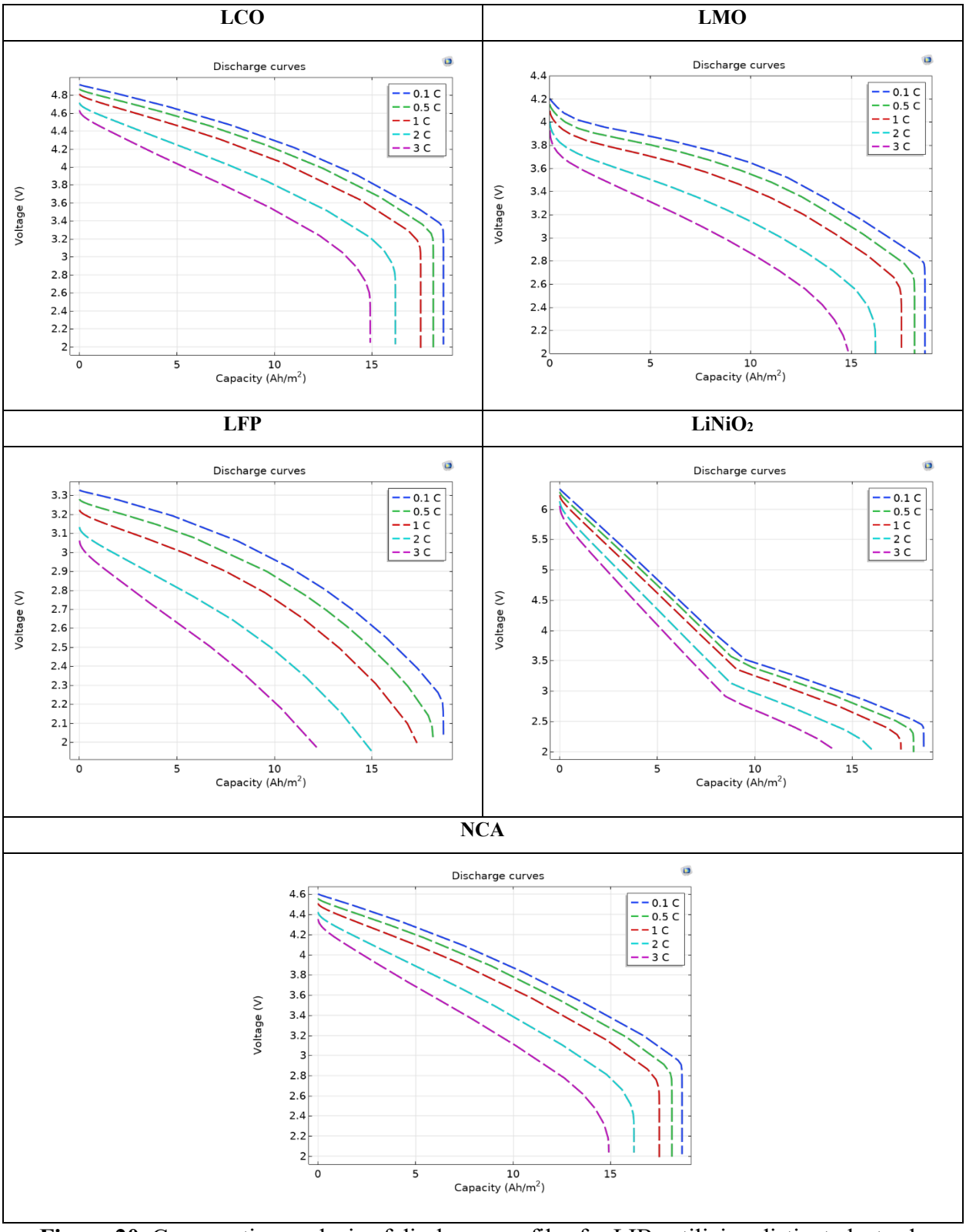

Figure 20. Comparative analysis of discharge profiles for LIBs utilizing distinct electrode materials across five C-rates.

Table 13. Comparative analysis of voltage-capacity profiles for LIBs utilizing distinct electrode materials across five C-rates.

Positive Electrode Material Type	**Capacity (Ah/m^2)**				
	C-rate	**0**	**5**	**10**	**15**
LCO, LiC_oO_2	**0.1**	4.91 V	4.64 V	4.29 V	3.81 V
	0.5	4.87 V	4.56 V	4.2 V	3.7 V
	1	4.81 V	4.46 V	4.07 V	3.55 V
	2	4.71 V	4.24 V	3.79 V	3.19 V
	3	4.63 V	4.03 V	3.51 V	-
LMO, $LiMn_2O_4$	**0.1**	4.2 V	3.875 V	3.65 V	3.2 V
	0.5	4.155 V	3.8 V	3.55 V	3.09 V
	1	4.099 V	3.7 V	3.419 V	2.93 V
	2	4 V	3.5 V	3.14 V	2.58 V
	3	3.93 V	3.31 V	2.86 V	-
LFP, $LiFePO_4$	**0.1**	3.32 V	3.18 V	2.96 V	2.61 V
	0.5	3.28 V	3.1 V	2.87 V	2.49 V
	1	3.22 V	3.01 V	2.75 V	2.32 V
	2	3.13 V	2.81 V	2.48 V	-
	3	3.06 V	2.62 V	2.2 V	-
$LiNiO_2$	**0.1**	6.33 V	4.83 V	3.46 V	2.92 V
	0.5	6.28 V	4.74 V	3.37 V	2.79 V
	1	6.22 V	4.61 V	3.24 V	2.64 V
	2	6.13 V	4.34 V	2.96 V	2.28 V
	3	6.05 V	4.08 V	2.68 V	-
NCA, $LiNi_{0.8}Co_{0.15}Al_{0.05}O_2$	**0.1**	4.6 V	4.27 V	3.87 V	3.37 V
	0.5	4.56 V	4.19 V	3.77 V	3.26 V
	1	4.5 V	4.09 V	3.65 V	3.12 V
	2	4.42 V	3.88 V	3.38 V	2.76 V

	3	4.35 V	3.68 V	3.11	-

4.3 Nanofluid Coolant Effect on 3D BTMS

The coolants tested included conventional fluids (air and water) as well as nanofluids containing Al_2O_3 (2%, 3%, and 5% volume fractions) dispersed in either water or an EGW base and CuO (5% volume fraction) with the same bases.

Figure 21 clearly highlights the critical impact of coolant selection. While air cooling proved inadequate, leading to significant temperature spikes, liquid cooling provided vastly superior temperature control. The data suggests that cooling performance relies heavily on both the nanoparticle concentration and the thermophysical characteristics of the base fluid. Ultimately, water-based nanofluids achieved the lowest temperature rise, attributing their success to the synergistic effect of water's superior properties and the added thermal conductivity of the nanoparticles.

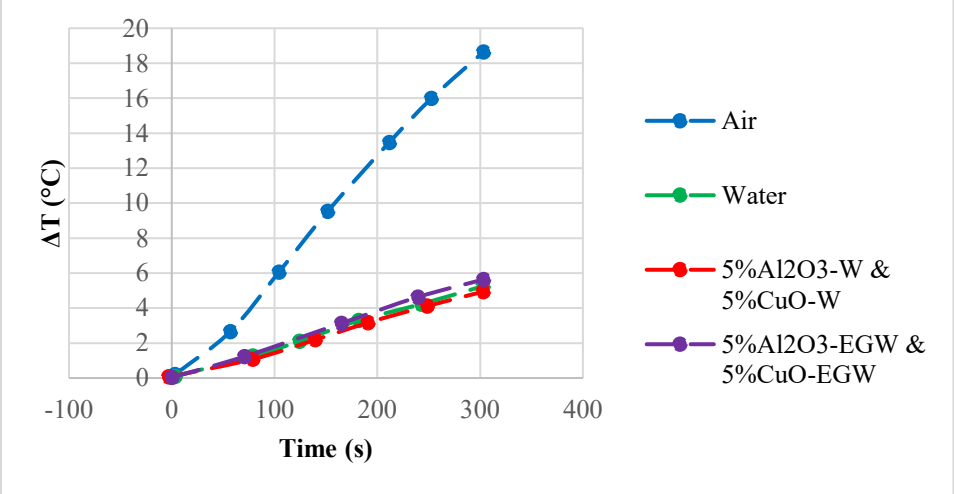

Figure 21. Time-dependent temperature variations for different cooling fluids.

Figure 22 illustrates three key findings regarding thermal management: first, air cooling is inadequate for maintaining thermal stability; second, water-based cooling systems outperform their EGW-based counterparts; and third, the suspension each of nanoparticles (Al_2O_3 and CuO) in either base fluid significantly enhances heat dissipation, resulting in lower battery surface temperatures compared to the base fluids alone. (For each cooling strategy in Figures 22, 23, 25,

and 28, localized (narrowed) color scales were utilized in the visualizations to clearly distinguish the local temperature gradients and the location of hot spots on the battery surface separately. This approach is essential for visualizing the specific thermal distribution details within each model. If a unified scale were used, the entire battery surface would appear red for the air-cooling case, while it would appear entirely blue for the water-based fluid cases.)

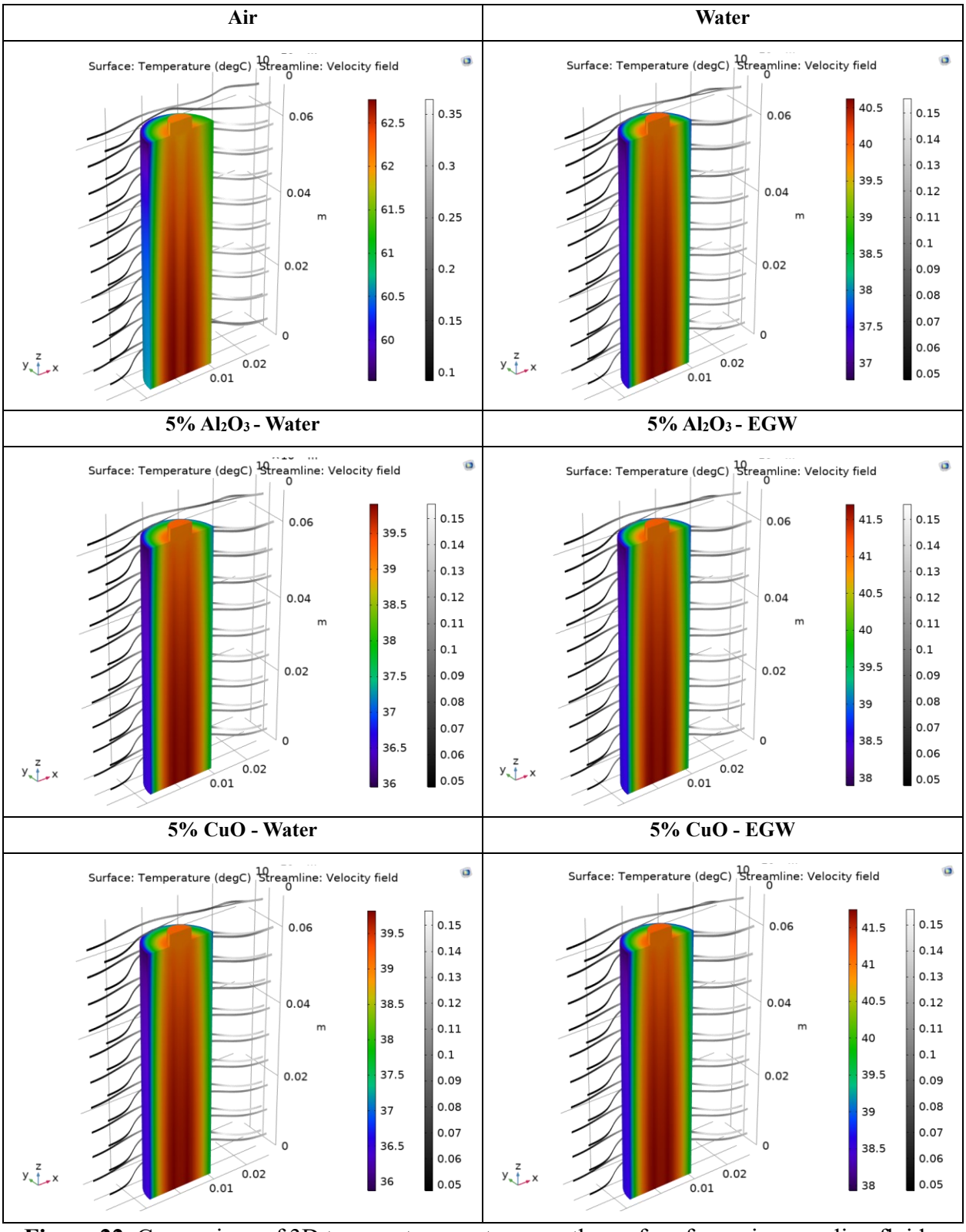

Figure 22. Comparison of 3D temperature contours on the surface for various cooling fluids.

As illustrated in Figure 23, the impact of varying volume fractions (2%, 3%, and 5%) was evaluated for the Al_2O_3-Water nanofluid. The data demonstrates that elevating the volumetric concentration of Al_2O_3 nanoparticles significantly improves effective thermal conductivity, thereby increasing the convective heat transfer coefficient. This enhancement facilitates superior heat dissipation from the battery surface, resulting in a reduction of the T_{max}. Consequently, the 5% Al_2O_3-Water nanofluid exhibited the optimal thermal management performance among the tested concentrations.

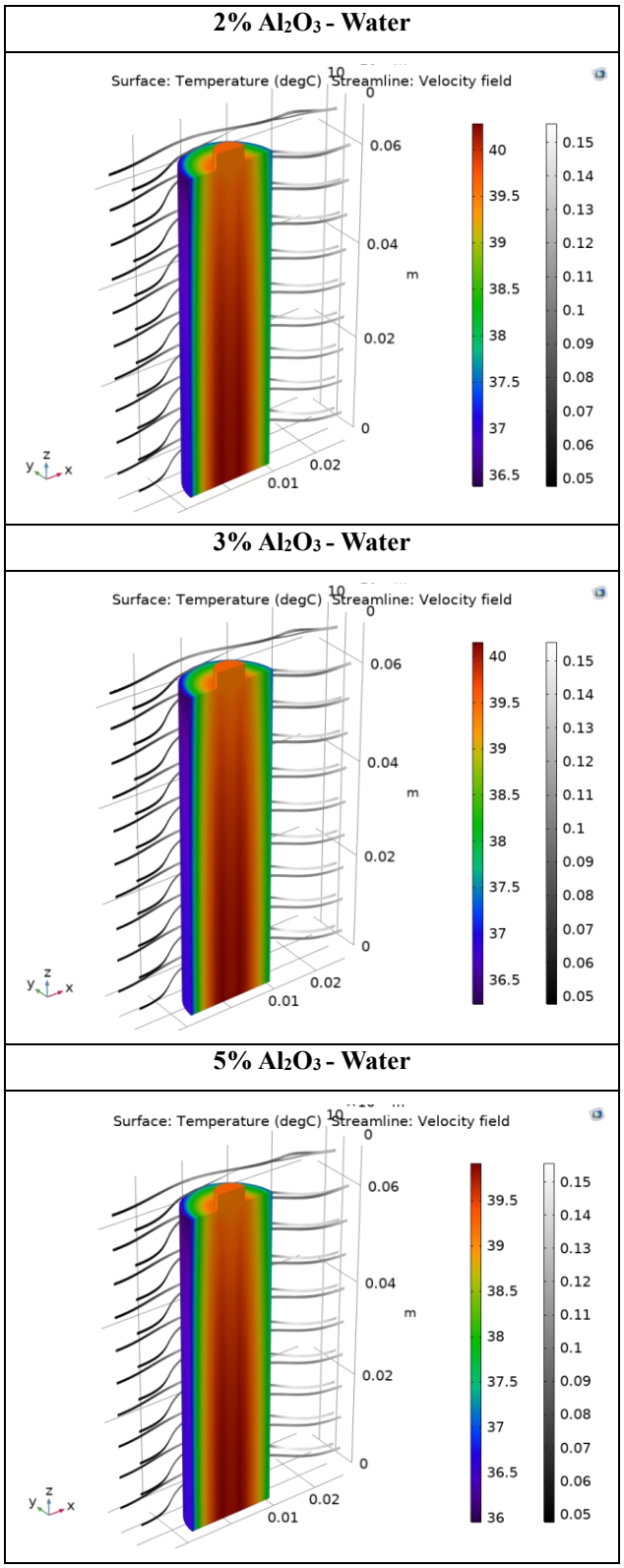

Figure 23. Influence of Al_2O_3-Water nanofluid volumetric concentration on the battery's 3D thermal distribution.

3D thermal analysis was conducted on an air-cooled cylindrical LIB under three distinct coolant velocities. As depicted in Figure 24, the efficiency of the thermal management system correlates directly with fluid velocity. Elevating the inlet velocity (V_{inlet}) proved to be a decisive factor in reducing operational temperatures by intensifying the cooling process. The maximum velocity of 0.2 m/s resulted in the lowest total battery temperature rise, effectively maximizing heat removal. At this velocity, the Reynolds number was estimated at approximately 266, confirming that the flow remained well within the laminar regime. Consistent with this finding, the Laminar Flow interface was utilized for all air cooling simulations. However, this thermal enhancement necessitates a significant energy trade-off: the pumping power required at 0.2 m/s increased by a factor of 16 relative to the 0.05 m/s baseline.

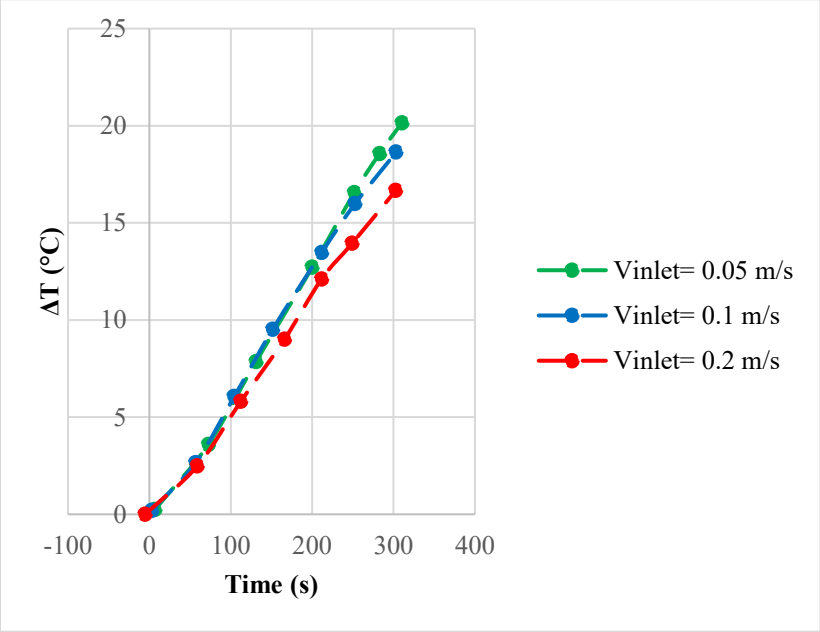

Figure 24. Comparative analysis of the effect of varying V_{inlet} on the time-dependent ΔT.

Figure 25 elucidates the direct correlation between the air V_{inlet} and cooling efficiency. A fourfold increase in flow velocity (from 0.05 m/s to 0.2 m/s) resulted in a reduction of approximately 15.5°C in the battery's T_{max}. This significant thermal improvement is attributed to the higher mass flow rate interacting with the battery surface. Furthermore, the velocity streamlines corroborate this behavior: as V_{inlet} rises, the maximum local fluid velocity scales from 0.18 m/s to 0.65 m/s. This high-momentum flow effectively thins the thermal boundary layer, thereby augmenting the convective heat transfer coefficient and optimizing heat dissipation.

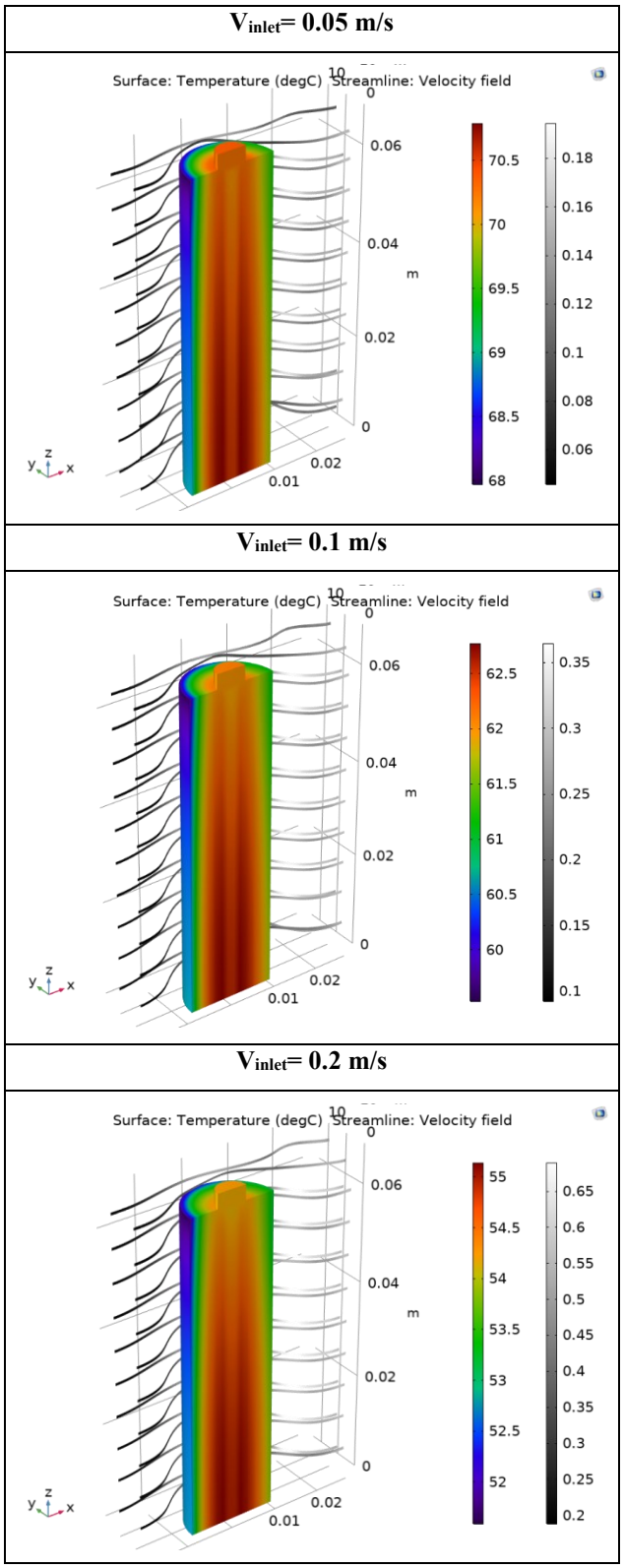

Figure 25. Impact of V_{inlet} on the battery's 3D surface temperature profile and velocity streamlines under air-cooling conditions.

4.4 3D BTMS with the Taguchi Optimization Method

Simulations of the 3D battery thermal model were performed for the 9 distinct parameter combinations planned according to the Taguchi L9 orthogonal array. The T_{max}, serving as the primary response variable for the study, was recorded for each experimental condition and is summarized in Table 14.

An examination of the findings in Table 14 clearly indicates that the level changes in the control factors have a significant impact on the battery's thermal performance. The resulting T_{max} values are distributed over a wide range, from 35.5°C to 50.0°C (a variation of 14.5°C).

- Lowest T_{max} (Desired State): The minimum T_{max} was observed as 35.5°C in the L9 experiment (A3, B3, C2, D1) configuration. This condition represents the combination of Water as the base fluid, a 5% Al_2O_3 volume fraction, a 3 × r_batt battery distance, and a 293.15 K T_{inlet}. Another similarly low temperature of 36.0°C was obtained in the L5 experiment (A2, B2, C3, D1).
- Highest T_{max} (Undesired State): The T_{max} value was recorded as 50.0°C in the L3 experiment (A1, B3, C3, D3) configuration. This condition involved the settings of Ethylene Glycol as the base fluid, a 5% Al_2O_3 volume fraction, a 3.5 × r_batt battery distance, and a 303.15 K inlet temperature.

These raw T_{max} results reveal a distinct difference of 14.5°C between the best-case (L9) and worst-case (L3) scenarios, proving how critical the selected parameters are for optimization.

Table 14. L9 orthogonal array configuration and the obtained T_{max} results.

Orthogonal Design	A	B	C	D	T_{max} (°C)
L1	1	1	1	1	48.5
L2	1	2	2	2	48
L3	1	3	3	3	50
L4	2	1	2	3	46
L5	2	2	3	1	36
L6	2	3	1	2	45
L7	3	1	3	2	38.5
L8	3	2	1	3	47.5
L9	3	3	2	1	35.5

To minimize the battery T_{max}, the "smaller-is-better" S/N analysis was applied. The S/N ratio response table, presented in Table 15, shows the average S/N ratios for each control factor (A, B, C, D) at their different levels. According to the Taguchi methodology, for the 'smaller-is-better' objective, the level with the highest S/N ratio is considered the optimal level for that factor.

Analyzing the table:

- Factor A (Base Fluid): The highest S/N ratio (-32.08) was obtained at Level 3 (Water).
- Factor B (Volume Fraction (Φ)-Al_2O_3): The highest S/N ratio (-32.68) was obtained at Level 3 (5%).
- Factor C (Battery-Battery Distance): The highest S/N ratio (-32.27) was obtained at Level 3 (3.5 × r_batt).
- Factor D (T_{inlet}): The highest S/N ratio (-31.95) was obtained at Level 1 (293.15 K).

Based on these findings, the optimal parameter combination that minimizes the T_{max} value is determined to be A3-B3-C3-D1.

The 'Delta' value in the table (the difference between the maximum and minimum S/N ratio for each factor) indicates the relative influence of that factor on the response variable (T_{max}). The 'Rank' column orders the factors by this magnitude of effect:

1. Factor A (Base Fluid) (Delta = 1.69)
2. Factor D (T_{inlet}) (Delta = 1.64)
3. Factor C (Battery-Battery Distance) (Delta = 1.17)
4. Factor B (Φ-Al_2O_3) (Delta = 0.21)

This ranking clearly demonstrates that the base fluid and T_{inlet} are the most dominant factors affecting the battery cooling performance. Conversely, the Φ-Al_2O_3 (Factor B) was found to be the least influential factor on T_{max} within the range studied.

Table 15. S/N ratio responses for T_{max} (smaller-is-better).

Level	A	B	C	D
1	-33,77	-32,89	-33,44	-31,95
2	-32,48	-32,76	-32,63	-32,80
3	-32,08	-32,68	-32,27	-33,59
Delta	1,69	0,21	1,17	1,64
Rank	1	4	3	2

To validate the findings from the S/N ratio analysis and to observe the direct effect of the factors on the raw temperature data, the mean T_{max} values at each factor level were examined. The "response table for means," presented in Table 16, lists the average T_{max} obtained at levels 1, 2, and 3 for each parameter. As the objective of the study is to minimize T_{max}, the level with the lowest average temperature for each factor indicates the preferred level.

According to the table:

- Factor A (Base Fluid): The lowest mean temperature (40.50°C) was obtained at Level 3 (Water - W).
- Factor B (Φ-Al_2O_3): The lowest mean temperature (43.50°C) was obtained at Level 3 (5%).
- Factor C (Battery-Battery Distance): The lowest mean temperature (41.50°C) was obtained at Level 3 (3.5 × r_batt).
- Factor D (T_{inlet}): The lowest mean temperature (40.00°C) was obtained at Level 1 (293.15 K).

These results directly confirm the A3-B3-C3-D1 optimal combination identified by the S/N ratio analysis (Table 15).

Furthermore, the 'Delta' value in the table (the difference between the maximum and minimum mean T_{max} for each factor) represents the magnitude of that factor's absolute effect on T_{inlet}. The 'Rank' column orders the factors by this magnitude of effect:

1. Factor A (Base Fluid) (Delta = 8.33°C)
2. Factor D (T_{inlet}) (Delta = 7.83°C)
3. Factor C (Battery-Battery Distance) (Delta = 5.50°C)
4. Factor B (Φ-Al_2O_3) (Delta = 0.83°C)

This ranking is in perfect agreement with the ranking obtained from the S/N ratio analysis (Rank: 1-A, 2-D, 3-C, 4-B). Both analyses consistently demonstrate that the base fluid (A) has the most significant effect on T_{max}, followed closely by the T_{inlet} (D). The effect of the Φ-Al_2O_3 (B) is markedly less significant compared to the other factors.

Table 16. Mean responses for T_{max}.

Level	A	B	C	D
1	48,83	44,33	47,00	40,00
2	42,33	43,83	43,17	43,83
3	40,50	43,50	41,50	47,83
Delta	8,33	0,83	5,50	7,83
Rank	1	4	3	2

As part of the Taguchi analysis, a "main effects plot" was generated to visualize the impact of each control factor (A, B, C, D) on the battery's T_{max}. This plot, presented in Figure 26, is a graphical representation of the "response table for means" (previously shown in Table 16). The vertical axis represents the mean T_{max} value, while the horizontal axis shows the levels (1, 2, 3) for each factor.

Since the study's objective is to minimize T_{max}, the lowest point on the plot for each factor indicates its optimal level:

- Factor A (Base Fluid): The lowest mean temperature is achieved at Level 3 (Water).
- Factor B (Φ-Al_2O_3): The lowest mean temperature is at Level 3 (5%).
- Factor C (Battery-Battery Distance): The lowest mean temperature is at Level 3 (3.5 × r_batt).
- Factor D (T_{inlet}): The lowest mean temperature is at Level 1 (293.15 K).

This visual analysis clearly shows that the conditions for optimal T_{max} performance are A3-B3-C3-D1, confirming the findings from Tables 15 and 16.

Furthermore, the steepness (slope) of a line represents the magnitude of that factor's effect (its significance) on T_{max}.

- Factor A (Base Fluid) and Factor D (T_{inlet}) exhibit the steepest slopes between levels. This visually proves that these two parameters are the most dominant factors in controlling the battery temperature.
- Factor C (Battery-Battery Distance) also shows a significant negative trend, reducing temperature from Level 1 to Level 3, indicating it is an important factor.
- In stark contrast, the line for Factor B (Φ-Al_2O_3) is nearly horizontal. This indicates that the nanofluid concentration, within the studied range of 2%-5%, has very little (or negligible) statistical effect on T_{max}.

These visual findings are in perfect agreement with the calculated 'Rank' (Rank: 1-A, 2-D, 3-C, 4-B) from the previous response Tables 15 and 16.

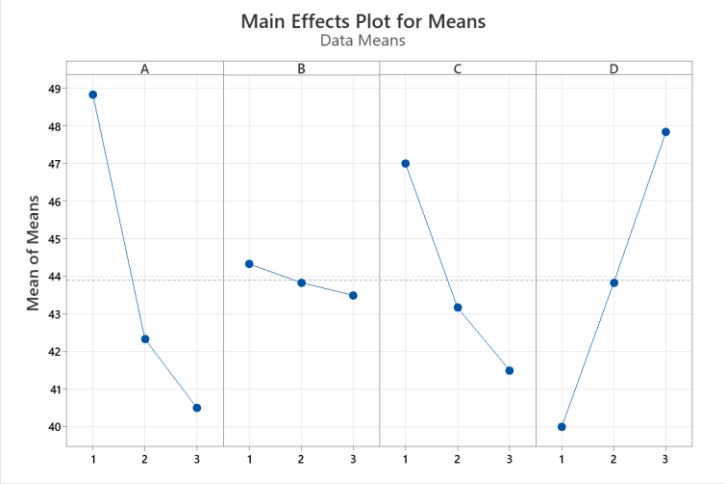

Figure 26. Main effects of the means for T_{max}.

To determine the optimal levels of the four control factors, the main effects plot for the "smaller-is-better" S/N ratio data was plotted, as presented in Figure 27. In this graph, the vertical axis represents the mean of S/N ratios. According to the Taguchi methodology, the highest S/N ratio value is desired, as it signifies a performance that is both on target (low T_{max}) and robust against noise (low variation).

Upon examining the plot, the levels that yield the highest S/N ratio for each factor are as follows:

- Factor A (Base Fluid): The highest S/N ratio is observed at Level 3 (Water).
- Factor B (Φ-Al_2O_3): The highest S/N ratio is observed at Level 3 (5%).

- Factor C (Battery-Battery Distance): The highest S/N ratio is observed at Level 3 (3.5 × r_batt).
- Factor D (T_{inlet}): The highest S/N ratio is observed at Level 1 (293.15 K).

This analysis visually confirms that the optimal conditions required to minimize T_{max} are A3-B3-C3-D1. This result is in perfect consistency with the main effects plot for means (Figure 26).

Furthermore, the slopes of the lines in the plot corroborate the factor ranking. Factor A (base fluid) and Factor D (T_{inlet}) demonstrate the sharpest changes in S/N ratio between levels, proving they are the most influential factors. Conversely, the line for Factor B (Φ-Al_2O_3) is nearly horizontal, confirming it has the least significant impact by causing very little change in the S/N ratio. These findings perfectly align with the 'Rank' established in the S/N response table (Table 15).

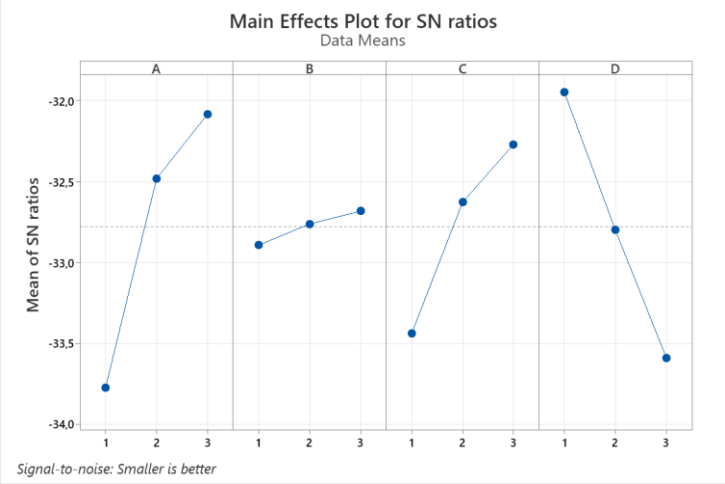

Figure 27. Main effects of the S/N ratios for T_{max}.

ANOVA is a statistical method used to decompose and identify the sources of total variability observed in results. Developed by R.A. Fisher, this method tests the statistical significance of the parameters (control factors) on the process output. Its fundamental principle is based on the ratio of between-group variability (factor effect) to within-group variability.

ANOVA was performed to quantitatively determine the statistical significance and relative influence of the four control factors (A, B, C, D) on the battery T_{max}. The ANOVA results are summarized in Table 17.

In this study, as an L9 array was used for 4 factors at 3 levels, the total 8 degrees of freedom (DF) were assigned to the factors (Total DF = 9 runs - 1 = 8; Factor DF = 4 factors * (3 levels - 1) = 8). This is known as a "saturated" design, which leaves zero DF for the residual error (DF_Error = 0). Consequently, standard F-values and P-values cannot be calculated (indicated by '*' in the table).

In such a case, the strength of each factor's effect on T_{max} is determined by examining its "adjusted sum of squares" (Adj SS) and calculating its "percentage contribution" (P%). The P% shows that factor's share of the total variation.

The ANOVA results statistically confirm the findings from the S/N ratio and main effects plots.

1. Factor A (Base Fluid) is identified as the most dominant factor influencing T_{max}, with a contribution of 44.96%.
2. Factor D (T_{inlet}) is the second most significant factor at 36.00%.
3. Factor C (Battery-Battery Distance) has a moderate effect with a contribution of 18.65%.
4. Factor B (Φ-Al_2O_3), with a contribution of only 0.41%, has a statistically insignificant (negligible) effect on T_{max}.

This analysis quantitatively demonstrates that efforts to reduce battery temperature should primarily focus on the selection of the base fluid and the coolant T_{inlet}.

Table 17. ANOVA of the T_{max} means.

Source	DF	Seq SS	Adj SS	Adj MS	F	P
A	2	115,056	115,056	57,5278	*	*
B	2	1,056	1,056	0,5278	*	*
C	2	47,722	47,722	23,8611	*	*
D	2	92,056	92,056	46,0278	*	*
Residual Error	0	*	*	*		
Total	8	255,889				

The Taguchi S/N ratio and ANOVA analyses identified the optimal parameter combination as A3-B3-C3-D1 for minimizing T_{max}. To validate the performance of this optimal design (Water-based, 5% Al_2O_3, 3.5 × r_batt distance, 293.15 K T_{inlet}) and to quantify the effectiveness of the optimization, a confirmation simulation was performed in COMSOL Multiphysics using this new configuration.

Figure 28 presents a direct comparison between the results of this confirmation run (post-optimization) and the initial experimentally validated air-cooled reference model (pre-optimization) used at the study's outset.

- Figure 28 (Pre-Optimization): This shows the baseline air-cooled reference model. Upon examining the temperature color scale, it is evident that the battery surface is 60°C - 62.5°C. This temperature is above the safe operating limit for LIBs (typically below 60°C) and carries a risk of thermal runaway.
- Figure 28 (Post-Optimization): This shows the nanofluid-cooled model based on the optimal A3-B3-C3-D1 design found via the Taguchi method. The temperature scale (30.5°C - 33.5°C) on the battery surface demonstrates a dramatic improvement in cooling performance. In the optimized design, the T_{max} is successfully limited to approximately 33.5°C.

This comparison quantitatively proves the success of the Taguchi optimization. The optimal nanofluid-cooled design achieved a remarkable reduction of 29.0°C in battery T_{max} compared to the initial air-cooled design.

It is also noteworthy that this T_{max} of 33.5°C is even lower than the best result obtained within the L9 experimental array (35.5°C from the L9 run). This validates the predictive capability of the Taguchi method, showing it can not only identify the best result within an experimental set but also successfully predict an "optimum" combination outside of that set that performs even better.

Pre-optimization Air Cooled Model	Taguchi-Optimized (A3-B3-C3-D1) Nanofluid Cooled Model
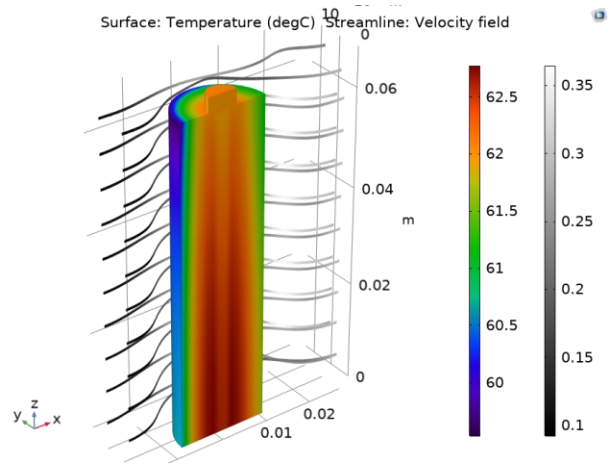	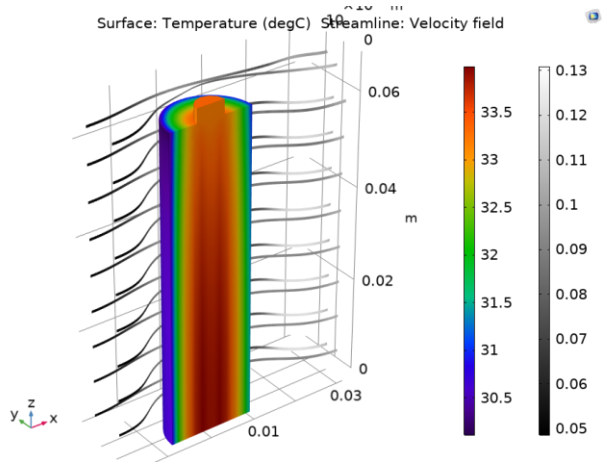

Figure 28. Surface temperature contours and velocity streamlines for the baseline air-cooled and optimized (A3-B3-C3-D1) nanofluid-cooled models.

To evaluate the effect of optimization on the battery's thermal behavior, not only in terms of T_{max} but also in terms of heating rate, a time-dependent analysis was conducted. Figure 29 illustrates the temperature increase in the battery over a 300-second operating period.

- Air-Cooled Model: This represents the initial air-cooled reference model. As seen in the graph, the temperature rise in this model is very rapid (steep slope), and at the end of the 300-second period, the ΔT reached approximately 18.7°C. This indicates that heat is not being effectively dissipated and is rapidly accumulating in the system.
- Optimized Nanofluid Model: This represents the A3-B3-C3-D1 configuration optimized via the Taguchi method. In this model, the heating rate is significantly slower (a much flatter slope). At the end of the same 300-second period, the temperature rise in the optimized system was limited to only approximately 5.1°C.

This graph proves that the thermal stability of the optimized A3-B3-C3-D1 design is far superior. The optimized system achieved an approximate 73% reduction in the rate of temperature increase compared to the initial air-cooled system (5.1°C vs. 18.7°C).

This finding corroborates the low T_{max} value seen in Figure 28: the optimized nanofluid cooling system driven by the dominant effects of the (A) base fluid (Water) and (D) T_{inlet} (293.15 K) is

able to dissipate the heat generated by the battery much more efficiently, preventing it from reaching dangerous temperature levels.

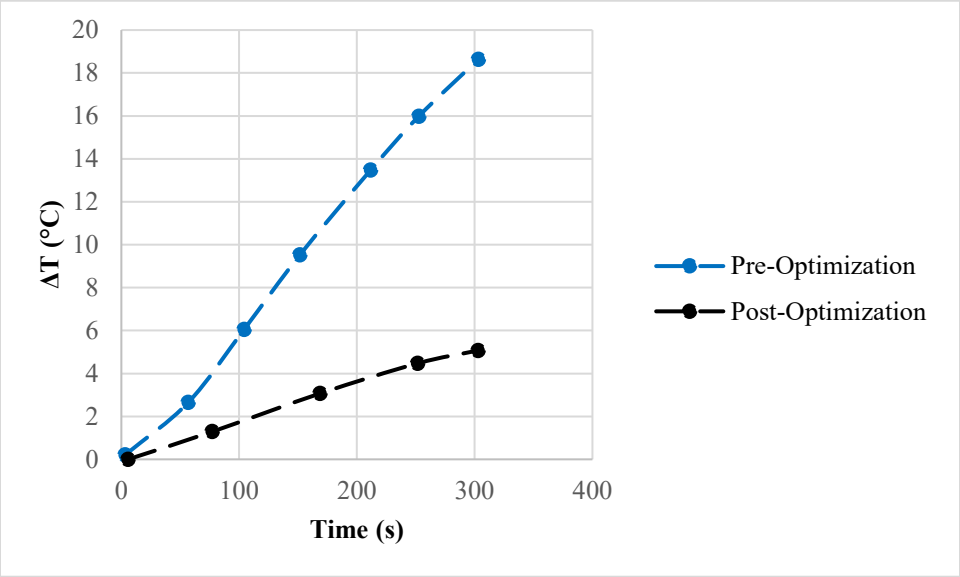

Figure 29. Time-dependent ΔT for the pre-optimization air-cooled and post-optimization (A3-B3-C3-D1) nanofluid-cooled models.

5. CONCLUSION

As the modeling of energy storage systems remains essential for future developments, understanding the interplay between design choices and functional performance is crucial. LIBs, distinguished by their high energy and power density, continue to be a focal point of this research. Through the simulation of a 1D isothermal LIB in COMSOL Multiphysics, this study first investigated the impact of varying C-rates. The findings confirm that higher C-rates exacerbate internal heterogeneity, causing significant increases in voltage spreads, electrolyte salt concentration gradients, and the diffusion lag between the particle surface and center.

Building on the fundamental components of battery systems electrodes and electrolytes the model-guided selection of functional materials was identified as a critical strategy for designing efficient battery configurations. The investigation into material selection using the Battery Design Module revealed significant performance differences. The results indicate that batteries utilizing polymer electrolytes generally exhibit an average electrolyte salt concentration range within the electrodes that is approximately 70% higher than those using liquid electrolytes. Similarly, the concentration range within the electrolyte component itself is roughly 40% higher for polymers. Regarding

discharge performance, liquid electrolytes consistently demonstrated a voltage advantage of approximately 0.05 V at a 1 C-rate compared to polymer variants.

Further investigation into positive electrode materials revealed that materials with lower concentration and density experienced more pronounced increases in AESOC values during discharge and sharper declines during charging. Specifically, $LiNiO_2$ showed the highest initial voltage (6.17 V) and the largest voltage differential (3.58 V), whereas LFP started with the lowest initial voltage (3.21 V) and showed the smallest potential difference (0.9 V). Based on these findings, distinct material recommendations are proposed: $LiNiO_2$ and NCA are recommended for high-energy applications (e.g., EVs), while LFP is recommended for safety and stability-critical applications due to its balanced trade-off between performance and cycle life.

Complementing the electrochemical analysis, this study provided a comprehensive thermal analysis of a 3D cylindrical LIB model. The results underscore that the selection of coolant, flow parameters, and nanofluid concentration is critical for effective temperature control. Liquid cooling demonstrated superior thermal management capabilities compared to air cooling. Under air cooling (V_{inlet} = 0.1 m/s), the battery experienced ΔT of ~18.5°C and a surface T_{max} ~62.5°C after 300 seconds, whereas all liquid cooling scenarios ensured stable operation, limiting the ΔT to below 6°C and the surface Tmax to below 41.5°C. Furthermore, the inclusion of Al_2O_3 and CuO nanoparticles significantly improved thermal performance, with optimal results achieved using water-based nanofluids.

Finally, the Taguchi L9 orthogonal array methodology, combined with S/N ratio analysis and ANOVA, was successfully applied to minimize the T_{max} of the cylindrical LIB. Based on the smaller-is-better S/N ratio analysis, the optimal parameter combination was determined to be a Water (W) base fluid, a 5% Al_2O_3 volume fraction, a 3.5 x r_batt battery distance, and a 293.15 K (20°C) T_{inlet}. The ANOVA identified the base fluid as the most dominant factor (44.96% contribution), closely followed by the T_{inlet} (Factor D) with a 36.00%. The optimized nanofluid-cooled design achieved a T_{max} of 33.5°C, representing a 29.0°C reduction compared to the air-cooled reference model and performing better than the best result within the experimental matrix. This confirms the Taguchi method as an efficient and powerful statistical tool for optimizing a BTMS, validating the study's approach to enhancing simulation accuracy and making informed material decisions for reliable LIB systems.

ABBREVIATATIONS

BTMS	Battery Thermal Management Systems
EG	Ethylene Glycol
EGW	Ethylene Glycol Water
ANOVA	Analysis of Variance
T_{max}	Maximum Temperature
T_{inlet}	Inlet Temperature
LFP	Lithium Iron Phosphate
LIB	Lithium-ion Battery
EV	Electric Vehicle
NiCd	Nickel-Cadmium
NiMH	Nickel-Metal Hydride
NiZn	Nickel-Zinc
AgZn	Silver-Zinc
Li-ion	Lithium-ion
DOD	Depth of Discharge
SOC	State of Charge
BMS	Battery Management Systems
Ah	Ampere-Hours
LCO	Lithium Cobalt Oxide
LMO	Lithium Manganese Oxide
NMC	Lithium Nickel Manganese Cobalt Oxide
NCA	Lithium Nickel Cobalt Aluminum Oxide
DMC	Dimethyl Carbonate
DEC	Diethyl Carbonate
EMC	Ethyl Methyl Carbonate
EC	Ethylene Carbonate
PC	Propylene Carbonate
$LiPF_6$	Lithium Hexafluorophosphate
HEV	Hybrid Electric Vehicle

PHEV	Plug-in Hybrid Electric Vehicle
PCM	Phase Change Material
DCR	Direct Current Resistance
SEM	Scanning Electron Microscope
ECM	Equivalent Circuit Model
S/N	Signal-to-Noise
1D	One-Dimensional
PVDF-HFP	Poly (Vinylidene Fluoride-Hexafluoropropylene)
Ref.	Reference
Eq.	Equation
ΔT	Temperature Change
OCV	Open Circuit Voltage
AESOC	Average Electrode State of Charge
V_{inlet}	Inlet Velocity
Φ	Volume Fraction

APPENDIX

Table A. Key parameters for five selected positive electrode materials.

Electrode Material Type	**Electrical Conductivity**	**Reference Concentration**	**Maximum-Minimum Electrode SOC**	**Poisson's Ratio**	**Young's Modulus**	**Density**	**Difussion Coefficient**	**Some Other Properties**	
LCO, $LiCoO_2$	1.13 mS/cm	56250 mol/m^3	1 0.43	0.24	191 GPa	5000 kg/m^3	5×10^{-13} m^2/s	**Coefficient of Thermal Expansion**	
								1.3×10^{-5} 1/K	
LMO, $LiMn_2O_4$	3.8 S/m	22860 mol/m^3	0.995 0.175	0.26	194 GPa	4140 kg/m^3			
LFP, $LiFePO_4$	91 S/m	21190 mol/m^3	0.90 0.01	0.3	117.8 GPa	3600 kg/m^3	3.2×10^{-13} m^2/s	**Thermal Conductivity**	**Heat Capacity at Constant Pressure**
								1 W/(m×K)	881 J/(kg×K)
$LiNiO_2$	100 S/m	23000 mol/m^3	1 0.45			4650 kg/m^3		**Temperature Derivative of Equilibrium Potential**	
								0 V/K	
NCA, $LiNi_{0.8}Co_{0.15}Al_{0.05}O_2$	91 S/m	48000 mol/m^3	1 0.25			4740 kg/m^3	1.5×10^{-15} m^2/s		

REFERENCES

1. Li, M., Lu, J., Chen, Z., & Amine, K. (2018). 30 years of lithium-ion batteries. *Advanced materials*, *30*(33), 1800561.

2. Alarco, J., & Talbot, P. (2015). The history and development of batteries. *Phys. org*, *30*.

3. Stinner, A. (2008). Alessandro Volta and Luigi Galvani (PDF).

4. The Great Idea Finder. (n.d.). *Electric battery history - invention of the electric battery*. Available online: Electric Battery History - Invention of the Electric Battery (accessed on 4 December 2025).

5. Electromagnetism Available online: Electromagnetism - Wikipedia (accessed on 4 December 2025).

6. Borvon, G. (10). *September 2012."History of the electrical units"*. Association S-EAU-S.

7. Crompton, T. R. (2000). *Battery reference book*. Newnes.

8. Pauling, L. (1988). 15: Oxidation-Reduction Reactions; Electrolysis. *General Chemistry, Mineola, Dover Publications*.

9. Electric battery Available online: Electric battery - Wikipedia (accessed on 4 December 2025).

10. Silberberg, M. S., & Amateis, P. (2006). *Chemistry: The molecular nature of matter and change* (Vol. 4). New York: McGraw-Hill.

11. Li, A., Yuen, A. C. Y., Wang, W., De Cachinho Cordeiro, I. M., Wang, C., Chen, T. B. Y., ... & Yeoh, G. H. (2021). A review on lithium-ion battery separators towards enhanced safety performances and modelling approaches. *Molecules*, *26*(2), 478.

12. Zhu, P., Gastol, D., Marshall, J., Sommerville, R., Goodship, V., & Kendrick, E. (2021). A review of current collectors for lithium-ion batteries. *Journal of Power Sources*, *485*, 229321.

13. Horiba, T. (2014). Lithium-ion battery systems. *Proceedings of the IEEE*, *102*(6), 939-950.

14. Deng, D., Kim, M. G., Lee, J. Y., & Cho, J. (2009). Green energy storage materials: Nanostructured TiO2 and Sn-based anodes for lithium-ion batteries. *Energy & Environmental Science*, *2*(8), 818-837.

15. Deng, D. (2015). Li-ion batteries: basics, progress, and challenges. *Energy Science & Engineering*, *3*(5), 385-418.

16. Schlesinger, H., & Spence, J. C. (2010). The battery: How portable power sparked a technological revolution. *Physics Today*, *63*(5), 45.

17. Pradhan, S. K., & Chakraborty, B. (2022). Battery management strategies: An essential review for battery state of health monitoring techniques. *Journal of energy storage*, *51*, 104427.

18. MIT Electric Vehicle Team. (2008, December). *A guide to understanding battery specifications*. Massachusetts Institute of Technology. Available online: A Guide to Understanding Battery Specifications (accessed on 4 December 2025).

19. Yüksek, G., & Alkaya, A. (2023, November). Effect of the depth of discharge and c-rate on battery degradation and cycle life. In *2023 14th International Conference on Electrical and Electronics Engineering (ELECO)* (pp. 1-5). IEEE.

20. Khan, M. I., Gilani, R., Hafeez, J., Ayoub, R., Zahoor, I., & Saira, G. (2025). Advantages and disadvantages of lithium-ion batteries. In *Nanostructured Lithium-ion Battery Materials* (pp. 47-64). Elsevier.

21. Yuan, X., Liu, H., & Zhang, J. (2011). Lithium-ion batteries: advanced materials and technologies. CRC.

22. Huang, P., Tu, R., Zhang, X., Han, M., Sun, Y., Hussain, S. A., & Zhang, L. (2022). Investigation of electric vehicle smart charging characteristics on the power regulation performance in solar powered building communities and battery degradation in Sweden. *Journal of energy storage*, *56*, 105907.

23. Chikkannanavar, S. B., Bernardi, D. M., & Liu, L. (2014). A review of blended cathode materials for use in Li-ion batteries. *Journal of Power Sources*, *248*, 91-100.

24. Li, W., Erickson, E. M., & Manthiram, A. (2020). High-nickel layered oxide cathodes for lithium-based automotive batteries. *Nature Energy*, *5*(1), 26-34.

25. Yang, X. G., Liu, T., & Wang, C. Y. (2021). Thermally modulated lithium iron phosphate batteries for mass-market electric vehicles. *Nature Energy*, *6*(2), 176-185.

26. Almadani, M., Oni, O. E., Longe, O. M., & Olatomiwa, L. (2024, April). Comparison of battery chemistries for electric vehicle applications. In *5th African International Conference on Industrial Engineering and Operations Management* (pp. 23-25).

27. Lithium Salts And Solvents Effects On Electrolyte Wetting. Available online: **https://iestbattery.com/effect-of-lithium-salts-on-the-electrolyte-wetting/** (accessed on 24 March 2025).

28. Ji, Y., Zhang, Y., & Wang, C. Y. (2013). Li-ion cell operation at low temperatures. *Journal of The Electrochemical Society*, *160*(4), A636.

29. Ren, D., Smith, K., Guo, D., Han, X., Feng, X., Lu, L., ... & Li, J. (2018). Investigation of lithium plating-stripping process in Li-ion batteries at low temperature using an electrochemical model. *Journal of The Electrochemical Society*, *165*(10), A2167.

30. He, F., Li, X., Zhang, G., Zhong, G., & He, J. (2018). Experimental investigation of thermal management system for lithium ion batteries module with coupling effect by heat sheets and phase change materials. *International Journal of Energy Research*, *42*(10), 3279-3288.

31. Finegan, D. P., Darcy, E., Keyser, M., Tjaden, B., Heenan, T. M., Jervis, R., ... & Shearing, P. R. (2017). Characterising thermal runaway within lithium-ion cells by inducing and monitoring internal short circuits. *Energy & Environmental Science*, *10*(6), 1377-1388.

32. Yang, Z., Huang, Q., Li, S., & Mao, J. (2018). High-temperature effect on electrochemical performance of Li4Ti5O12 based anode material for Li-ion batteries. *Journal of Alloys and Compounds*, *753*, 192-202.

33. Panchal, S., Mcgrory, J., Kong, J., Fraser, R., Fowler, M., Dincer, I., & Agelin-Chaab, M. (2017). Cycling degradation testing and analysis of a LiFePO4 battery at actual conditions. *International Journal of Energy Research*, *41*(15), 2565-2575.

34. Bandhauer, T. M., Garimella, S., & Fuller, T. F. (2011). A critical review of thermal issues in lithium-ion batteries. *Journal of the electrochemical society*, *158*(3), R1.

35. Shiao, H. C. A., Chua, D., Lin, H. P., Slane, S., & Salomon, M. (2000). Low temperature electrolytes for Li-ion PVDF cells. *Journal of power sources*, *87*(1-2), 167-173.

36. Bugga, R., Smart, M., Whitacre, J., & West, W. (2007, March). Lithium ion batteries for space applications. In *2007 IEEE Aerospace Conference* (pp. 1-7). IEEE.

37. Yuan, Q., Zhao, F., Wang, W., Zhao, Y., Liang, Z., & Yan, D. (2015). Overcharge failure investigation of lithium-ion batteries. *Electrochimica Acta*, *178*, 682-688.

38. Yang, K., An, J., & Chen, S. (2010). Thermal behavior analysis of nickel/metal hydride battery during overcharging. *Science China Chemistry*, *53*(5), 1177-1182.

39. Shim, J., Kostecki, R., Richardson, T., Song, X., & Striebel, K. A. (2002). Electrochemical analysis for cycle performance and capacity fading of a lithium-ion battery cycled at elevated temperature. *Journal of power sources*, *112*(1), 222-230.

40. Zhang, Y., Wang, C. Y., & Tang, X. (2011). Cycling degradation of an automotive LiFePO4 lithium-ion battery. *Journal of power sources*, *196*(3), 1513-1520.

41. Belt, J. R., Ho, C. D., Miller, T. J., Habib, M. A., & Duong, T. Q. (2005). The effect of temperature on capacity and power in cycled lithium ion batteries. *Journal of power sources*, *142*(1-2), 354-360.

42. Haran, B., White, R., & Popov, B. N. (2002). Capacity fade of Sony 18650 cells cycled at elevated temperatures Part II. Capacity fade analysis. *J. Power Sources*, *112*, 614-620.

43. Ning, G., Haran, B., & Popov, B. N. (2003). Capacity fade study of lithium-ion batteries cycled at high discharge rates. *Journal of power sources*, *117*(1-2), 160-169.

44. Pesaran, A. A., Swan, D., Olson, J., Guerin, J. T., Burch, S., Rehn, R., & Skellenger, G. D. (1998). *Thermal analysis and performance of a battery pack for a hybrid electric vehicle*. Brussels, Belgium: National Renewable Energy Laboratory.

45. Spotnitz, R., & Franklin, J. (2003). Abuse behavior of high-power, lithium-ion cells. *Journal of power sources*, *113*(1), 81-100.

46. Wang, Q., Ping, P., Zhao, X., Chu, G., Sun, J., & Chen, C. (2012). Thermal runaway caused fire and explosion of lithium ion battery. *Journal of power sources*, *208*, 210-224.

47. Wen, T., Zhou, Z., Zhang, Y., & Xu, X. (2025). Advances and Challenges in the Battery Thermal Management Systems of Electric Vehicles. *Materials*, *18*(20), 4718.

48. Nanofluid Available online: Nanofluid - Wikipedia (accessed on 4 December 2025).

49. Argonne National Laboratory. (n.d.). *Transportation Technology R&D Center*. Available online: Materials - Nanofluids (accessed on 4 December 2025).

50. Sajid, M. U., & Ali, H. M. (2019). Recent advances in application of nanofluids in heat transfer devices: a critical review. *Renewable and Sustainable Energy Reviews*, *103*, 556-592.

51. Mahbubul, I. M. (2019). *Preparation, characterization, properties and application of nanofluid*. William Andrew Publishing.

52. Hasan, M. F., Chen, C. F., Shaffer, C. E., & Mukherjee, P. P. (2015). Analysis of the implications of rapid charging on lithium-ion battery performance. *Journal of the Electrochemical Society*, *162*(7), A1382.

53. Leißing, M., Horsthemke, F., Wiemers-Meyer, S., Winter, M., Niehoff, P., & Nowak, S. (2021). The Impact of the C-Rate on Gassing During Formation of NMC622 II Graphite Lithium-Ion Battery Cells. *Batteries & Supercaps*, *4*(8), 1344-1350.

54. Snyder, C. (2016). *The effects of charge/discharge rate on capacity fade of lithium ion batteries*. Rensselaer Polytechnic Institute.

55. Somerville, L., Bareño, J., Trask, S., Jennings, P., McGordon, A., Lyness, C., & Bloom, I. (2016). The effect of charging rate on the graphite electrode of commercial lithium-ion cells: A post-mortem study. *Journal of Power Sources*, *335*, 189-196.

56. Wang, J., Liu, P., Hicks-Garner, J., Sherman, E., Soukiazian, S., Verbrugge, M., ... & Finamore, P. (2011). Cycle-life model for graphite-LiFePO4 cells. *Journal of power sources*, *196*(8), 3942-3948.

57. Tran, T. D., Feikert, J. H., Pekala, R. W., & Kinoshita, K. (1996). Rate effect on lithium-ion graphite electrode performance. *Journal of applied electrochemistry*, *26*(11), 1161-1167.

58. Zheng, H., Li, J., Song, X., Liu, G., & Battaglia, V. S. (2012). A comprehensive understanding of electrode thickness effects on the electrochemical performances of Li-ion battery cathodes. *Electrochimica Acta*, *71*, 258-265.

59. Li, J., Wang, D., & Pecht, M. (2019). An electrochemical model for high C-rate conditions in lithium-ion batteries. *Journal of Power Sources*, *436*, 226885.

60. Peng, P., & Jiang, F. (2016). Thermal safety of lithium-ion batteries with various cathode materials: A numerical study. *International Journal of Heat and Mass Transfer*, *103*, 1008-1016.

61. Choi, H., Lim, N. G., Lee, S. J., & Park, J. (2021). Numerical approach for lithium-ion battery performance considering various cathode active material composition for electric vehicles using 1D simulation. *Journal of Mechanical Science and Technology*, *35*(6), 2697-2705.

62. Zheng, G., Zhang, W., & Huang, X. (2018). Lithium-Ion Battery Electrochemical-Thermal Model Using Various Materials as Cathode Material: A Simulation Study. *ChemistrySelect*, *3*(41), 11573-11578.

63. Shim, J., & Striebel, K. A. (2003). Effect of electrode density on cycle performance and irreversible capacity loss for natural graphite anode in lithium-ion batteries. *Journal of power sources*, *119*, 934-937.

64. Choi, J., Son, B., Ryou, M. H., Kim, S. H., Ko, J. M., & Lee, Y. M. (2013). Effect of LiCoO2 cathode density and thickness on electrochemical performance of lithium-ion batteries. *Journal of Electrochemical Science and Technology*, *4*(1), 27-33.

65. Smekens, J., Gopalakrishnan, R., Van den Steen, N., Omar, N., Hegazy, O., Hubin, A., & Van Mierlo, J. (2016). Influence of electrode density on the performance of Li-ion batteries: Experimental and simulation results. *Energies*, *9*(2), 104.

66. Chabot, V., Farhad, S., Chen, Z., Fung, A. S., Yu, A., & Hamdullahpur, F. (2013). Effect of electrode physical and chemical properties on lithium-ion battery performance. *International Journal of Energy Research*, *37*(14), 1723-1736.

67. Ye, Y., Shi, Y., Cai, N., Lee, J., & He, X. (2012). Electro-thermal modeling and experimental validation for lithium ion battery. *Journal of Power Sources*, *199*, 227-238.

68. Wiriyasart, S., Hommalee, C., Sirikasemsuk, S., Prurapark, R., & Naphon, P. (2020). Thermal management system with nanofluids for electric vehicle battery cooling modules. *Case Studies in Thermal Engineering*, *18*, 100583.

69. Soleymani, P., Saffarifard, E., Jahanpanah, J., Babaie, M., Nourian, A., Mohebbi, R., ... & Ma, Y. (2023). Enhancement of an air-cooled battery thermal management system using liquid cooling with CuO and Al2O3 nanofluids under steady-state and transient conditions. *Fluids*, *8*(10), 261.

70. Koorata, P. K., & Chandrasekaran, N. (2021). Numerical investigation of cooling performance of a novel air-cooled thermal management system for cylindrical Li-ion battery module. *Applied Thermal Engineering*, *193*, 116961.

71. Suryavanshi, S. S., & Ghanegaonkar, P. M. (2025). Improving Electric Vehicle Air-Cooled Cylindrical Battery Temperature Control Systems: A Computational Fluid Dynamics (CFD) Study of an Innovative Uniform Flow Distribution Plate. *Energy Storage*, *7*(1), e70108.

72. Yetik, O., Morali, U., & Karakoc, T. H. (2023). A numerical study of thermal management of lithium-ion battery with nanofluid. *Energy*, *284*, 129295.

73. Thorat, P., Sanap, S., & Gawade, S. (2024). A comparative study of thermo-physical properties of different nanofluids for effective heat transfer leading to Li-ion battery pack cooling. *Energy Storage*, *6*(1), e566.

74. Banerjee, R., & Nidhul, K. (2025). Immersion cooling performance of nanofluid in a cylindrical cell battery pack using two-phase numerical simulations for varying discharge rates: A comparative study. *Results in Engineering*, *25*, 104377.

75. Panchal, S. (2024). Enhancing efficiency in air-cooled cylindrical battery temperature management systems for electric vehicles: A CFD analysis of a novel uniform flow distribution plate.

76. Yetik, O., & Karakoc, T. H. (2022). A study on lithium-ion battery thermal management system with Al2O3 nanofluids. *International Journal of Energy Research*, *46*(8), 10930-10941.

77. Ali, M., El-Leathy, A. M., & Al-Sofyany, Z. J. A. I. M. E. (2014). The effect of nanofluid concentration on the cooling system of vehicles radiator. *Advances in Mechanical Engineering*, *6*, 962510.

78. Ozbektas, S., Mumcu, F., Kaleli, A., & Sungur, B. (2025). Experimental and numerical study for temperature estimation in lithium-ion cells using Taguchi-based model parameterization. *Journal of Energy Storage*, *121*, 116538.

79. Sharma, H., Saxena, G., Rajput, R. S., & Randa, R. (2025). Optimization of Process Parameters of Novel Hybrid Automotive Battery Cooling System using GRA-Taguchi and Heatmap Visualization. *Journal of The Institution of Engineers (India): Series C*, *106*(5), 1281-1303.

80. Alrashdan, M. H. (2024). Optimizing Average Electric Power During the Charging of Lithium-Ion Batteries Through the Taguchi Method. *Transactions of Tianjin University*, *30*(2), 152-166.

81. Morali, U., Yetik, O., & Karakoc, T. H. (2024). Nanofluid-based cooling of prismatic lithium-ion battery packs: an integrated numerical and statistical approach. *Journal of Thermal Analysis and Calorimetry*, *149*(2), 799-811.

82. Kirad, K., & Chaudhari, M. (2021). Design of cell spacing in lithium-ion battery module for improvement in cooling performance of the battery thermal management system. *Journal of Power Sources*, *481*, 229016.

83. Shaik, S. A., Nigam, P. K., & Gugulothu, S. K. (2025). Optimizing cooling efficiency in Li-ion battery packs: A numerical study on the influence of inter-cell gaps and airflow dynamics. *Thermal Science and Engineering Progress*, 103624.

84. 1D Isothermal Lithium Ion Battery. COMSOL Inc. Available online: **https://www.comsol.com/model/1d-isothermal-lithium-ion-battery-686** (accessed on 17 February 2025).

85. Lu, J., & Mazumder, S. (2013). Development of fast one-dimensional model for prediction of coupled electrochemical-thermal behavior of Lithium-ion batteries. *The Ohio State University*.

86. Huber, I. S. (2017). Using COMSOL to Model a 1-D Lithium-Ion Battery. College of William and Mary, Department of Physics: Williamsburg, VA, USA.

87. Linden, D. (1995). Handbook of batteries. In *Fuel and energy abstracts* (Vol. 4, No. 36, p. 265).

88. Doyle, M., Newman, J., Gozdz, A. S., Schmutz, C. N., & Tarascon, J. M. (1996). Comparison of modeling predictions with experimental data from plastic lithium ion cells. Journal of the Electrochemical Society, 143(6), 1890.

89. Kaya, E., Reina, L., & d'Adamo, A. (2024, November). Investigating the Impact of Varied C-Rates on Lithium-Ion Batteries: A 1D Simulation Study. In *Journal of Physics: Conference Series* (Vol. 2893, No. 1, p. 012050). IOP Publishing.

90. Thermal Modeling of a Cylindrical Lithium-Ion Battery in 3D COMSOL Inc. Available online: Thermal Modeling of a Cylindrical Lithium-Ion Battery in 3D (accessed on 17 June 2025).

91. Kaya, E., & d'Adamo, A. (2025). Numerical Modelling of 1d Isothermal Lithium-Ion Battery with Varied Electrolyte and Electrode Materials. *Energies*, *18*(13), 3288.

92. D'Adamo, A., Corda, G., Berni, F., Diana, M., & Fontanesi, S. (2023). CFD simulations and potential of nanofluids for PEM fuel cells cooling. *SAE International Journal of Advances and Current Practices in Mobility*, *6*(2023-24-0144), 1800-1814.

93. Said, Z., Assad, M. E. H., Hachicha, A. A., Bellos, E., Abdelkareem, M. A., Alazaizeh, D. Z., & Yousef, B. A. (2019). Enhancing the performance of automotive radiators using nanofluids. *Renewable and Sustainable Energy Reviews*, *112*, 183-194.

94. Tahir, S., & Mital, M. (2012). Numerical investigation of laminar nanofluid developing flow and heat transfer in a circular channel. *Applied Thermal Engineering*, *39*, 8-14.

95. Mondal, B., Lopez, C. F., & Mukherjee, P. P. (2017). Exploring the efficacy of nanofluids for lithium-ion battery thermal management. *International Journal of Heat and Mass Transfer*, *112*, 779-794.

96. Pak, B. C., & Cho, Y. I. (1998). Hydrodynamic and heat transfer study of dispersed fluids with submicron metallic oxide particles. *Experimental Heat Transfer an International Journal*, *11*(2), 151-170.

97. Wang, X. Q., & Mujumdar, A. S. (2007). Heat transfer characteristics of nanofluids: a review. *International journal of thermal sciences*, *46*(1), 1-19.

98. Yu, W., & Choi, A. S. (2003). The role of interfacial layers in the enhanced thermal conductivity of nanofluids: a renovated Maxwell model. *Journal of nanoparticle research*, *5*(1), 167-171.

99. Brinkman, H. C. (1952). The viscosity of concentrated suspensions and solutions. *Journal of Chemical Physics*, *20*(4), 571–572.

100. Panchal, S., Mathew, M., Fraser, R., & Fowler, M. (2018). Electrochemical thermal modeling and experimental measurements of 18650 cylindrical lithium-ion battery during discharge cycle for an EV. *Applied Thermal Engineering*, *135*, 123-132.

101. Ghani, J. A., Choudhury, I. A., & Hassan, H. H. (2004). Application of Taguchi method in the optimization of end milling parameters. *Journal of materials processing technology*, *145*(1), 84-92.

102. Kaya, A. F., & Acır, A. (2022). Enhancing the aerodynamic performance of a Savonius wind turbine using Taguchi optimization method. *Energy Sources, Part A: Recovery, Utilization, and Environmental Effects*, *44*(2), 5610-5626.

103. Cheng, S. J., Miao, J. M., & Wu, S. J. (2010). Numerical optimization design of PEM fuel cell performance applying the Taguchi method. *World Academy of Science, Engineering and Technology*, *41*, 249-255.

104. Buchmann, I. (2016). *Batteries in a portable world: A handbook on rechargeable batteries for non-engineers* (4th ed.). Cadex Electronics.